THE CATEGORIZATION OF SOIL MOISTURE CONTENT IN THE NEAR INFRARED SPECTRUM

CATHERINE TSOUVALTSIDIS

A THESIS SUBMITTED TO THE FACULTY OF GRADUATE STUDIES
IN PARTIAL FULFILLMENT OF THE REQUIREMENTS FOR THE
DEGREE OF
MASTER OF SCIENCE

GRADUATE PROGRAM IN EARTH AND SPACE SCIENCE
YORK UNIVERSITY
TORONTO, ONTARIO

November 2016

Abstract

A new shortwave infrared remote sensing instrument potentially capable of measuring soil moisture from space was designed, tested and developed. The atmospheric spectral information and target detection range for infrared spectroscopy was analyzed. In order to measure soil moisture using grating spectroscopy, a trade study of the Argus 1000 spectrometer components was performed. This provided the basis for the chassis and component modifications required so that the desired spectral region could be viewed.

Two atmospheric windows in the SWIR, 1964 nm and 2020 nm have been identified as potential locations for soil moisture content observation from space. The second derivative method was successfully employed to calibrate Argus 2000 instrument by providing calibration points for each end of the detector. The resulted spectral resolution of the instrument is 3 nm and has a calculated SNR value of 479:1.

A custom Unmanned Aerial Vehicle (UAV) and data acquisition system (DAQ) was developed to ground test space-based observation methodologies. The system was field tested, collecting up to 10 minutes of data per flight.

The laboratory methodologies for soil baking, radiometric and wavelength calibration, and spectral collection was developed and performed. The soil baking methodology produced an error measurement of 2.4 %. Spectral measurements proved

well, resulting in the confirmation of the wavelength region 1964 nm in being able to provide potential use for measuring soil moisture content from space.

Dedication

This thesis is dedicated to my darling wife, best friend and confidant, Nythalah Baker. Without her endless support, love and encouragement I wouldn't have been able to see this through to the end. Thank you for being there to talk at all hours of the day and encouraging me to grow both as an engineer and a person, for holding me when I needed to be vulnerable, and for making me smile day in and day out.

I also dedicate this thesis to my Philip. You make me want to become a better person.

Είστε και οι δύο είναι ο κόσμος μου (You both are my world).

Acknowledgements

This thesis would have never even come to fruition without the help of Dr. Brendan Quine. Ben, you saw potential in me where no one else did and for that I am forever grateful. Thank you for guiding me along in my work and pushing me into situations I would have never entered in willingly. You helped to broaden my horizons, face my fears and develop as an engineer.

To Caroline Roberts, you were a sounding ear and guiding voice when I needed one. Thank you for urging me to become a STEM superstar and allowing me to find my own route to get there.

I must acknowledge the role Catherine Mavriplis has played in my life. Catherine, thank you for helping me to re-light the fire within. I was small and in pain and you lifted me up, encouraged me and reminded me that good Greek woman never lets her fury go to a dull roar.

Finally, I would like to acknowledge my friends in Lassonde and PSE, especially AB, PI, SS, HP, GB, NZA, RS, RL, AG, PE, GC, JR, and PD. Thank you for taking the time to get to know me, for helping me out when I needed it, teaching me the tricks of the trade and just letting me be me. You rock.

Table of Contents

List of Tables

List of Figures

List of Acronyms

AERI	Atmospheric Emitted Radiance Interferometer
AMSR-E	Advanced Microwave Scanning Radiometer for the Earth Observing System
API	Antecedent Precipitation Index
ARM	Atmospheric Radiation Measurement
AVHRR	Advanced Very High Resolution Radiometer
DSM	Digital Surface Models
ECV	Essential Climate Variables
ESA	European Space Agency
FPI	Fabry-Perot Interferometer
GCOS	Global Climate Observing System
GNSS	Global Navigation Satellite System
HIS	High-resolution Interferometer Sounder
LiDAR	Light Detection and Ranging
MODIS	Moderate Resolution Imaging Spectroradiometer
NIR	Near Infrared
RGB	Red-Green-Blue
SMAP	Soil Moisture Active/Passive
SMC	Soil Moisture Content
SMOS	Soil Moisture Ocean Salinity
SSM/I	Special Sensor Microwave Imager

UAS	Unmanned Aerial Systems
UAV	Unmanned Aerial Vehicles
VMC	Volumetric Moisture Sensor

1 Introduction

Equipped with his five senses,

man explores the universe around him

and calls the adventure

Science.

— Edwin Hubble, The Nature of Science, 1954

Flooding and droughts are two severe hazards directly linked to soil moisture content. Soils that are over-saturated cannot absorb surplus water, which can lead to increased surface runoff and flooding while soil that is overly dry, during drought conditions, do not provide the correct environment for seed germination and have a direct effect on the amount of plants that can be grown. This information can be used for famine early warning and provide drought risk assessment. In soil science, hydrology and agricultural sciences, water content has an important role for groundwater recharge, agriculture, and soil chemistry.

Satellite-based soil moisture data can provide a worldwide picture of soil moisture conditions and to understand if there is an anomaly present (significant difference between the average soil moisture condition for the specific time of year and what is

observed). The European Space Agency, ESA, has published historical soil moisture data sets and calculated anomalies (Figure 1-1and Figure 1-2) from Sentinel-1and Landsat-8 missions. Additionally, SMOS data is now available for public use as well, but limited to a 35 km ground resolution.

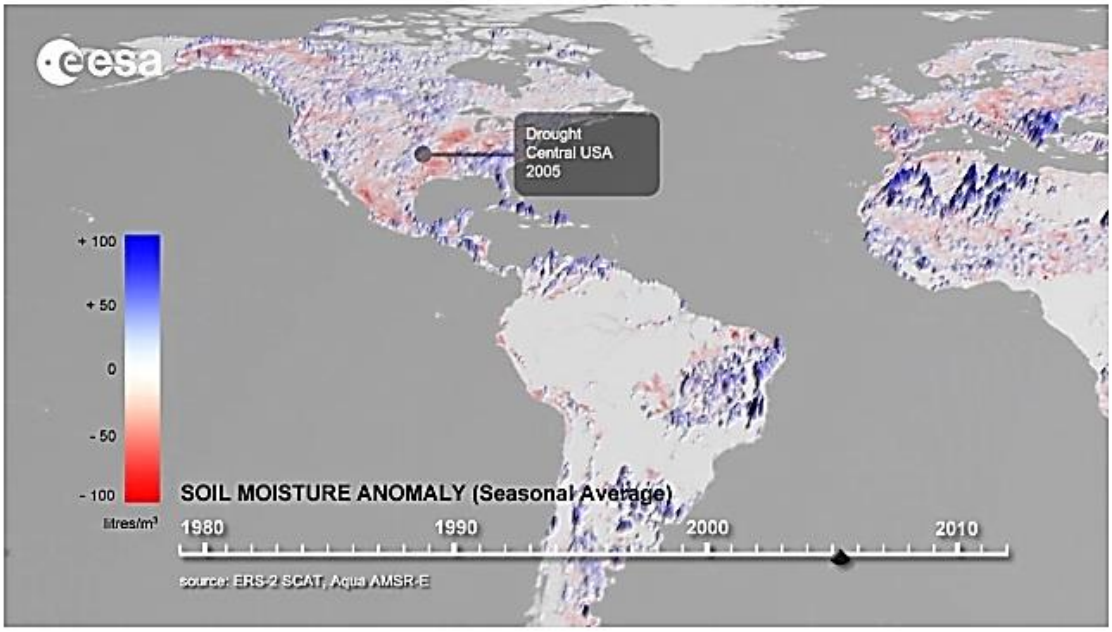

Figure 1-1 2005 Soil Moisture Anomaly for Americas [1]

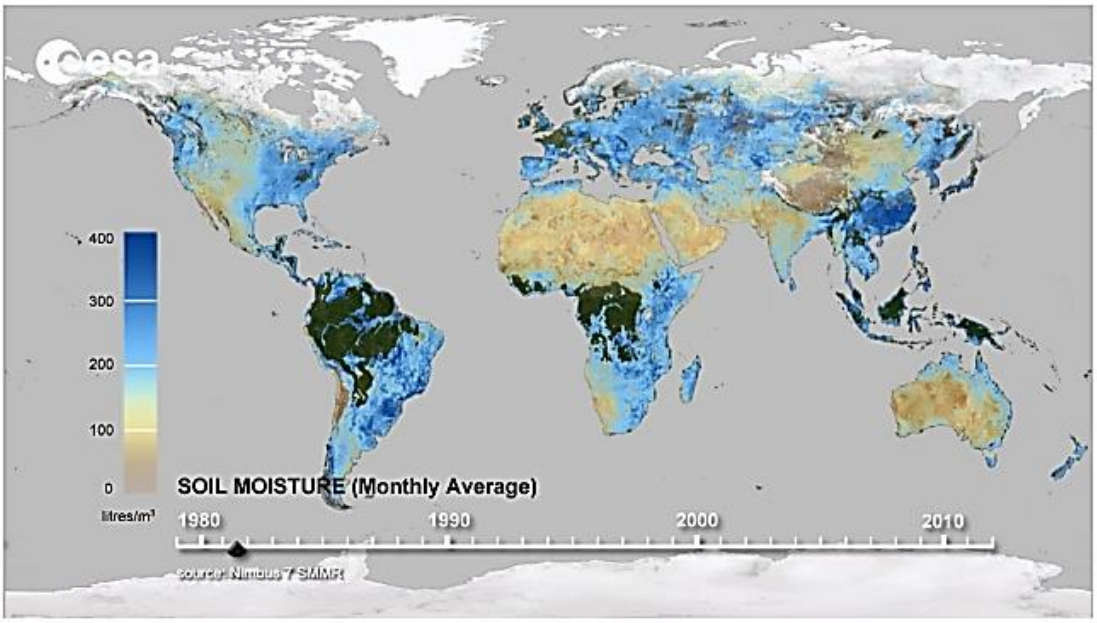

Figure 1-2 1982 Soil Moisture Monthly Average [1]

Due to its role in the climate system, soil moisture was recognized in 2010 as one of the Essential Climate Variables (ECV), which were defined by the Global Climate Observing System (GCOS) [1].

Plant growth is directly tied into how much water is located within soil and the percentage volume. Water plays many critical functions in the soil ecosystem including roles as a transporting agent, chemical solvent, readily available nutrient pool, source of water for metabolic activities of soil biota and vegetation, an as a factor affecting soil air composition and soil temperature.

The soil medium is an interconnecting hub for various elemental cycles. These cycles are comprised of a series of interrelated processes occurring within and between the atmosphere, hydrosphere, biosphere, and geosphere.

The water content held within the soil solution is sensitive to the major pulls and fluxes of the interacting within the medium. Soil water is an important component facilitating interactions within and between the atmosphere-biosphere-geosphere ecosystem components, while the overall examination of soil provides an interpretation of the behavior and transport of the dissolved and colloidal constituents in the soil environment [2].

The goal of this research program is to contribute in painting a worldwide picture of soil moisture in low vegetation areas, aiding with large scale agricultural monitoring and enabling the creation of a system to determine soil and agricultural inputs. When poor soil conditions are present, this can often lead to inferior crop health and survival [3]. Depending on where people are located in the world, this can correlate with reduced human conditions and reduced quality of life.

1.1 Research Objectives

This project aims to extend previous work performed using hand-held infrared scanners used to detect soil moisture content.

This research was supported by the Canadian Space Agency under the UTIAS led Micro-mission clusters pilots project [4].The project goal was to develop new instruments and mission concepts for interplanetary and lunar missions involving soil moisture

measurements from Earth orbit, geophysical measurements and high data rate volume antenna capabilities. The mission collaborators come from a variety of research laboratories at York University, University of New Brunswick, University of Winnipeg, and UTIAS.

The first objective is to determine the feasibility of detecting soil moisture content from space-borne infrared spectroscopy. The work is performed through a ground-up approach.

To accomplish this goal, several tasks have been identified. These are the main targets of my research:

1. Analyze spectral information of the atmosphere and determine the target detection range (wavelengths) for infrared spectroscopy;
2. Perform a full study and trade studies of a near infrared spectrometer (Argus 1000) components and suggest modifications to be used for soil moisture content measurements.
3. Prepare the design of a new spectrometer that would function in the determined target spectral range.
4. Prepare and test an Unmanned Aerial Vehicle (UAV) that is capable of performing spectral data acquisition fieldwork.
5. Determine if it is possible to move towards a full remote sensing observation model within the infrared region.

This research has resulted in the publication of two papers. The contents of the Argus 2000 design [5] are featured in Chapters 2, 3. This publication is a joint effort between Tsouvaltsidis, Al Salem, and Benari. Tsouvaltsidis performed the atmospheric analysis and hardware selection. Al Salem provided GENSPECT aid and data visualization while Benari wrote on the potential calibration methodology used for the instrument. In Tsouvaltsidis *et al.* [6] the hardware and data-acquisition system was showcased and the preliminary field results were shown and discussed. This material is reproduced in Chapter 4. Al Salem performed the Matlab figure production and Benari provided the analysis on how the UAV data would be compared to the data taken with the Argus 1000 instrument on CanX-2. Vrekalic aided during the design and development of the UAV system as well as aiding Tsouvaltsidis during the field surveys.

1.2 Thesis Organization

The thesis organization is as follows.

Chapter 1 discusses the thesis and research objectives. Research sponsorship is stated.

Chapter 2 provides a background introduction regarding the in-situ and space-borne measurement methods, describing differing technologies in use and their associated spectral range information. UAV platforms used for spectral research are also discussed.

Chapter 3 discusses GENSPECT's role in the determination of a spectral region for the NIR instrument to operate in; also providing the background heritage knowledge for Argus 1000. The new components chosen for the Argus 2000 build are examined.

Chapter 4 introduces the UAV platform, including details regarding the flight platforms used and the scientific payload. The UAV software development is discussed alongside the field campaigns.

Laboratory methodology for soil baking, radiometric and wavelength calibration, and spectral collection are shown in Chapter 5.

Chapter 6 present the results obtained for the calibration processes and space flight using the methodologies identified in Chapters 4 and 5 and their conclusions.

The overall thesis conclusion and sub-section conclusions are found in Chapter 7.

2 Literature Review

Gathering soil moisture content is often time consuming and expensive; the data is retrieved by hand through use of volumetric moisture sensors (VMC) or infrared scanners. This requires the use of many person-hours to visit the pre-determined test sites which are normally located far distances from each other. The resulting measurements, usually sparse, have a limited range to which their soil moisture content (SMC) finding applies. Space based microwave measurements can be used in conjunction with other data sets, such as volumetric moisture content measurements or remote sensing infrared data [7] to aid with missing measurements. The microwave based data often has low ground resolution and is not useful for agricultural applications. The equipment is expensive to launch into space as it requires large satellite systems. Within the soil science and soil health communities, there is a strong interest in the remote sensing of soil health and soil moisture content from space within the infrared region in order to produce more useful data. Most direct measurement methods provide estimates of SMC at small scales (approximately 10–100 cm) while remotely-sensed measurements of soil moisture represent larger scales (40–60 km), but these data lack the spatial resolution to be useful for most applications [8] [3].

Current in-situ methods for the measurement of soil moisture content are presented in Section 2.1 while 2.2 will introduce space-based measurements and approaches. UAV applications for obtaining remote spectral imagery will be reviewed in Section 2.3.

2.1 In-Situ Methods

2.1.1 Traditional Methods of Soil Moisture Representation

Gravimetric and Volumetric soil moisture content methods are two main traditional approaches used in field. Volumetric water content, Θ_V, is the portion of the soil volume occupied by the water given as a fraction while gravimetric, Θ_G, is based on the masses of the species, mainly the liquid contained in the soil and the overall soil mass. Both methods are related to each other by the bulk density of the soil [9], as seen in equations 2-1 and 2-2.

$$\Theta_G = \frac{m_{water}}{m_{soil}} = \frac{m_{wet} - m_{dry}}{m_{dry}} \tag{2-1}$$

$$\Theta_V = \frac{V_{water}}{V_{soil}} = \frac{\frac{m_{water}}{\rho_{water}}}{\frac{m_{soil}}{\rho_{soil}}} = \frac{\rho_{soil}}{\rho_{water}} * \Theta_G \tag{2-2}$$

The soil bulk density (ρ_{bulk}) is used for ρ_{soil} and is the ratio of soil dry mass to sample volume. The mass of the wet soil (m_{wet}) and dry soil samples (m_{dry}) are used to solve for the mass of water within the soil, m_{water}, and the mass of soil (without water content), m_{soil}.

The third traditional method is to use electrical resistance blocks to measure soil moisture content. This method is based upon the principle that electrical conductivity decreases in soil moisture. The experiment comprises of insulating blocks with two electrodes each a fixed distance apart. The blocks are buried in soil and the conductivity across the electrodes is measured with a modified Wheatstone bridge. The thicker the water films, the more ions that flow between the block's electrodes. Normally the blocks are placed at the vegetation root zone in order to provide a measure of the amount of water there. This is useful during crop season but much less so when it is time for seed planting and germination, as those processes occur closer to the soil surface [9].

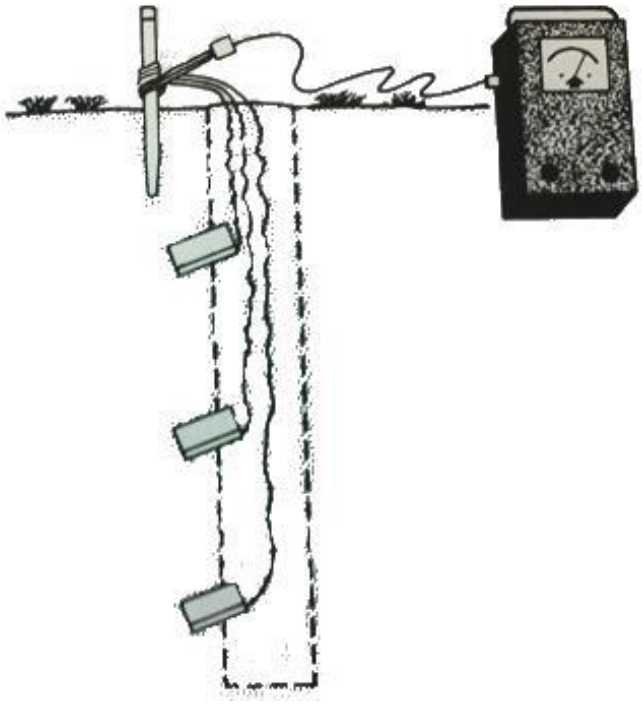

Figure 2-1 Measuring SMC with resistance blocks. [9]

In Figure 2-1, a typical resistance block field set up is shown. Electrical conductivity between two electrodes set at a fixed distance apart inside a small block in an indirect measure of soil moisture from the field capacity to the wilting point. The resistance blocks are fabricated from various types of materials such as gypsum, nylon, or fiberglass.

The movement of water occurs through soil and is directly related to the SMC value measured at any vertical height. Water can be displaced upwards or downwards through the soil through capillaries, which are very small pores. This process is called capillary rise and occurs differently through different types of soils and is dependent on the soil texture [10]. In very clay-filled sands (fine textured soils), the movement of water is slow but the water can travel long distances within the soil, while in very sandy soils (coarse textured) the movement of water is quick but the water can only travel a very short distance. Table 2-1shows normalized capillary rise values for soils with different textures.

Table 2-1 Soil Texture and Capillary Rise

Soil Texture / Soil Type	**Capillary Rise (cm)**
Coarse / Sandy	20-50
Medium	50-80
Fine / Clay	80 – several meters

Soil moisture can range from totally dry (0%) to soil saturation (100%). In soil, pores are present. It is within these pores that water rests. During soil saturation, there is no air left in the soil's pores – only water. When the soil is totally dry, the pores are only filled with air and not water. The SMAP (Soil Moisture Active/Passive) satellite, has mapped regions like the Sahara Desert to have SMC values ranging from 0-5%, while regions in Canada have shown 25-65% (averaged over a season, not showing daily variance).

2.1.2 Handheld Infrared Spectrometers

Handheld infrared spectrometers have also been utilized as a stand-alone method to measure SMC [11].The number of samples taken are increased but the approach still does not provide an accurate overview of the large regions being assessed. The spectral range utilized is from 1200 to 2400 nm with a spectral bandwidth of 1 nm. Goldshleger *et al.* [11] found significant spectral changes, in the three soil samples that they tested. These spectral changes are related to both particle size distribution and mineralogical composition.

Hardisky *et al.* [12] used a hand-held radiometer to collect spectral radiance data of the salt marsh planets in three wavelength bands 630 - 690 nm, 760 - 900 nm, and 1550 - 1750 nm. The NIR band 1550 - 1750 nm is sensitive to the water content while 630 - 690 nm and 760 - 900 nm bands are sensitive to the chlorophyll concentration and plant tissue structure respectively. The hand-held radiometer was held 140 cm or 88 cm above the canopy and levelled to a nadir pointing direction. They argue that soil salinity study would indicate that a strong relationship exists between the spectral radiance index and

leaf moisture content. Moreover, they observed that the relationship between the radiance index and moisture content was highly significant despite a small range in moisture content (12%).

O'Brien *et al.* [13] utilized a NIR hand-held spectrometer to quantitatively determine oil contamination in soil samples in the spectral interval 1150-2150 nm. They collected five spectra from each of the 48 oil-contaminated samples and showed a good agreement between the predictions of the mean spectra of the five test samples they determined and the reference values over the whole concentration range.

Bogrekci and Lee [14] investigated he effects of soil moisture content on the absorbance spectra of sandy soils with different phosphorus (P) concentrations in the spectral range from 225 nm to 2550 nm. They showed that the dried samples reflected more light than the moist samples which indicates that water is a strong light absorber in sandy soils. Their analysis showed that removing the moisture effect by spectral signal processing considerably improved prediction of phosphorus in soils.

Hummel *et al.* [15] measured the soil moisture contents and the soil organic matter by using a NIR spectrometer which operates in the spectral interval 1603–2598 nm. They normalized, transformed to optical density, and analyzed the spectral reflectance of the soil samples using stepwise multiple linear regressions. They concluded that the NIR soil moisture prediction can be more easily commercialized than can soil organic matter prediction, since a reduced number of wavelength bands are required (four versus nine, respectively).

When small regions are assessed by a handheld tool and approximately one measurement per square meter are made, and then a method is considered accurate, however, this approach is not readily adaptable to regional or global measurement [16].

2.2 Space-based Measurements

2.2.1 Earth Observation Satellites used for Soil Moisture Measurements

Gouweleeuw *et al.* [17] analyzed the influence of open water bodies on satellite-derived soil moisture retrievals from the Advanced Microwave Scanning Radiometer for the Earth Observing System (AMSR-E) for three areas in Oklahoma, USA. The AMSR-E data near-surface soil moisture retrievals (~2 cm) were derived from the microwave bands 6.9 GHz (C-band) and 10.7 GHz (X-band). They related the differences between the satellite data and on-ground and simulated estimates of SMC to dynamic estimates of open water fractions. These fractions are retrieved from a global daily record based on higher frequency AMSR-E data, from the Moderate Resolution Imaging Spectroradiometer (MODIS), and through inversion of the radiative transfer model, used to retrieve soil moisture.

Kerr *et al.* [18] described the Soil Moisture and Ocean Salinity (SMOS) mission which was developed to deliver key observations of land surface variables, including SMC. SMOS operates at low frequencies (L-band: 1.4 GHz, 21 cm) which is an established

technique for estimating surface soil moisture and sea surface salinity with a suitable sensitivity.

Entekhabi *et al.* [19]outlines the Soil Moisture Active/Passive (SMAP) mission which delivers soil moisture measurements in the L-Band range (1.41 GHz and 1.26 GHz). They showed that measurements of the radiometer L-Band are sensitive to soil moisture in the surface (0 to 5cm) layer. They stated that both active and passive SMAP measurements must be obtained at L-Band frequency in order to minimize the impact of vegetation on the soil parameter retrievals.

Chauhan *et al.* [20] developed an approach that links microwave-derived soil moisture estimates with optical/IR parameters. Their approach involves in two main steps. In step one the brightness temperature is inverted from passive microwave remote sensing measurements using a simplified radiative transfer model. In the second step, the estimation of the soil moisture in the microwave region at low resolution is related to the scene optical/IR parameters such as land surface temperature and surface albedo. Their technique which is applied to data from the Special Sensor Microwave Imager (SSM/I) and Advanced Very High Resolution Radiometer (AVHRR) was compared to in-situ soil moisture measurements and related issues were discussed.

Choudhury and Golus [21] utilized NIMBUS-7 Scanning Multichannel Microwave Radiometer (SMMR) and the NOAA-7 Advanced Very High Resolution Radiometer (AVHRR) data to obtain improved estimates of soil wetness. They argued that their

estimator was found to provide four levels of soil wetness using Antecedent Precipitation Index (API) model.

2.2.2 Microwave Radiometry used for Soil Moisture Measurements

In remote microwave radiometry measurements, there are many different frequencies being used to obtain ground brightness temperature. The most commonly used frequencies are 1.4 GHz ([22]; [18]; [23]; [24]; [25]), 5.5 GHz [23], 6.7 GHz [25] and 10.7 GHz ([23]; [24]; [25]). The spatial resolution also varies with the satellite instrument, but mostly ranges from 50 [22] to 150 km [25], which can be considered too large a spatial distribution to be computing an overall soil moisture value over.

Often ground measurements are used for validation purposes. These ground measurements are not numerous, with sometimes only having one to five measurements taken, and at times not performed on the same day as the microwave readings are recorded [25].

On the MODIS mission, the microwave soil moisture measurements are combined with overall soil health measurements taken by an infrared spectrometer onboard and are validated by the use of handheld infrared spectrometers on ground. The onboard infrared spectrometer provided the overall soil health measurements and was combined with microwave data retrieved and space telemetry information in order to increase ground resolution to up to approximately 10 km [7].

2.2.3 Reflected Multipath GNSS signals

A novel technique for the measurement of soil moisture and snow pack measurements exists through the use of signal to noise ratio (SNR) recorded by high precision GPS

receivers. Since these receivers are already in place for geodetic uses, a network of measurement systems can be easily implemented. The GPS receivers measure the direct GPS signal and noise. The noise measurement comes from the reflections of the original GPS signal as it bounces off of the ground or other objects. This noise can come in and out of phase with the direct GPS signal and will result in the SNR value recorded to resemble a sine-wave. This sinewave's phase and frequency are dependent on the amount of snow on the ground or water in the soil. It is believed that by recording this data as it changes over time, a methodology will be developed to retrieve continuous SMC and snow depth measurements from a high precision GPS network [26].

Figure 2-2 shows a sample measurement taken from the Research Applications Laboratory (RAL) at the National Center for Atmospheric Research in the USA. The grey measurements were taking by traditional moisture probes while the red dots were measured using SNR measurements from a GPS receiver.

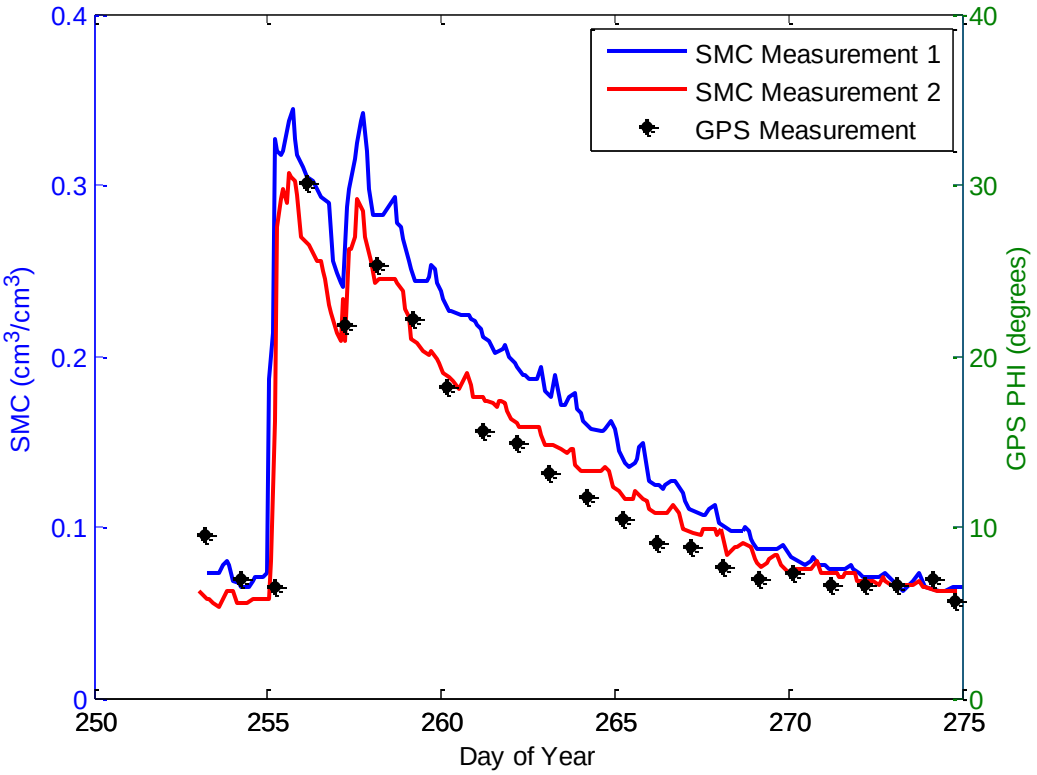

Figure 2-2 SMC measurements taken from high precision GPS receiver (adapted from [26])

In order to further expand the regions where this technique can be used, the RAL is studying how GPS signals and reflections can become further complicated in regions like forests due to surrounding trees and bush [26].

Larson *et al.* provide a methodology to aid in the quantification of SNR oscillations and multipath amplitude due to the satellite-reflector-antenna geometry [27]. Using multipath reflection amplitudes taken at a GPS site in Uzbekistan over a period of 10 days, SMC data is derived and compared to estimates from the Noah land surface model. Although the GPS multipath amplitudes and the land surface model are uncalibrated, it was noted

that both sets of theoretical and actual measurements rose sharply following each rainfall event and slowly decrease over a period of time.

2.3 Airborne Spectral Data Collection Methods

Saari *et al.* [28] developed an Unmanned Aerial Systems (UAS) that consists of a Fabry-Perot Interferometer (FPI) based hyperspectral imager and a high resolution false color imager for forest and agriculture applications. The FPI based hyperspectral imager operates in the spectral range 500-900 nm at selectable spectral range from 10 nm to 40 nm. The 5 mega- pixel CMOS image sensor used in the spectral imager prototype an on-chip ADC which provides 12-bit dynamic range per pixel. The Unmanned Arial Vehicle (UAV) imaging system consists of GPS receiver, downwelling irradiance sensor, autopilot, VIS-NIR spectral camera with compact flash memory, and high resolution false color camera with compact flash memory. Their preliminary analysis shows the possibility of generating high resolution Digital Surface Models (DSM) from false color images. Johnson *et al.* [29] developed a small UAV to collect digital RGB (red-green-blue) and hyperspectral imagery in the spectral range from 480 nm to 880 nm above San Bernabe Vineyards in California. The high spectral resolution data that they collected in 580 channels were used for examination of canopy reflectance differences as related to crop vigor. The UAV used in this field campaign supported a payload of five kg. When drawing 40 watts of power it remained aloft for up to eight hours, using an altitude ceiling of 3000 m.

Figure 2-3 Sample Octocopter used for Hyperspectral Imaging [30]

Hakala *et al.* [31] developed a Fabry-Perot interferometer based spectral imaging system which operated in the spectral range of 400-1000 nm. It was primarily for applications that required detailed surface spectral information to be obtained. They investigated a new method based on in-situ irradiance measurements for the radiometric correction of UAV imagery that has been collected in variable imaging conditions. vonBueren *et al.* [32] developed four optical UAV-based sensors (high spectral resolution spectrometer, RGB camera, converted near-infrared camera and six-band multispectral camera) for precision agricultural applications. They used two different UAV systems; QuadKopter and a Falcon-8. The spectrometer (Ocean Optics STS-VIS) operates in the spectral range 338-824 nm with spectral resolution 3 nm, field of view 12° and weight of 216 g. A ground-based spectrometer that covers the spectral range from 325 nm to 1075 nm for comparison with all UAV sensors flown in their study.

Revercomb *et al.* [33] developed airborne instruments for UAV use. These instruments are the High-resolution Interferometer Sounder (HIS), the Atmospheric Emitted Radiance Interferometer (AERI) and the new AERI-UAV for application in the DOE Atmospheric Radiation Measurement (ARM) Program. The AERI-UAV has the capability to remotely sense temperature and water vapour, while observing the upwelling and down welling solar radiation. It was designed to take nadir measurements from the UAV with 100 mrad angular field of view and operates in the spectra interval 7-24 microns with spectral resolution 0.5 cm^{-1}.

Mac Arthur *et al.* [34] developed a lightweight spectrometer for environmental monitoring (upwelling and downwelling solar radiation) from a UAV platform. The spectrometer (QE Pro by Ocean Optics) operates in the very near infrared (VNIR) region from 400 nm to 1000 nm. Another spectrometer with the spectral interval 1000-1700 nm is under development.

Chao *et al.* [35] developed a small UAV for cooperative remote sensing for real-time water management and irrigation control. Three types of UAV platforms were tested including off-the-shelf Procerus UAV, Xbow UAV with open source software, and Parparrazi UAV with both open source software and hardware.

During the summers of 2007 and 2008, Berni *et al.* [36] flew UAV platforms over agricultural fields, obtaining thermal imagery in the 7.5–13-μm region (40 cm spatial resolution) and narrow-band multispectral imagery in the 400–800 nm spectral region (20 cm spatial resolution). Wallace *et al.* [37]developed a low-cost Unmanned Aerial

Vehicle-Light Detecting and Ranging (UAV-LiDAR) system to provide an unrivalled combination of high temporal and spatial resolution datasets. The aim of this system is to present development of a UAV-borne LiDAR system using lightweight and low-cost sensors, and demonstrate its capability of collecting spatially dense, accurate, and repeatable measurements for forestry inventory applications.

Valencia *et al.* [38] used 2.5-meter wingspan UAV. During a 45-minute flight, the UAV's L-band radiometer collected sea shore and land data. Turner *et al.* [39] used a multi-rotor electric powered UAV system for hyper resolution vineyard mapping based on visible, multispectral, and thermal imagery. Archer *et al.* [40] used AutoCopter-XL, a small unmanned helicopter that can fly autonomously or semi-autonomously to measure the soil moisture in the L-Band (1.4-GHz).

3 Argus 2000

This chapter outlines the work performed to address the first three targets of my research; (1) analyze spectral information of the atmosphere and determine the target detection range (wavelengths) for infrared spectroscopy; (2) perform a full study and trade studies of a near infrared spectrometer (Argus 1000) components and suggest modifications to be used for soil moisture content measurements, and (3) prepare the design of a new spectrometer that would function in the determined target spectral range.

The Argus 1000 near infrared spectrometer is the chosen hardware that the Argus 2000 instrument is to based off of because of its availability within the laboratory, access to the issuing company's design team for Argus 2000 design feedback, and its size and cost to manufacture.

Section 3.1 chapter discusses the background modeling tool used to produce a spectral range for the Argus 2000 instrument and its outcomes. Section 3.2 reviews the current Argus 1000 instrument while in 3.3, the trade studies performed for the determination of the Argus 2000 optical instrumentation are presented. The Argus 2000 instrument is a derivative of the Argus 1000 instrument featuring a chassis redesign, new detector, different operational wavelength region, new radiation filter and chassis material.

3.1 Spectral Modelling for Water Detection

3.1.1 GENSPECT

GENSPECT is a spectral modeling tool used in atmospheric, climate and environmental studies [41]. Using GENSPECT, an atmospheric model is created in order to see if a

spectral window exists within the infrared spectrum where an instrument could take ground measurements without atmospheric interference. Wavelength regions which can be used for differing atmospheric constituent's column measurements are noted. The GENSPECT tool allows for user input in order to create a synthetic spectrum to suit ones needs.

GENSPECT is the atmospheric modelling tool used for my research due to availability of the software within the laboratory, and research team familiarity with the tool, and the internal use of the HITRAN database.

3.1.2 Geo-Parameters and Atmospheric Constituents

GENSPECT is used to compute the absorption parameters of the atmosphere. This is achieved by generating synthetic spectra using the HITRAN 2000 database to obtain the mixing ratios of the gases in the standard atmosphere to be simulated. The synthetic atmospheric spectrum is converted to radiance in order to be comparable to the spectra a space instrument would see. GENSPECT uses an estimate of the nadir angle of the instrument, an estimate of the spacecraft sun angle, and albedo values to generate synthetic spectra observed using those parameters. The error tolerance of the synthetic spectra produced can be set to either 1%, 0.1%, and 0.01%, based on end-use requirements [41].

The synthetic spectra produced by GENSPECT has been used for comparative purposes with data collected by Earth observing instruments such as MOPITT-A, MOPITT, ACEFTS, and MAESTRO [42].

The SWIR region allows direct observation of absorption by molecular processes including the concentration of soil moisture (considered to be water).

purposed The zenith viewing angle was assumed to be zero in order to mimic a nadir viewing geometry, mimicking the physical parameters required when performing measurements from a satellite orbiting Earth. Measurements made during the local-geographical day allow for photons reflected off the Earth's surface to be measured. Measurements may also be acquired during local-geographical night however much longer integration times are required. This causes an undesired decrease in spatial resolution. This is imperative as without the knowledge of what a space based sensor would see, then research item 5 (determination of if it is possible to move towards a full remote sensing observation model within the infrared region) could not be completed.

For surface parameters, the surface was set as smooth with a reflectance of 0.35, which corresponds to the value for wet soil [43]. The surface was chosen to be smooth in order to mimic the surface reflecting all incident energy that it receives from the sun. The other input variables set are incident angle and reflected angle, assumed each to be zero, Earth surface temperature set to 300°K, and solar temperature set to 5980°K. The resolution used was 0.001 cm^{-1}, while the forty (40) grids were created and set to be altitude weighted.

The main constituents taken into account for the GENSPECT atmospheric model are CO, CO_2, N_2O, CH_4, O_2, O_3, and H_2O. These constituents were chosen as infrared photons are most absorbed by these molecules and to suit the research purpose of

measurement through the atmosphere in the infrared region [44]. Each atmospheric constituent was checked for any temporal changes in their mixing ration levels. Only one constituent value has changed enough to warrant a review of the mixing ratio values – CO_2. According to Tans [45], CO_2 has risen from 351 ppm in 1995 to 398 ppm in 2013. A more recent atmospheric mixing ratio was unavailable however resulting in the original values used.

There are three main water regions associated with soil moisture content and the reflectance curve obtained through use of infrared spectroscopy; 1400 nm, 1900 nm, and 2100 nm. The water absorption feature at 1400 nm is due to the first overtone of the O-H bend, while 1900 nm water feature is attributed to a fundamental O-H stretch and O-H deformation. The 2100 nm characteristic is related to a combination of the third overtone of the O=H bend, C-O stretch and C-O-C stretch for cellulose and other carbohydrates [44].

The wavelength region of 1700 to 2200 nm was examined due to the regions where hygroscopic water can be measured in the infrared. Evans *et al.* [46] and Goldshleger *et al.* [11] both performed broad spectral imaging of soils in the infrared regions, showing hygroscopic water dips at 1400 nm, and 1900 nm (note two arrows pointing upwards labelled Hygroscopic water). Evans does not show a location for hygroscopic water at approximately 2150 nm, as seen in Figure 3-1, while Goldshelger's data, seen in Figure 3-2, shows a secondary dip at 2200 nm [11].

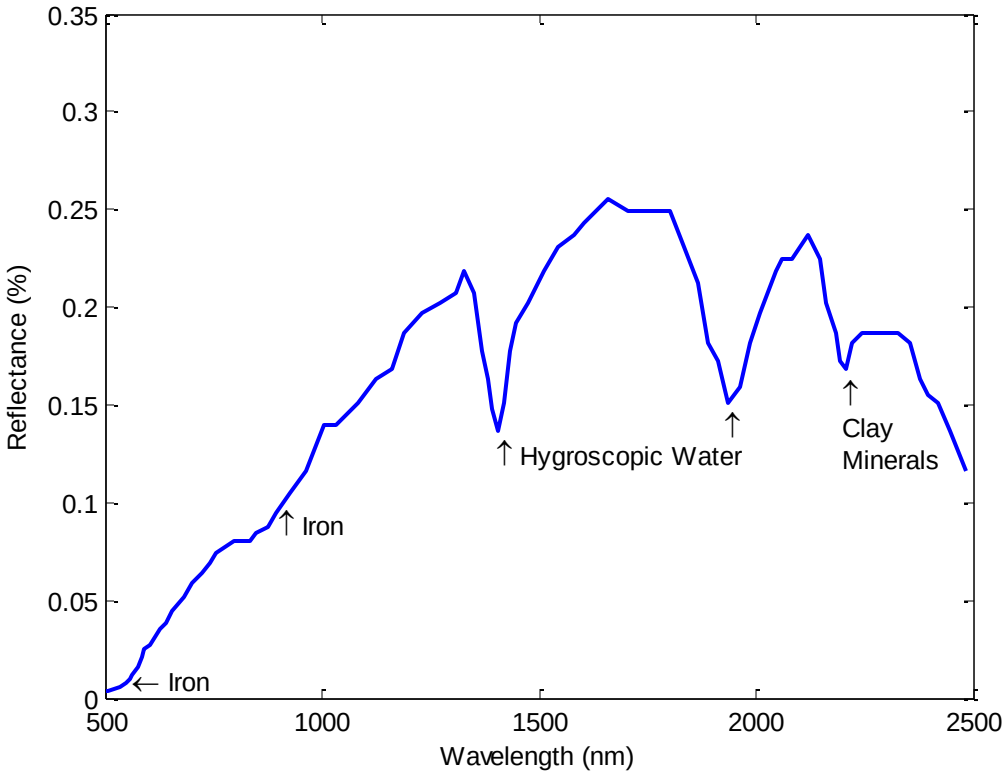

Figure 3-1 VNIR-SWIR spectra of soil, showing important spectral locations (adapted from [46])

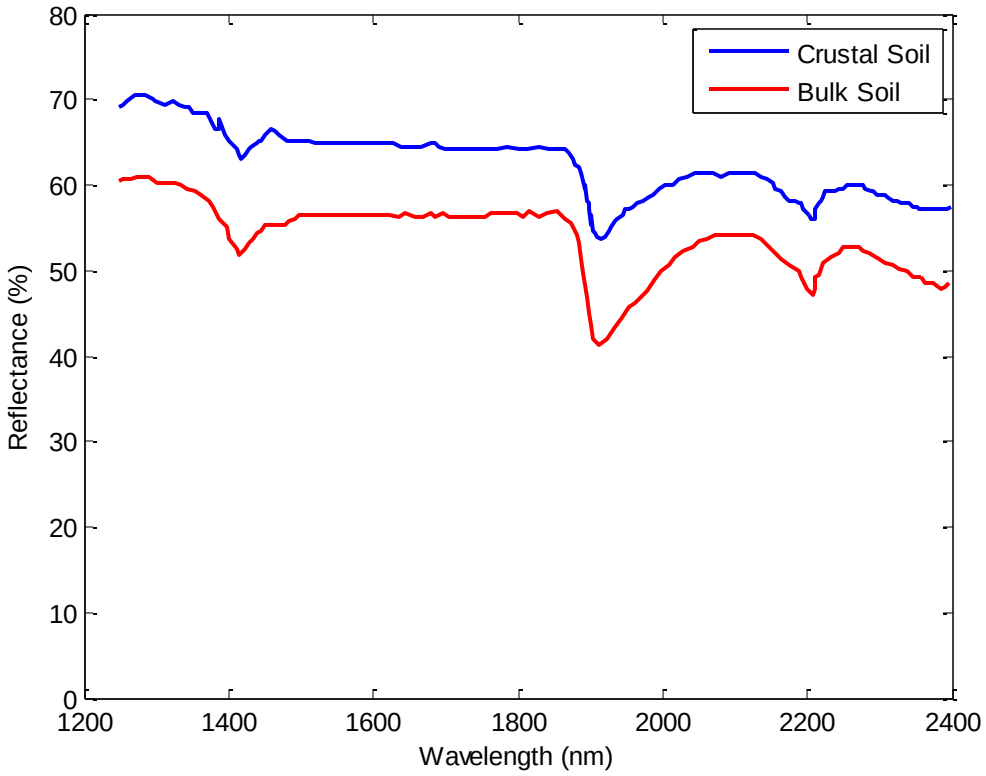

Figure 3-2 Hamra soil reflectance (adapted from [11])

Both figures relate to the soil crust and not deep underlying soil. Soil crust is the uppermost layer of the soil, which would be visible to an infrared instrument in space. This is the layer which would be viewed from space through remote sensing methods. The reflectance value has strong shifts at certain wavelengths, mainly approximately 1400 nm and 1940 nm. These wavelength values have been specifically mentioned by Goldshleger to contain vital soil health information, including soil moisture content [11].

3.1.3 Spectral Modelling of Water

The GENSPECT program was run in order to observe the individual behaviors of each atmospheric constituent and their overall combination. A general model reflecting the near-infrared spectrum was produced in order to see the main areas where atmospheric interference occurs.

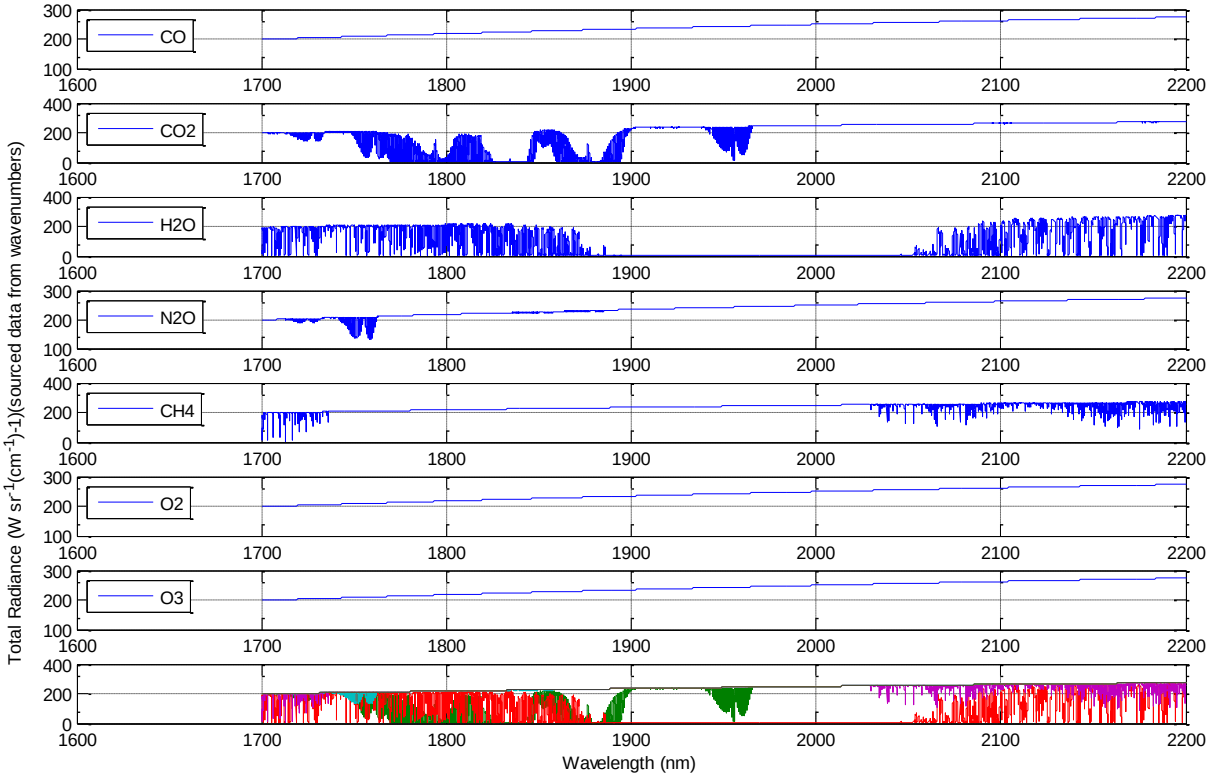

Figure 3-3 GENSPECT atmospheric outputs

Figure 3-3 showcases the synthetic spectra of each individual constituents produced by the GENSPECT software. The y-axis represents the total radiance (W* Sr^{-1} * $(cm^{-1})^{-1}$), calculated from wavenumber data, while the x-axis is the wavelength in nanometers. The lowest plot shows the total combined synthetic spectrum which is expected to be observed from space. The linear regions seen in the spectral graphs showcase where zero atmospheric interference are observed. The regions where atmospheric interference occur are visible and are represented by the dark regions which travel downwards from the radiance line in the y-axis. Any region which travels downwards from the radiance line is not usable for remote infrared measurements. The bottom graph in Figure 3-3 I total combined synthetic spectrum. Figure 3-4 shows a more detailed view of the total combined synthetic spectrum.

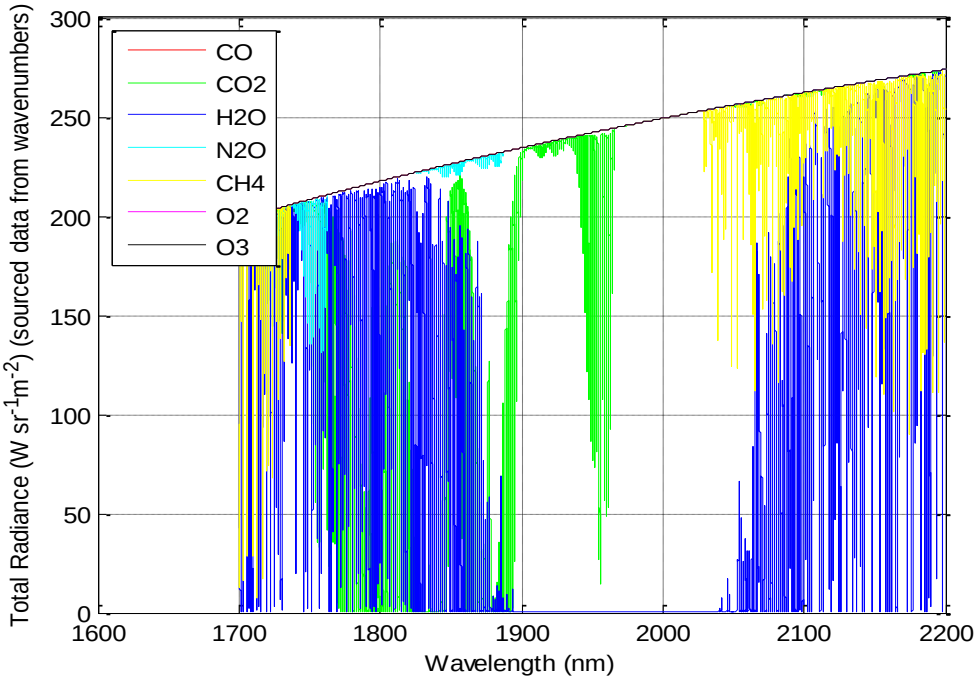

Figure 3-4 Total combined synthetic spectrum

The region of 1965 and 2020 nm wavelengths showcases a potential area for Earth based observations. The Argus 2000 spectrometer that will be used for the laboratory experiments will aim for 5 nm pixel resolution, allowing for multiple pixel measurements to be made at both 1965 and 2020 nm wavelengths. This aids in providing a better idea of a small spectral window that may be useful towards the remote sensing of soil moisture. The Short Wave Infrared Region (SWIR) corresponds to the area which is known to contain soil health information, including soil moisture content [5]. From Figure 3-4 certain regions of the spectrum can be made to take column measurements, specifically CO_2 and H_2O. From this, a region of 1600 nm to 2200 nm is identified to take spectral

measurements in. Specifically, the modelling shows that the region of 1965 nm that corresponds to the theoretical hydroscopic soil content are potentially useful for measurements from space. This is seen in Figure 3-5. From this modelling set, the desired spectral range for the Argus 2000 instrument has been obtained (1600 nm to 2200 nm). This wavelength region includes the atmospheric window which has been previously discussed and that will be used to ascertain if varying levels of SMC can be measured.

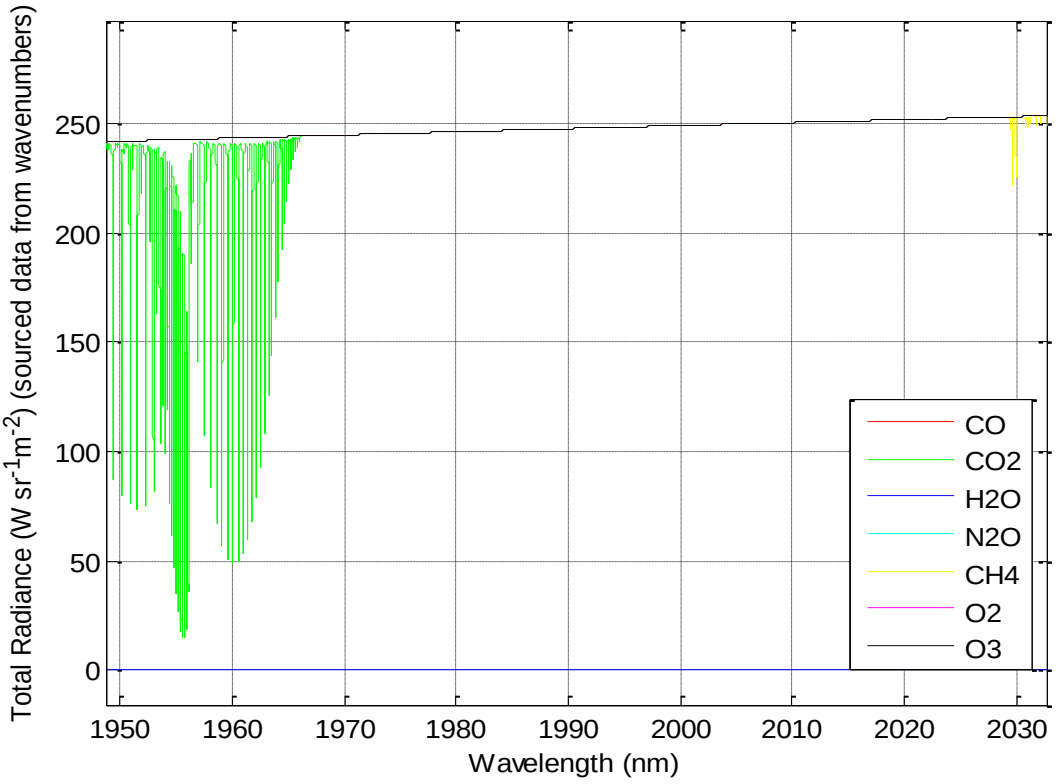

Figure 3-5 Zoomed in wavelength regions

3.2 Argus 1000

The Argus 1000 instrument is a near infrared (NIR) grating spectrometer, measuring spectra from 900 to 1700 nm. The Argus instrument has flown aboard CanX-2 since 2008 [47] and has been used to study various atmospheric constituents. At 228 g and a spectral resolution of 6 nm, the Argus is a great instrument to use for space based spectral measurements [48]. Currently the Argus 1000 spectrometer has features seen in Table 3-1 (adapted by [48]).

Table 3-1 Argus 1000 Spectrometer Specifications (adapted from [48])

Argus 1000 Spectrometer Specifications	
Optics	Grating Spectrometer
Configuration	Single Aperture
Field of View	2.18 mRad viewing angle around centered camera bore-sight with 15mm fore-optics
Mass	228 g
Accommodations	40 mm x 50 mm x 80 mm
Operating Temperature	-20 to +40
Survival Temperature	-25 to +50
Detector	265 element InGaAs Linear Array
Grating	300 grooves/mm plane grating (12mm x 12mm)
Spectral Resolution	6 nm
Operational Modes	1: Continuous cycle, constant integration time 2: Continuous cycle, adaptive exposure 3: Single shot
Data Delivery	Fixed length parity striped packets of single or co-added spectra with sequence number, temperature, array temperature, and operation parameters.
Integration Time	500 μs to 4.096 s
Calibration	Five-wavelength laser calibration and radiance calibration
Volatiles	Less than 0.1% volatile internals by mass.
Exposure Environment	Clean-room class 10,000 or better recommended. Class 1,000 required for optical or internal inspection.
Signal to Noise Ratio	120:1
Dark Noise	11 RMS counts
Power Consumption	2.4 W (max)

For the new spectral range of 1700 to 2200 nm to be observed, a modified version of the Thoth Technology micro-spectrometer Argus 1000 was designed and built. The component changes that were to the made to the instrument in order to maximize the measurement of soil moisture content in the SWIR region.

3.3 Instrument Design

This section describes on the trade studies and design work performed in order to manufacture an infrared spectrometer which would be able to detect radiation within the desired wavelength region identified in 3.1.3. The original design is based upon the Argus 1000 instrument as described in 3.2. b

3.3.1 InGaAs Linear Array

Linear arrays are linear focal planes that are composed of individual detectors. An InGaAs linear array is a specific type of array mean to detect light in three specific IR ranges 900 to 1700 nm, 1100 to 2200 nm or 1100 to 2600 nm. There are many other options such as detector height, pixel pitch and the number of pixels in the array to consider when choosing a linear focal plane array.

Table 3-2 Linear plane focal arrays (adapted from [49])

Linear Focal Plane type	**Pitch (µm)**		**Pixel Heights (µm)**			**# of pixels**
	25	**50**	**1.7**	**2.2**	**2.5**	
LX		X	50, 500	50, 250	250	256, 512
LD/LDB	X		500	250	250	512
LSB		X	500	250	250	256
LE	X		25, 500	250	250	1024
LSE		X	500	250	250	512

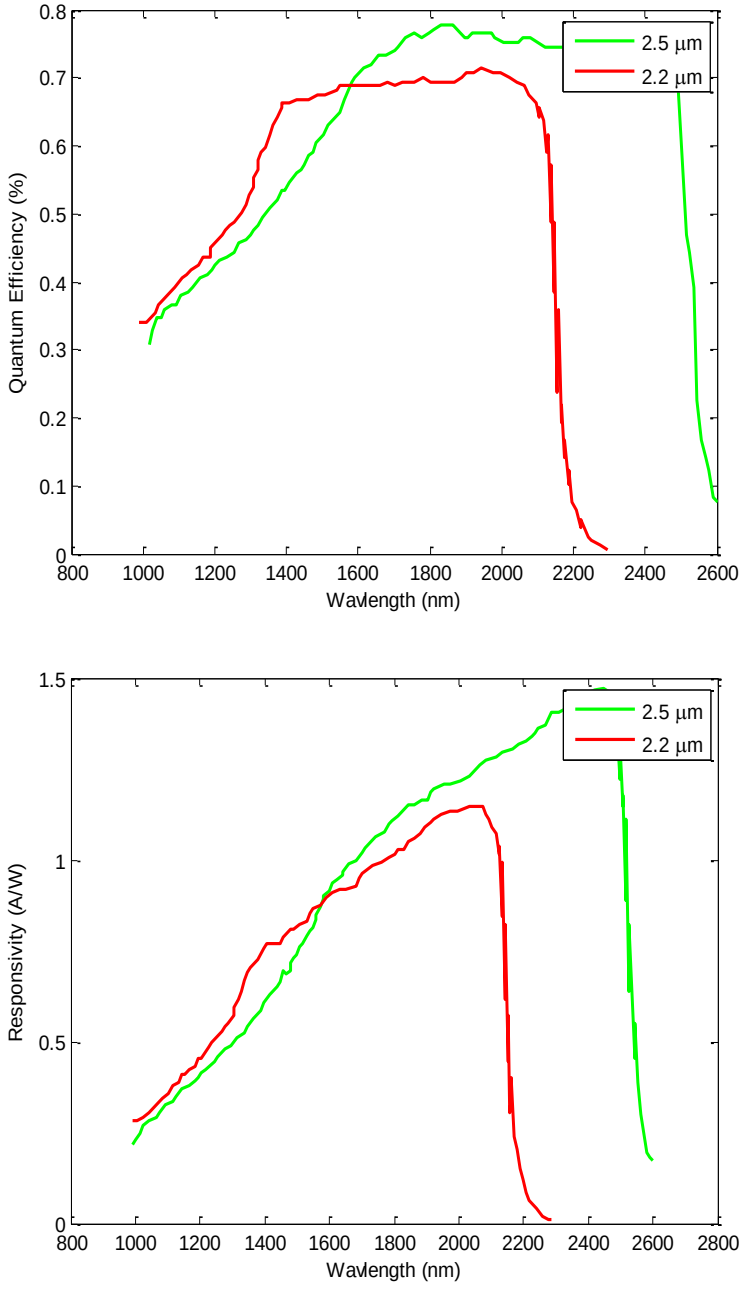

Figure 3-6 Comparison of 2.2 and 2.5 µm cut-off wavelengths (adapted from [49])

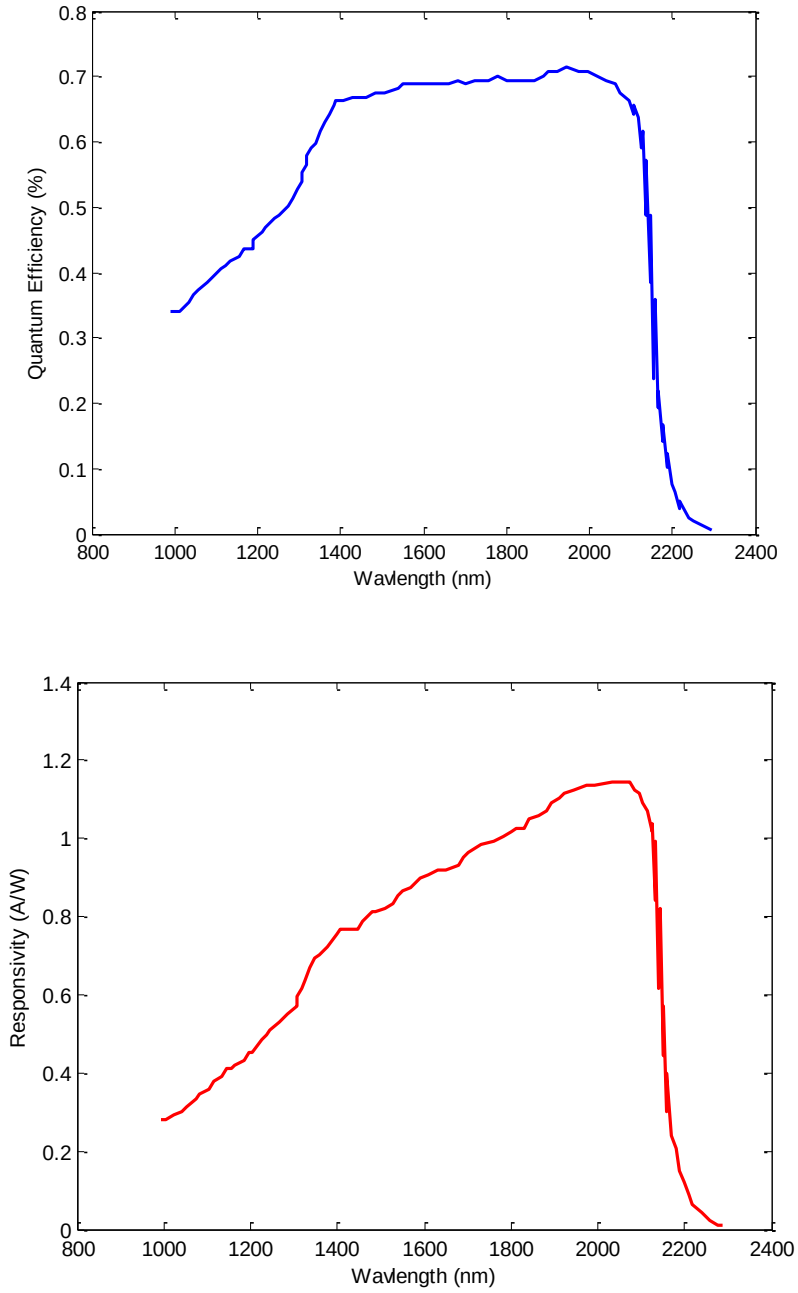

Figure 3-7 Responsivity and QE of 2.2µm cut-off linear array (adapted from [49])

The design requirements for the detector are a 50 µm pitch, pixel height of 250 µm and a minimum of 256 pixels. This eliminates the LD/LDB and LE options, leaving LX, LSB, and LSE.

The cutoff of 1.7 µm was eliminated as this would not allow for measurements in the desired spectral region. The Quantum Efficiency and Responsivity of the linear arrays varies according to the spectral sensitivity of the linear plane array. The Responsivity of the linear plane array increases in values from the start of the spectral range to the end of it, whereas the QE is mainly stable in the spectral region of interest. The new spectral range that the Argus 2000 will measure has a Responsivity of 0.9 to 1.1 from while the QE is found to be 0.65 to 0.7 in the spectral range 1700 nm to just below 2200 nm. Responsivity measures the optical input– electrical output gain of a detector system, measured in amperes per watt. The Responsivity and QE showcased by the 2500 nm cut-of linear array also performs well. The major comparative note was the pricing. The 2200 nm cut-off linear array was far more reasonable. From this, a cutoff of 2.2 µm was chosen.

The design of the Argus 2000 system is both similar and different to its predecessor, Argus 1000. The overall optical flows and electrical systems are similar with the distinction of each subsystem modified for a different wavelength system. The design differs from the original in its chassis size, uses new linear arrays, grating, and detector, and a redesigned electronics board in order to accommodate the new wavelength region.

each system was reviewed and had trade studies performed on it. The current InGaAs Linear Array model used for the Argus 1000 was studied and compared to the LSB model which came recommended by Sensors Unlimited, Inc. Because the new versions are to measure in a new spectral region, and make the system as similar to the other versions commercially available, the LX model of InGaAs Linear Array was studied and compared to the LSB model which came recommended by Sensors Unlimited, Inc. The comparisons are seen in Table 3-3.

Table 3-3 InGaAs Linear Array options [50]

Model	**SU256LX-2.2T1-0250**	**SU256LSB-2.2TI-0250**
Version Notes	Older style, Obsolete	State-of-the-art, currently available
Price	Premium pricing as is no longer being made/sold	Standard pricing
Number of Pixels	256	256
Pixel Height (µm)	250	250
Pixel Pitch (µm)	50	50
Spectral Sensitivity end (µm)	2.2	2.2
Cooling Method	One-stage TEC cooling	One-stage TEC cooling, newest technology
Detector Packaging	T1	T1

As seen in Table 3-3, the SU256LX-2.2T1-0250 InGaAs Linear Array is considered obsolete technology and is no longer being commercially available. It also features a one-stage TEC cooling system. Conversely the SU256LSB-2.2TI-0250 InGaAs linear array is considered to be state of the art and is currently available of the market, featuring the latest technology in one- stage TEC cooling. When comparing the spectral sensitivity, number of pixels and pixel height and pitch, both the current model and LSB are the same. The SU256LSB-2.2T1-0250 was chosen due to availability and improved cooling

system potentially resulting in enhanced data collection. The physical length of the detector in this chip measures to 12.5 mm, which is used in order to solve for the new optical design [49] [50]. The sizing of the SU256LSB-2.2T1-0250 array is seen in Figure 3-8.

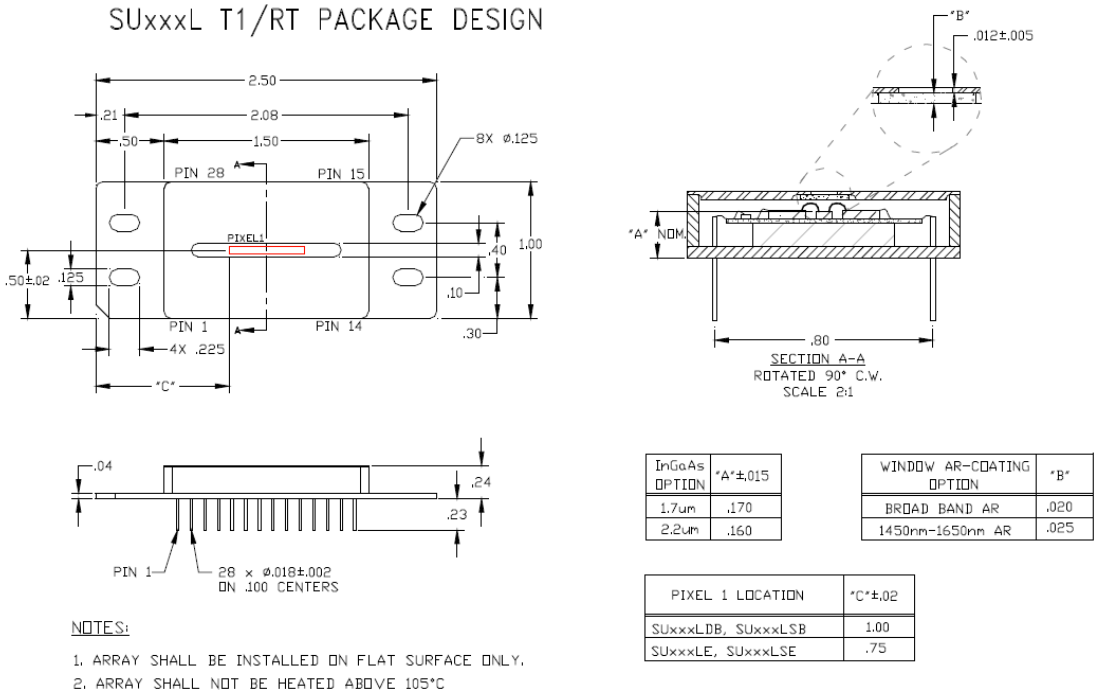

Figure 3-8 SU256LSB-2.2T1-0250 Sizing (adapted from [49])

3.3.2 Gratings

In order to properly understand how the new spectrometer was to be formed, the grating system was examined. In the non-extended range versions of Argus, 300 groves/mm gratings are used. These gratings are blazed with a laser set to the optical range at which the spectrometer is to observe at. This is done to increase optical performance.

The gratings available on the market vary in the number of grooves and the blazed wavelength at which they are manufactured. An example of availabilities is seen in Figure 3-9.

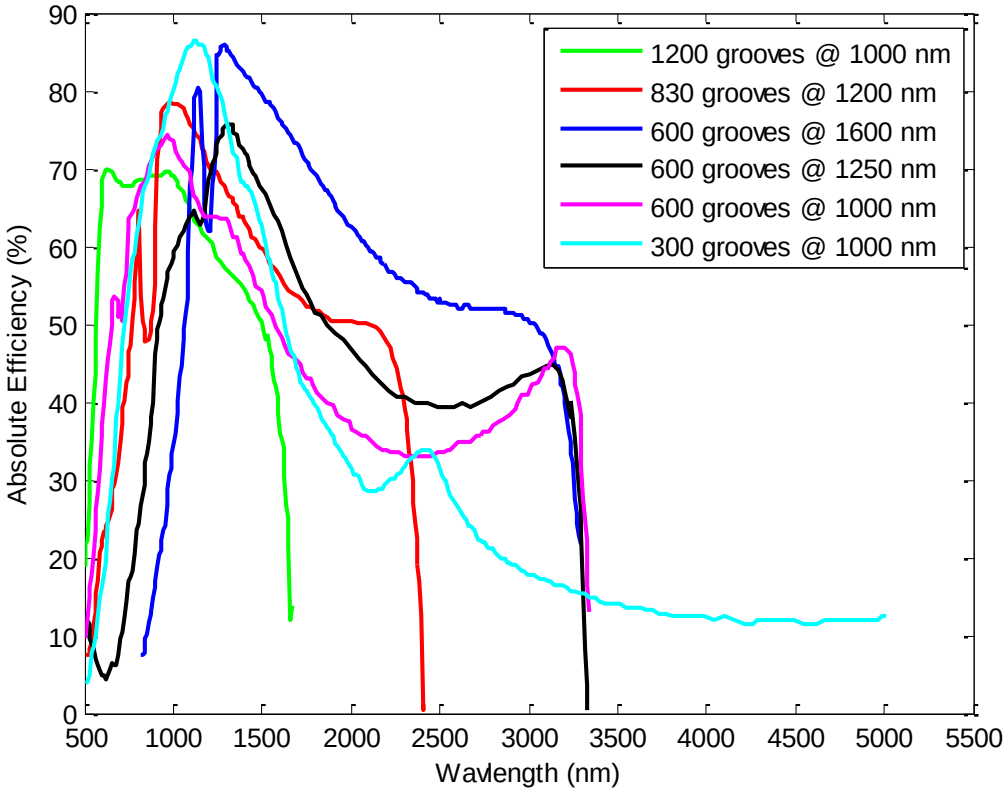

Figure 3-9 Grating efficiencies (adapted from [49])

For this examination, both the theoretical use of 300 g/mm and 600g/mm were studied and compared. Their potential wavelength outputs and absolute efficiencies are reviewed and compared. Using an Optical Design Layout Thoth Technology proprietary MATLAB tool, the potential wavelength output was studied. The design results are seen in Table 3-1 and respectively in Figure 3-10 and Figure 3-11.

Table 3-4 Argus 2000 Optical Design Results

Parameters Studies	**Matlab Outputs Using**	
	300 g/mm	**600 g/mm**
Focal Length (mm), Order Number, Mirror Length (mm)	Focal length: 35; M:1; Mirror:35	Focal length: 35; M:1; Mirror:35
Grating Offset in X (mm)	12	15.5
Chassis Coordinates X (mm)	[-40 40]	[-40 40]
Chassis Coordinates Y (mm)	[-25 30]	[-25 55]
Length of Spectrum on Linear Array (mm)	12.45	11.01
Spectra Max/Min (nm)	1200/2200	1700/2200
Optimal Grating Angle (deg)	-10	20

In the optical diagrams, the dark blue lines represent the input optics, black represents the spectral length of the dector, while the spectrum at 2200 nm is comprised of the red line (2200 nm) and the light blue line (1200 nm or 1700 nm, grating dependant).

As seen in Figure 9, the 300g/mm grating allows for a smaller chassis and more easily placed grating. This optimized grating angle was found to be the same of the current Argus 1000 model, allowing for less internal structure change. The length of the spectrum on the linear array is 12.45 mm, which is closest to the maximum of 12.5 mm and allows for a larger spectral range of 1200 nm to 2200nm.

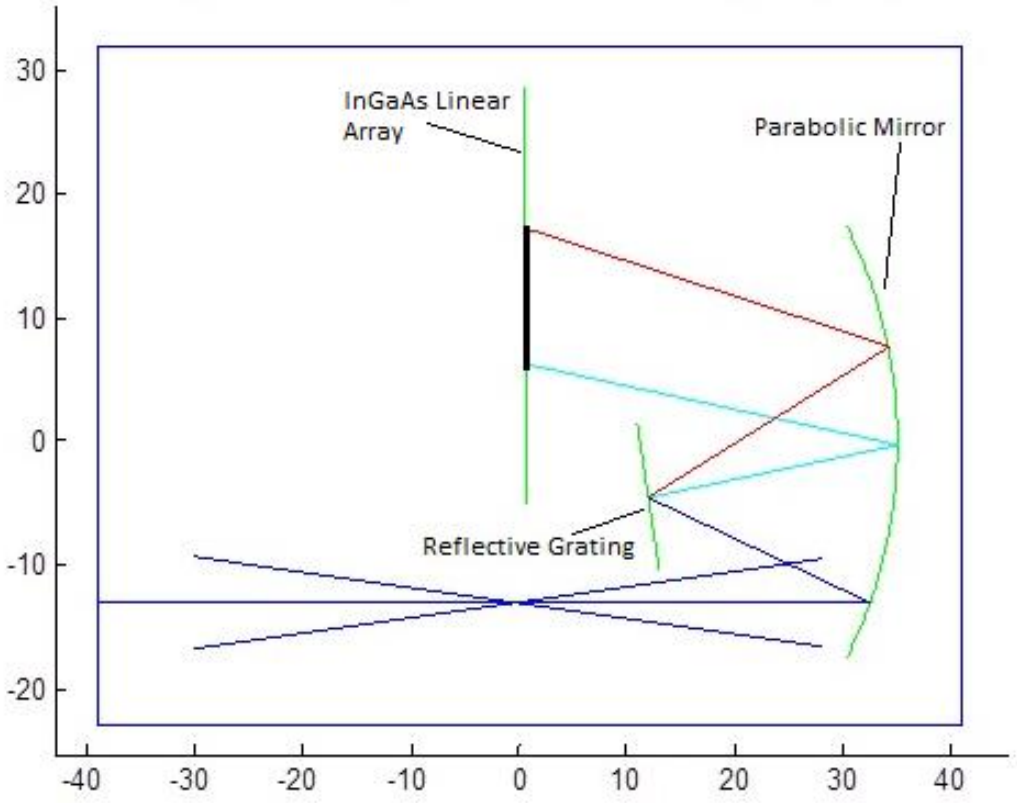

Figure 3-10 Argus Optical Design Layout (300g/mm)

The 600 g/mm solution uses a mm larger chassis in the y-coordinate while remaining equal to the 300 g/mm soluntion in the x-coordinate. In order to achieve a maximum spectral range and meet the maximum length of spectrum on linear array requirement, the grating offset is changed to 15.5 mm in the x-coordinate.

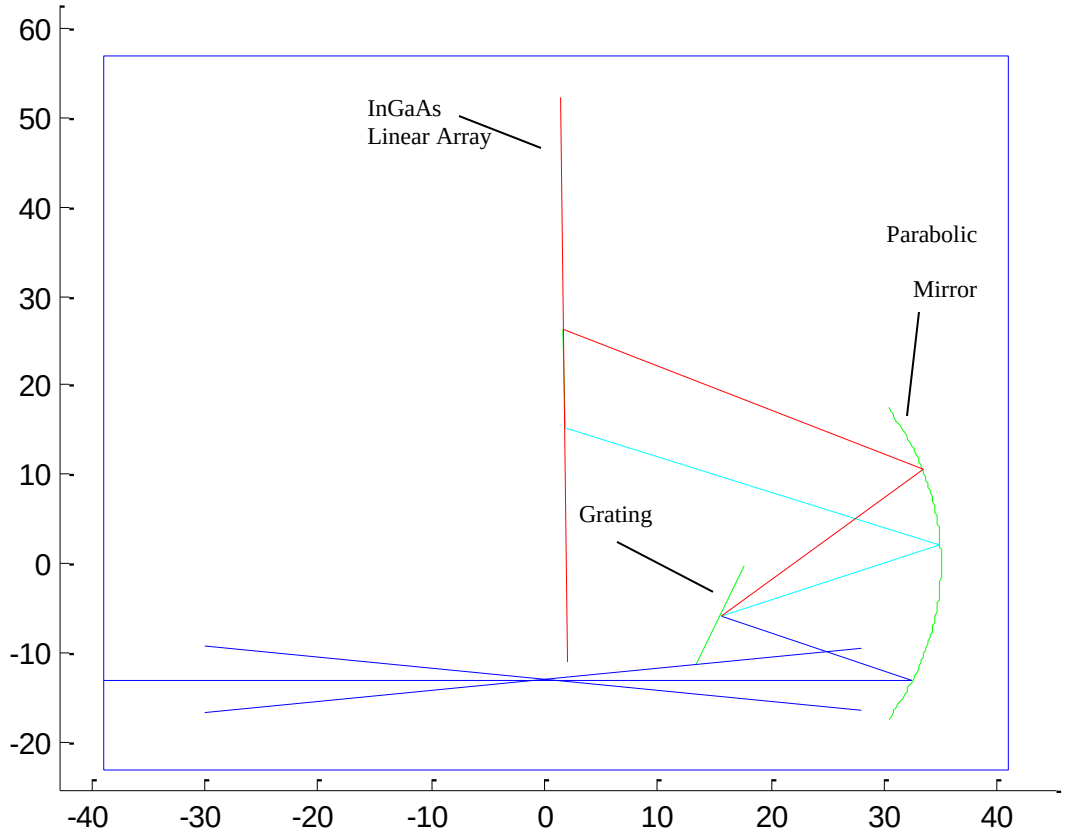

Figure 3-11 Argus Optical Design Layout (600g/mm)

Next the efficiency curves for both the 600 g/mm and 300 g/mm gratings are considered. In the desired spectral range , it is seen from Figure 3-9, it is seen that the 600 g/mm blazed at 1600 nm shows the best absolute efficiency, while 300 g/mm shows poor effciency. From the effiency percentages the 600 g/mm grating blazed at 1600 nm is chosen for the Argus 2000 design.

The opitcal design layout follows the schematic diagram in Figure 3-12. The input optical rays first interact with the lens. Then the rays are wavelength filtered before interacting with the mirror. The rays are bounced off to the mirror into the grating. The grating separates the rays into specific wavelengths and reflects them onto the mirror. The mirrror is then used to reflect the rays onto the detector, the final target.

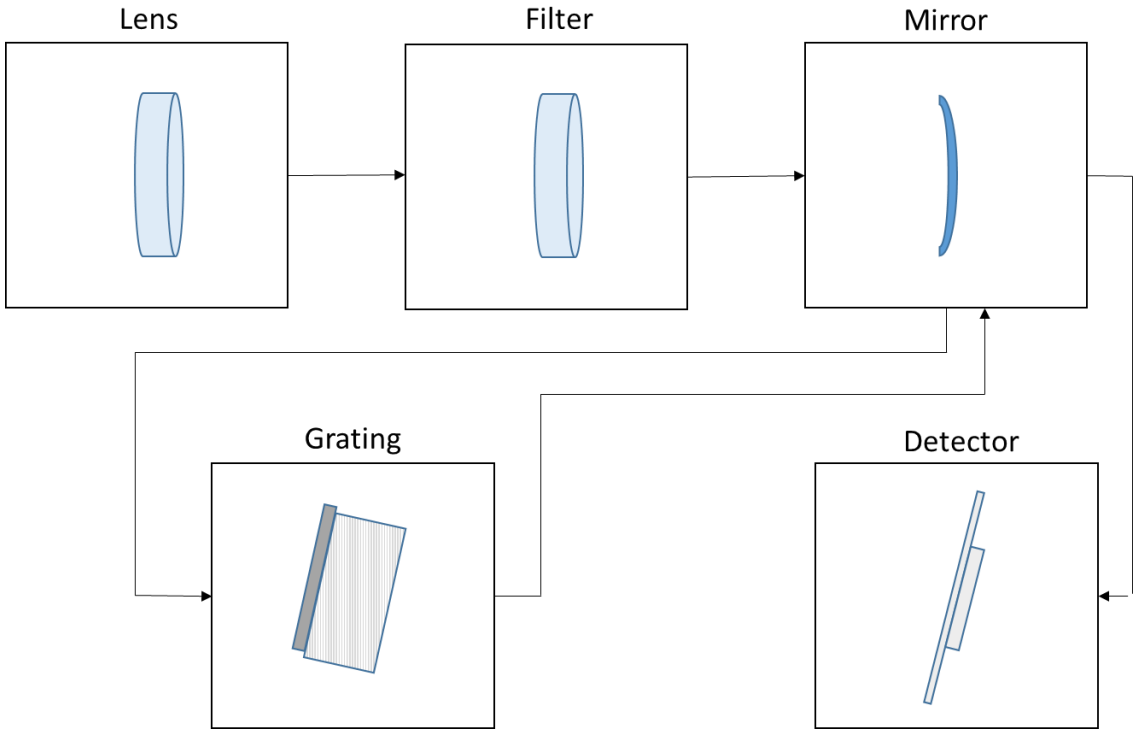

Figure 3-12 Argus 2000 Schematic Diagram

3.3.3 Hastings Triplet Achromatic Lenses

Hastings Triplet Achromatic Lenses are typically used in a spectrometer design in order to provide distortion-free, high-powered magnification [51]. The lenses are designed to interact with each other in order to eliminate pincushion distortion and spherical

aberrations. Two concave meniscus elements are cemented to a double convex lens to create the triple lens system [51]; visually represented in.

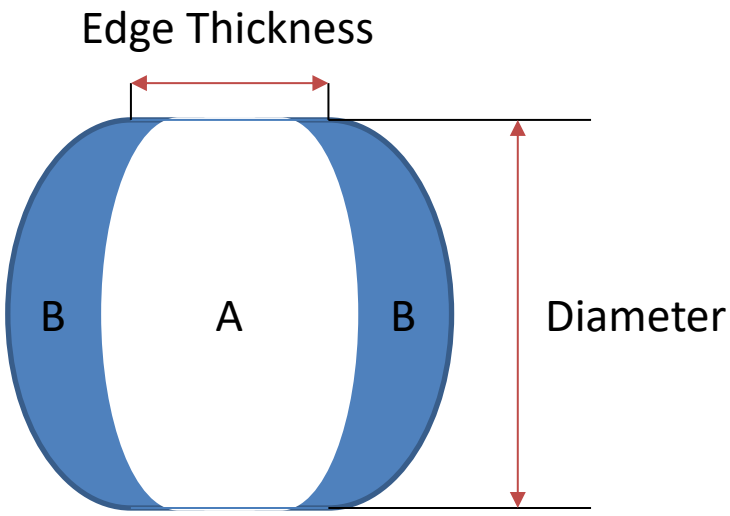

Figure 3-13 Hastings Triplet Achromatic Lens (adapted from [51])

To calculate the final value for the transmittance of the glass plate, the values sourced from Schott North America [52] [53] are used. Two main elements are used in the production of these lenses. Elements A and B. The letters A and B in Figure 3-13 are Schott glass N-BK7 517/642 (A) and N-F2 620/364 (B) [54]. The transmittance values for both of the materials in the desired spectral range are shown in Figure 3-14, with the values being retrieved from Schott North America, Inc.'s Optical Glass Datasheet. The transmittance values decrease as the wavelength increases in value. The decrease ranges

from slightly nominal, as seen in material B at a 10 mm thickness, to rather vast in material A at a 25 mm thickness. Transmittance is thickness dependent, which is seen in Figure 3-14. Both materials A and B have lower transmittance values at the higher glass thickness. In order to better understand how these values will propagate into the larger achromatic lens, the values found are propagated into a final transmittance quantity for the entire lens.

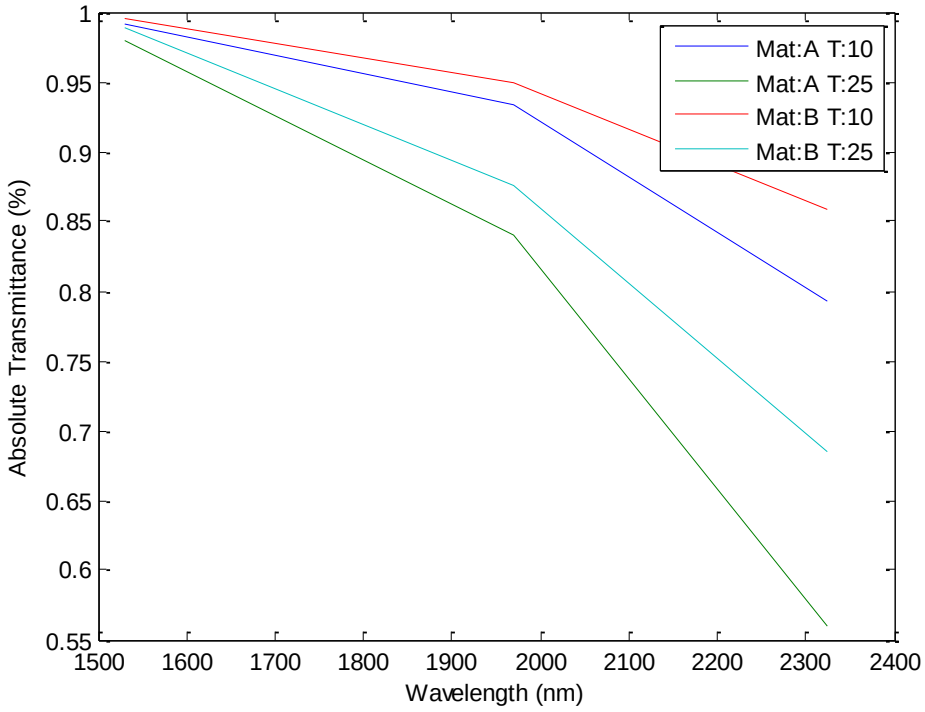

Figure 3-14 Absolute Transmittance of N-BK7 517/642 (A) and N-F2 620/364 (B)

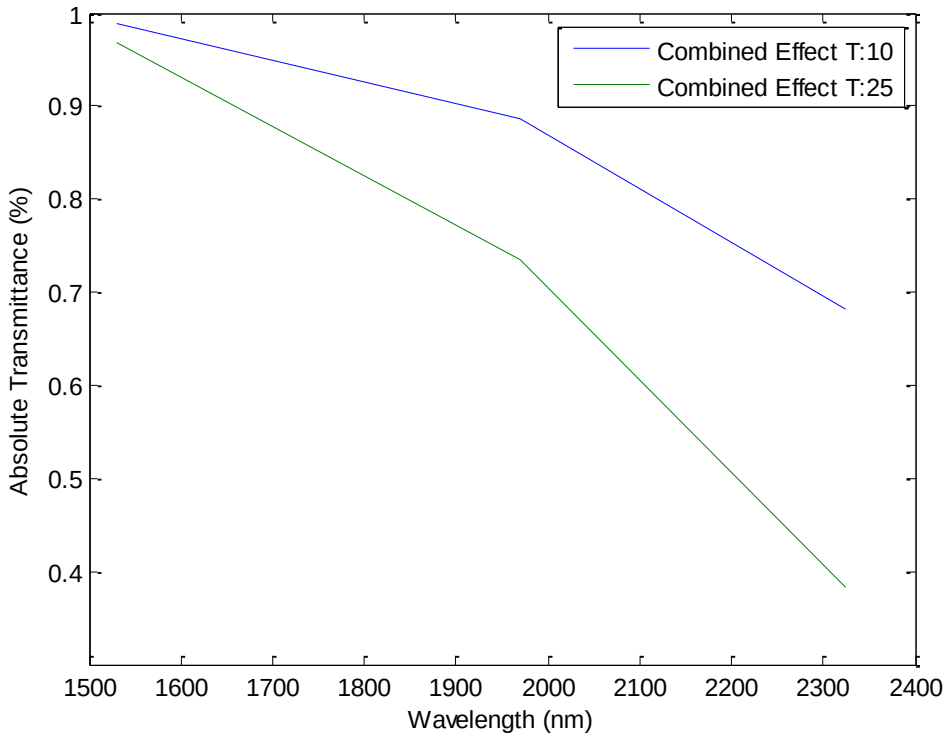

Figure 3-15 Combines effect of Absolute Transmittance of Materials A and B

The transmittance of an optical glass is inversely proportional to its spectral absorption which is strongly related to the glass's dispersion behavior. This dispersion is a measure of the change of the refractive index with wavelength. Since the measurements are to be taken in the infrared spectrum, the influence of the infrared transmittance is taken into account. The infrared transmittance is mainly influenced by the O-H content placed during the glass melt to form the lens. The O-H absorption bands typically occur between 2.9 µm and 4.2 µm [55]. The sudden decrease seen in the absolute transmittance in Figure 3-14 and Figure 3-15 are indicative of the absorption bands [52].

From this, the thickness of 10 mm is chosen.

3.3.4 Optical Filters

To block the lower wavelength light from being detected on the InGaAs linear array, a filter is used. The Techspec 1600 nm Longpass OD>2.0 filter was purchased from Edmund optics. On the company website, the transmission specifications reflect only those seen in Figure 3-16 from 1400 nm onwards [56]. When the filter arrived, upon inspection it was seen to be clear through the optical, as seen in Figure 3-17. This immediately was cause for concern as it indicates the filter does not stop the transmission of visible light. This hypothesis was confirmed upon speaking to Customer Support and obtaining the full transmission specifications for this filter, reflected in Figure 3-16.

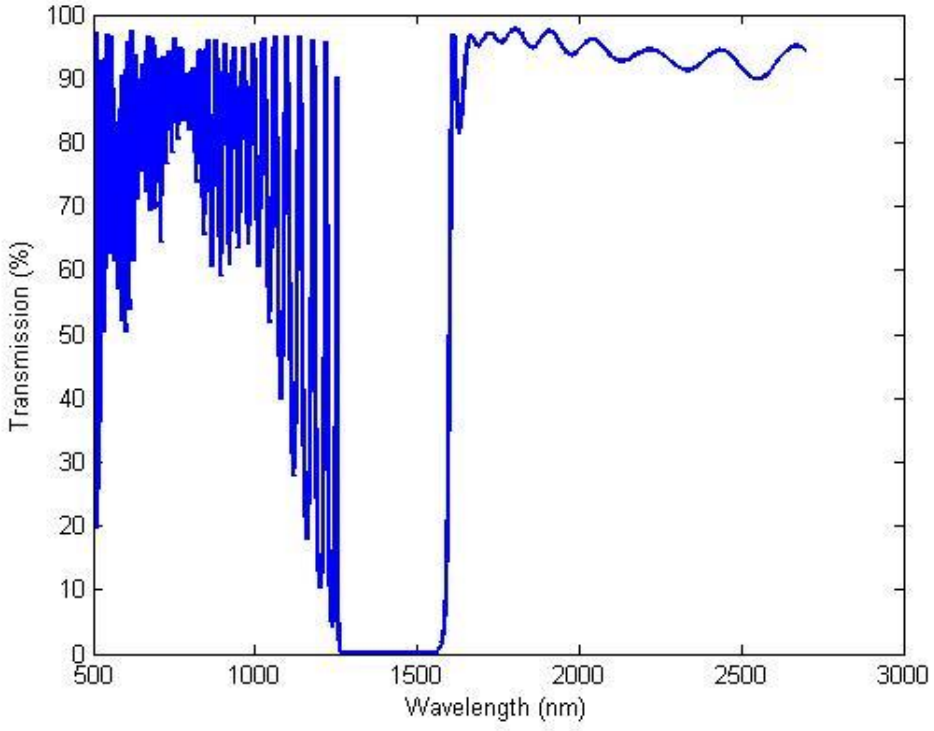

Figure 3-16 Techspec 1600 longpass filter (adapted from [56])

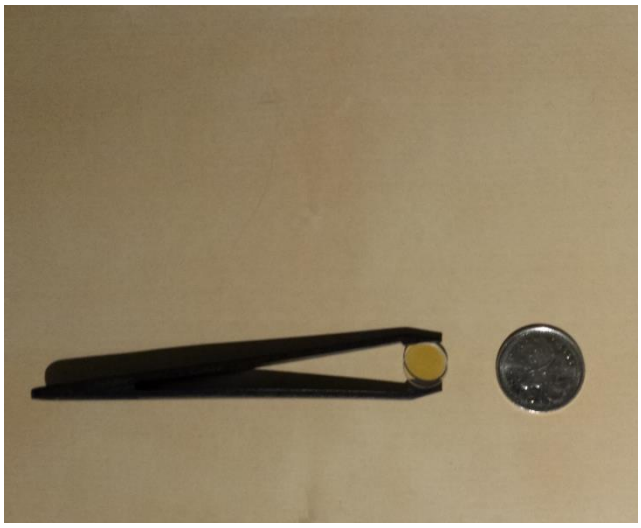

Figure 3-17 Transparency of Techspec 1600 nm longpass filter

Due to market availability, a suitable substitute for the Techspec 1600 nm longpass filter was unable to be sourced. Instead a secondary filter was acquired; FELH1300 from Thorlabs. This filter's duty was to ensure that the visible region which the Techspec allowed through was to be blocked. The filter transmission data clearly showcased a blockage of all radiation up to 1300 nm where transmission then begins to occur, observable in Figure 3-18 [57]. This was confirmed upon arrival of the filter as seen in Figure 3-19.

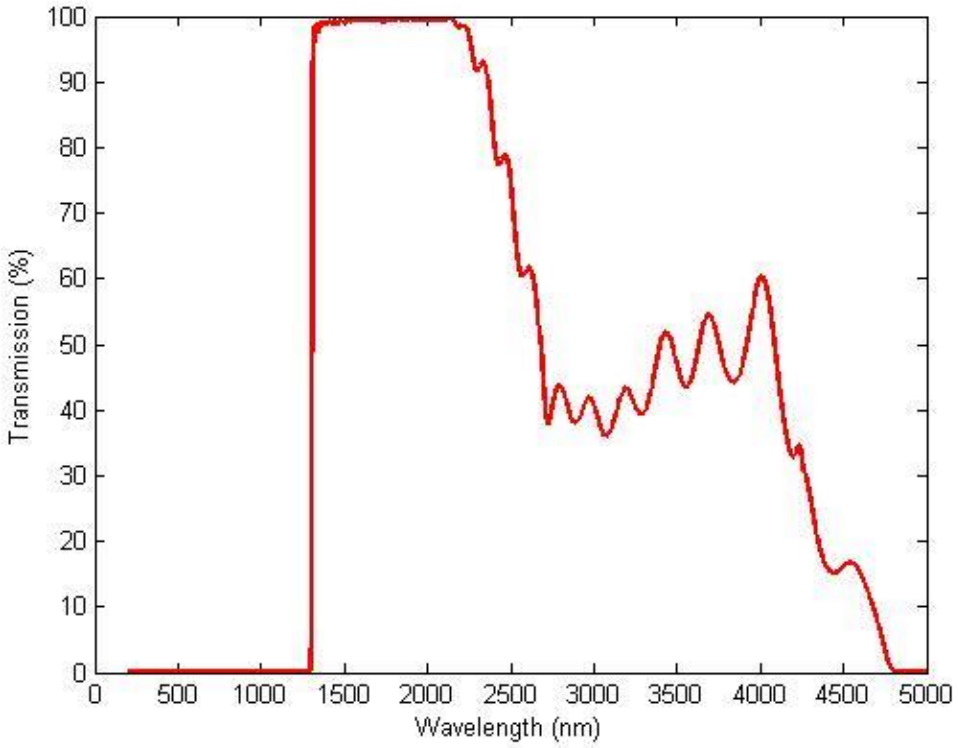

Figure 3-18 Transmission data for Thorlabs FELH1300 (adapted from [57])

Figure 3-19 FELH1300 longpass filter

The combined filter transmission data is graphically showcased in Figure 3-20. The Thorlabs FELH1300 longpass filter allows for radiation in the NIR and VIS to not be seen by the detector while the Edmund Optics Techspec 1600 nm long pass filter properly applies the radiation start to equate with 1600 nm. The transmission in the desired spectral region is a function of both filter's transmission information.

In order to determine how the combined transmission is measured, it is imperative to be able to determine if the radiation viewed by the Argus 2000 instrument is coherent or incoherent. Coherent emissions have the same wavelength as original photon did and are in phase (coherent) with original source whereas incoherent does not. Examples of

coherent light sources are lasers and collimated light from the Sun while the Quartz Tungsten Halogen lamp and un-collimated solar light that will be used for instrument calibration is considered to be incoherent [58] [59] [60].

The combination of filters for coherent and incoherent light is not simply the product of the individual transmissions (T ≠ T1*T2). Multiple-path interference results in the transmission of coherent light through two filters to be solved through the use of Equation (3-1) where L is the separation between the two filters and λ is the wavelength [61] .

$$T = \frac{T_1 T_2}{1 + (1 - T_1)(1 - T_2) - 2\sqrt{(1 - T_1)(1 - T_2)\cos\left({}^{2\pi L}/_{\lambda}\right)}} \qquad \textbf{(3-1)}$$

The transmission of incoherent light can be solved for using Equation (3-2).

$$T = \left(\frac{1}{T_1} + \frac{1}{T_2} - 1\right)^{-1} \qquad \textbf{(3-2)}$$

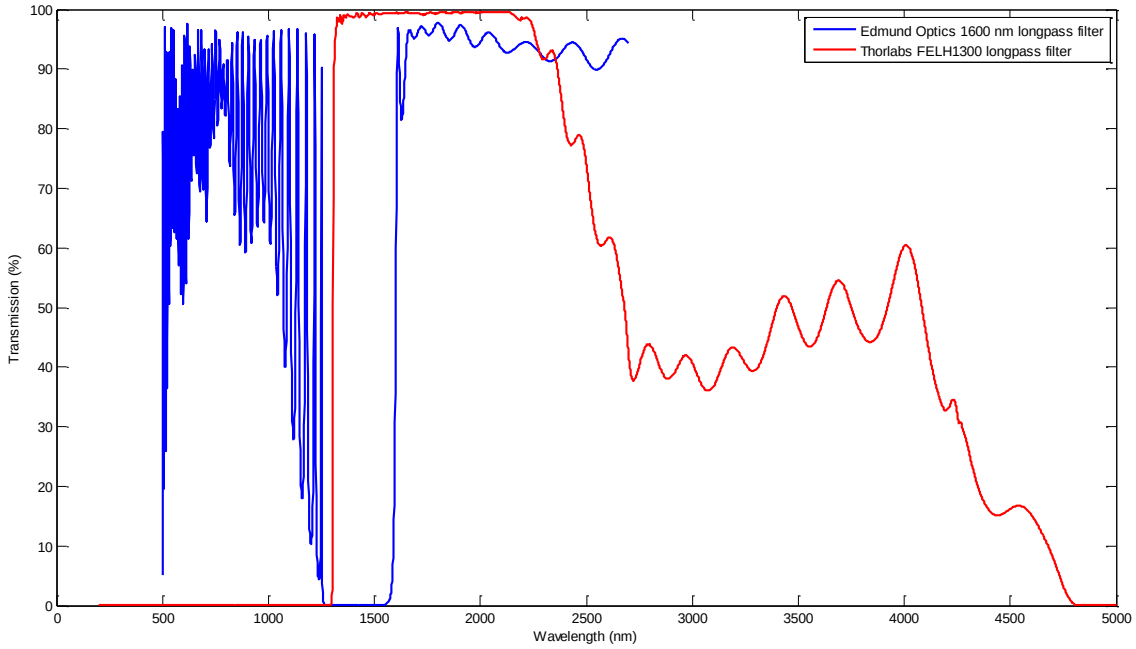

Figure 3-20 Filter transmission

In order to solve for the coherent light transmission, the maximum filter separation, L, must be solved for. The square root term is the deciding factor for the transmission – L must be solved for without both real and imaginary numbers. The value of L cannot be any larger than 400 nm for an only real term, anything larger produces both real and imaginary terms which would result in possible non-transmission. Using 400 nm as a filter distance, the combined transmission is seen in Figure 3-21.

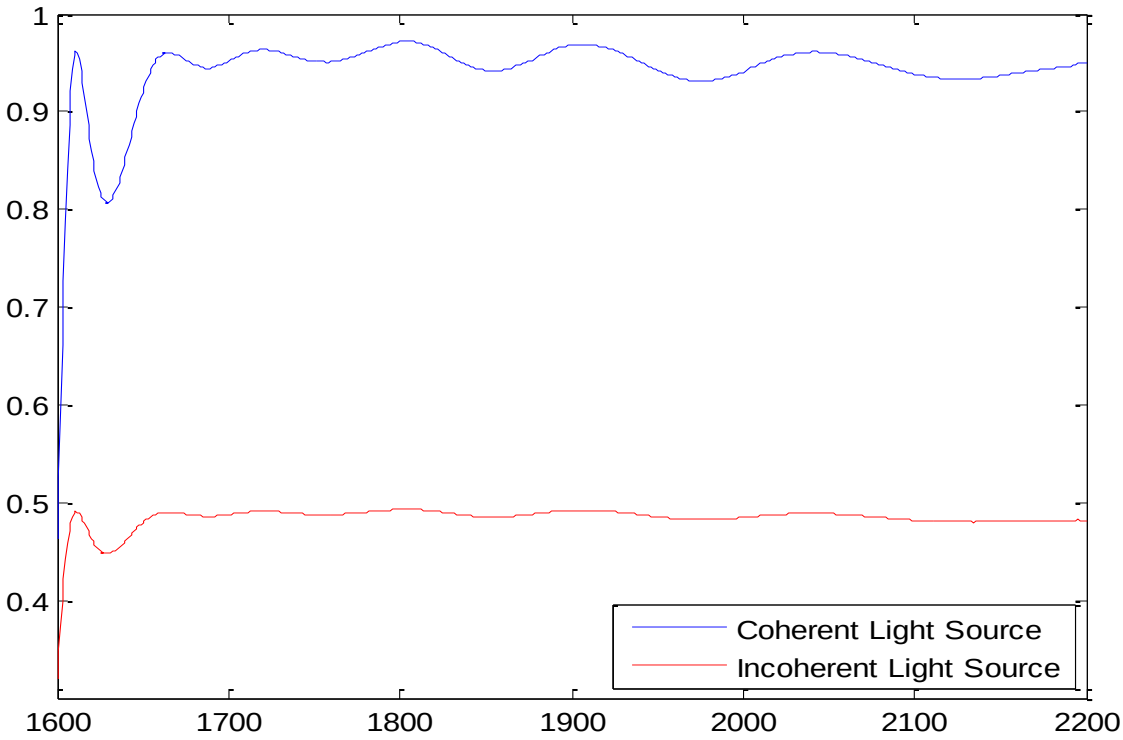

Figure 3-21 Combined filter transmission

These results suggest that the use of two filters in the instrument design is flawed and unnecessary, therefor only one filter will be used. The filter chosen is the Thorlabs FELH1300 longpass filter allows for its ability to block radiation in the NIR and VIS spectral regions.

3.3.5 Chassis Redesign

The chassis required enlargement in order for the new electronics deck and internal optical components. This gave space for more stable mounts to be placed internally. The optical deck which shields the optical components was changed in order to contain the

new pathways the light-waves travel. Additional mounting holes were also added in the optical deck in order for either the redesigned electronics deck. The CAD models for both the Argus 1000 and Argus 2000 instrumentation are shown. Figure 3-22 shows a typical optical deck mounted over the regions where light sensitive equipment is mounted, while in Figure 3-23 the grating and detector mounting equipment can be seen. The location to each mount is specifically determined for the spectrometer's end use (desired spectral range) and will vary with instrument to instrument.

Two materials were chosen to design the chassis out of; Al-6061 and Delrin 150SA. Chassis material is very important when designing a spectrometer. This is the material responsible for ensuring that the internal electrical and optical components are stable and unmoving during the spectrometer use. If there is internal movement, then the spectrometer will not function as planned and the spectral data retrieved may be useless.

For the Argus 2000 model, the use of Delrin was studied. Delrin is a homopolymer acetal which shows a good balance of internal properties meant to bridge the gap between plastics and metals. Delrin is typically manufactured by DuPont [62]. Many types of Delrin are available for purchase which comes in a variety of processing methods and product characteristics. All DuPont manufactured Delrin products show good dimensional stability, have good wear and abrasion properties, are chemically resistant to hydrocarbons, solvents and neutral chemicals, resulting in a product which can be used for many industrial applications.

For this project, the types of Delrin available needed to be determined. Delrin can be processed using both extrusion methods and injection molding. Only Delrin grades that were processed using extrusion methods were considered, as they are more densely packed and found to exhibit maximum toughness versus the injection molded Delrin. Only three types of Delrin are manufactured using extrusion methods. They are seen in Table 3-5.

Table 3-5 Composition of Delrin Acetal Resins [62]

Delrin Grade	Process Characteristics	Product Characteristics	Applications
150SA	High viscosity resin with low die deposit	Maximum toughness in an extrusion resin without modification.	Highly stressed sheet, rod and tubing.
150E	High viscosity resin with low die deposit	Toughness with reduced center-line porosity.	Exclusively stock shapes that is greater than .25 inches thick.
550SA	General purpose extrusion resin with additive system that allows fast cycling without voids or warpage	Excellent balanced properties in resin producing uniform rod stock.	Stock shapes for machining part, including rod, sheet, and tube.

From the properties compared in Table 3-5, Delrin 150SA is the type of Delrin grade chosen to build the Argus 2000 chassis. The material currently used for the Argus 1000 spectrometer is AL6061. The shortened table of material characteristics is seen in Table 3-6.

Table 3-6 Al 6061 and Delrin 150SA Material Properties (adapted from [62] and [63])

Properties		Al-6061	Delrin 150SA
Physical	Density (g/cc)	2.7	1.41
Mechanical	Ultimate Tensile Strength (MPa)	310	101
	Shear Strength (MPa)	207	66
	Poisson Ratio	.33	.35
	Modulus of Elasticity (Young's Modulus) (GPa)	69	3.103
Thermal	Thermal Conductivity (W/mK)	167	.4

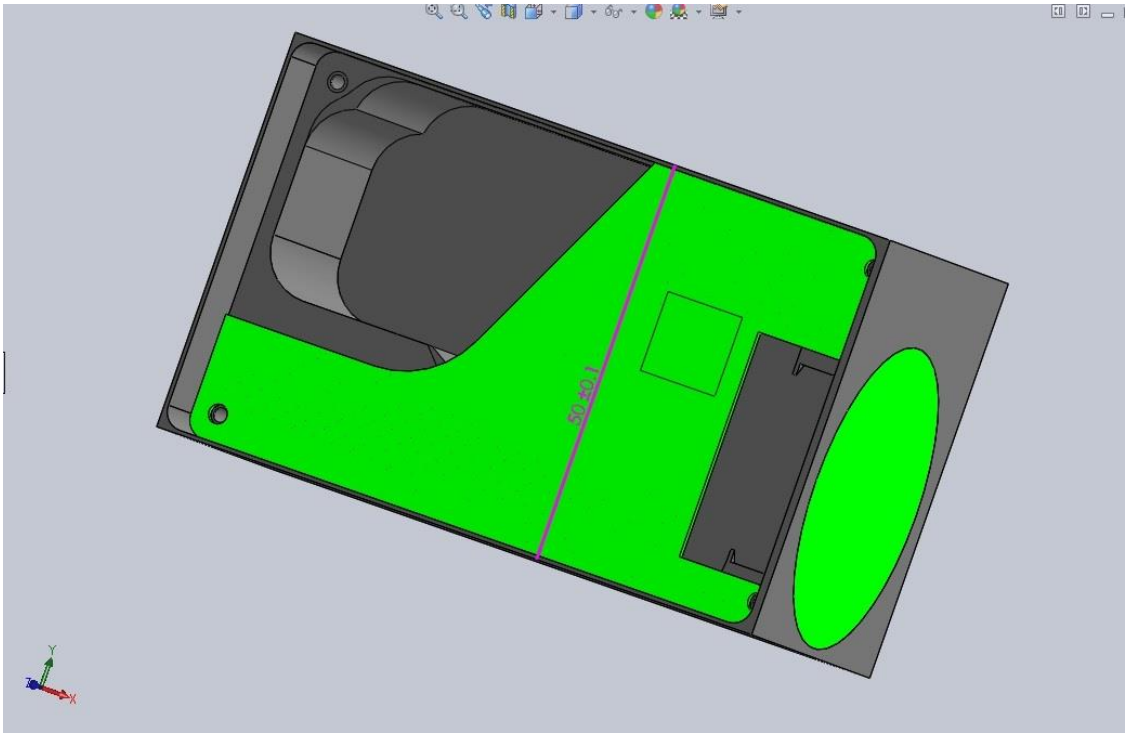

Figure 3-22 Argus 1000 CAD model

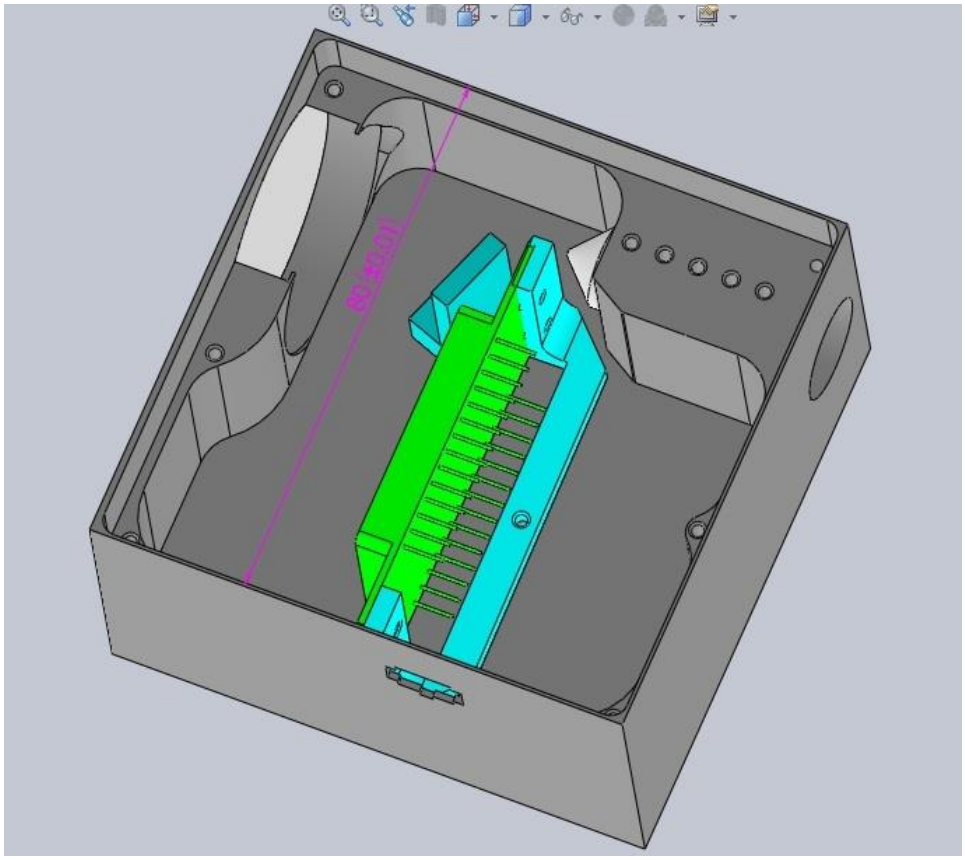

Figure 3-23 Argus 2000 CAD Model

In order to accommodate for the new desired spectral range, the Argus 2000 instrument chassis was enlarged from 40 mm x 50 mm x 80 mm [7] to 80 mm x 50 mm x 80 mm. The final assembled Argus 2000 chassis can be seen in Figure 3-24. The final weights for the assembled chassis' are 206.48 g for the Al-6061 chassis assembly and 116.37 g for the Delrin 150SA version. A comparison of the similarities and differences in Argus 1000 and Argus 2000 are in Table 3-7.

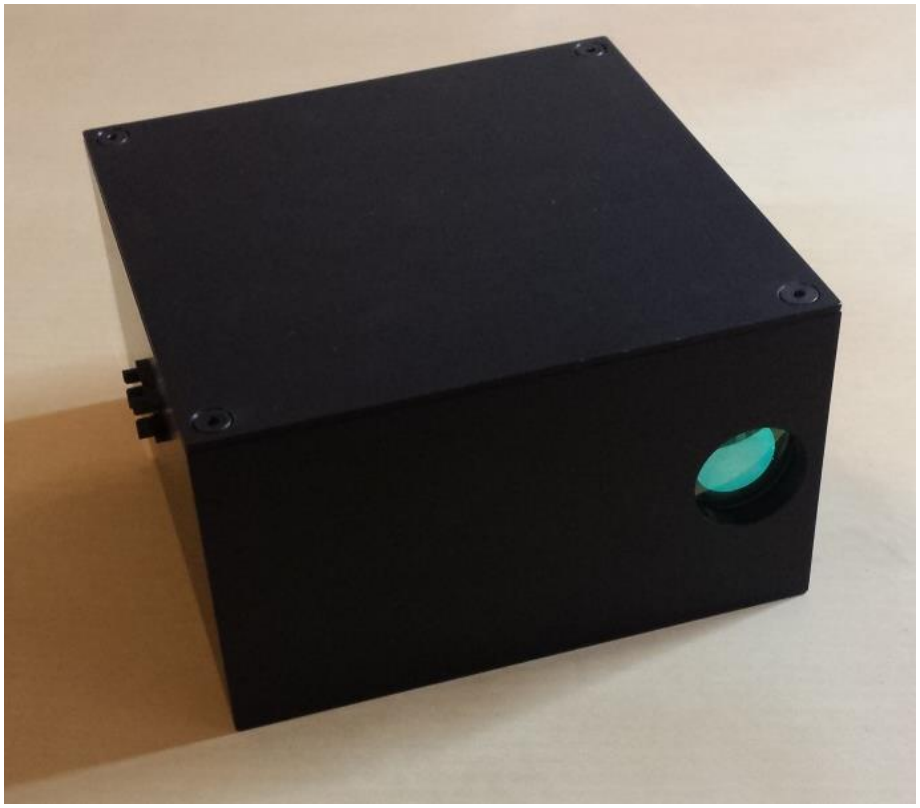

Figure 3-24 Assembled Argus 2000 micro-spectrometer chassis

Table 3-7 Argus version comparatives

	Argus 1000	**Argus 2000**
Mass	228g (Al-6061)	230g (Delrin), 320g (Al-6061)
Size	40 mm x 50 mm x 80 mm	80 mm x 50 mm x 80 mm
Power Consumption	2.4 W (max)	2.4 W (max)
Grating	300 groves/mm	600 grooves/mm
Integration Time	500µS to 4.096 S	500µS to 4.096 S
Detection Region	1100 – 1700 nm	1700 - 2200 nm

4 Unmanned Aerial Vehicle Design for Fieldwork

Sub-orbital platforms (unmanned aerial vehicles, sounding rockets and high altitude balloons) are often used as part of the validation methods for space mission. These platforms are reasonable in price and are able to be launched often. They are able to provide a basis in how the instrument being tested will perform in a remotely operated/accessed use. In this chapter, the UAV is used as a validation method of Argus technologies. The platform developed and tested are an integral component of the Argus technologies validation for field work and remote data collection.

An Unmanned Aerial Vehicle (UAV) was designed to perform field work in order to collect spectral data easily using the test instrumentation. No UAV system was available off the shelf that had the desired lift capacity and ability to safeguard the instrument in case of a rough or malfunction landing. Due to this, a UAV system was designed and developed using varying COTS products that are not normally incorporated together. This chapter describes the materials development and the campaign methods that are used when this UAV performs field work. This work resulted from research objective 4, prepare and test an Unmanned Aerial Vehicle (UAV) that is capable of performing spectral data acquisition fieldwork.

4.1 UAV Materials

This section describes the materials used for the UAV platform and scientific payload.

4.1.1 UAV Platform

The UAV platform consists of the UAV hardware and the scientific payload. The UAV is comprised of low-cost, easily available commercial off-the-shelf (COTS) components. Its main purpose is to safely fly the scientific payload for a minimum of ten minutes' flight. The platform is controlled by the UAV pilot and has safety features programmed into it, such as a return to home function.

The main chassis for the UAV is the 3DR-Y6 frame set. This features a diagonal wheelbase of 550 mm which is used to mount the UAV and payload hardware and three arms of 216 mm length each. The system is comprised of battery powered vertical take-off and landing (VTOL) UAV with 6 motors. The Y6 frame format was chosen to provide motor redundancy in case of failure during flight. The 880Kv motors and 30A electronic speed controllers (ESC) were chosen to be able to deliver a strong lift and ability for the UAV to carry the payload without fail during the flight. The arms are constructed from PA66+30GF material which is known to be resistant to breakage in case of crashing, while the diagonal wheelbase is base is constructed from PCB material.

The landing gear used is the AeroXcraft DJI F550 Landing Gear Set. This is a high crash resistant landing gear made from G10 and aluminum construction [64]. G10 laminate grades are produced by inserting continuous glass woven fabric impregnated with an epoxy resin binder while forming the sheet under high pressure. This material is used exhibits excellent mechanical and dimensional stability [65]. The landing gear offers 0.12 m of space to mount equipment and has large aluminum rails for landing. This landing gear was chosen over the original for its rigidity in case of a rough landing.

The UAV is powered by a Kypom KYPOM 5100mah 4S 35~70C Lipo Pack. This provides the system with approximately ten minutes of flight without the Argus and Argus DAQ, and three minutes with those systems included, of flight from full charge; dependent on the weather and wind conditions. The UAV is flown using a DJI NAZA V2 APM which is comprised of the GPS, MC, PMU, and LED system information monitor. The data from the APM is logged for further analysis at a later date. A first-person-view system in installed on the UAV so that the co-pilot can ensure the UAV is over the intended spectral target. This is extremely useful when flying over coastlines to ensure the target area has been observed. The UAV is controlled through its attitude sensors. The operator's desired controls are processed through the on-board computer and then confirmed through the accompanying sensors. When the UAV is placed into attitude hold, the science platform is held in nadir-viewing position.

Figure 4-1 UAV during test flight

4.1.2 Science Payload

The UAV science payload consists of an Argus micro-spectrometer and its associated data acquisition system (DAQ) and power system. The Argus micro-spectrometer measures 45 mm x 50 mm x 80 mm and has a variable integration time from 500 µs to 4.096 seconds. It features a narrow field of view of 0.15°. The data delivered by the instrument is of fixed length parity striped packets of spectra which include sequence number, temperature, array temperature and operating parameters [48].

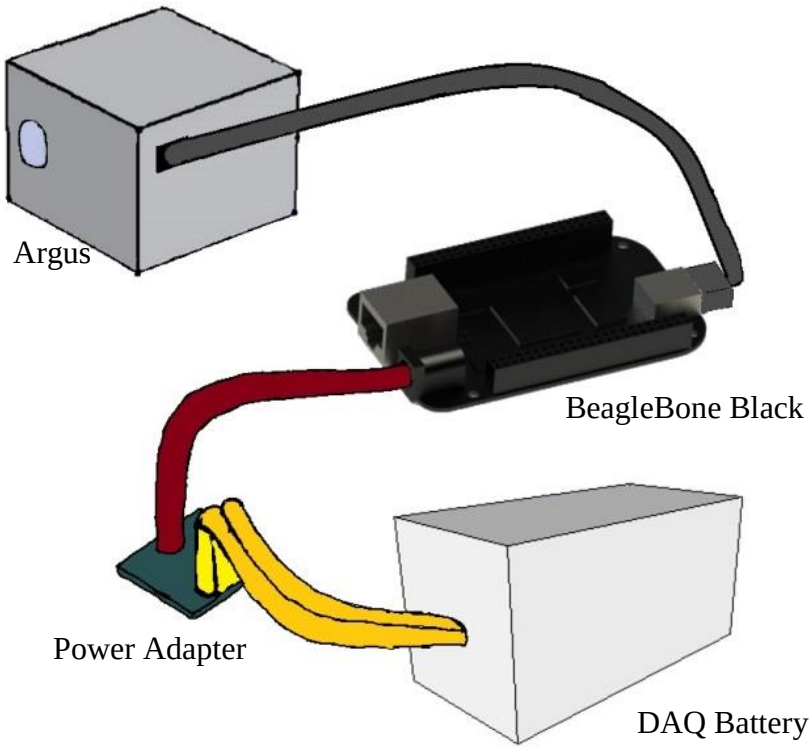

Figure 4-2 Scientific Payload

The Argus is mounted in a nadir viewing position in order to mimic spectral data taken from CanX-2. A GoPro camera is placed next to the instrument, also in the nadir facing position in order to ensure its imagery pixels overlap the Argus' field of view. The Argus is controlled and its outputs data logged by a BeagleBone Black. The BeagleBone Black was chosen for its simplicity, light mass, and ease to program and control remotely using an XBee radio module. The data is saved to a micro-SD card in the BeagleBone Black. This arrangement is shown in Figure 4-2. The Argus and DAQ are powered by a Ravpower 15000 mAh portable cell phone charger which outputs 5 V at 2.4 A and can

last approximately four hours on a full charge. The full mass of the UAV comes to 2625 g and the detailed mass of each component can be seen in Table 4-1.

Table 4-1 UAV mass breakdown

Item	Mass (g)
Y6 frame incl. motors, ESCs and propellers	478
F550 Landing Gear	270
BeagleBone Black and power cable	60
GoPro Hero 3+ with Protective Case	300
RAV Power 15000mAh External Battery	330
Kypom 4S 5100mAh Battery	480
Argus Spectrometer	230
Argus Cable	20
DJI NAZA V2 System	95
FPV TX/RX and Cloverleaf Antenna	88
Flytrek Core Flight Logger	4
Misc. Items	270
Total	2625

The bottom view of the UAV is showcased in Figure 4-3. The placement of the GoPro and Argus spectrometer can be viewed, while detailed distance separation between these two components can be seen in Figure 4-4. This information is used in order to compute the pixel overlap of the Argus and GoPro field of view.

Figure 4-3 UAV bottom view

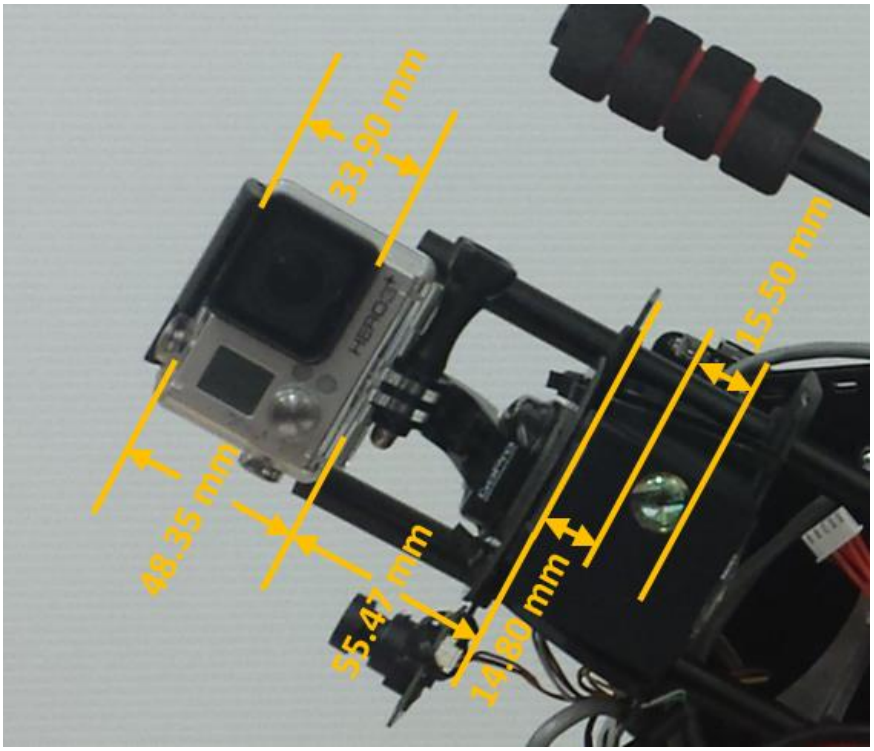

Figure 4-4 Detailed distance separation information

4.2 Software Development

Two pieces of software were developed for the UAV field campaign. The first is the data acquisition software which is run through the BeagleBone Black. This software is used to collect the data from the Argus instrument. The second software development provided a means to overlay where the Argus pixels would be in the GoPro imagery. This allows for visual confirmation of the surface Argus is taking spectral imagery of.

4.2.1 Data Acquisition Software

The data acquisition software, written in Python, was run on the BeagleBone Black. This software was responsible for the data acquisition of the Argus instrument.

The software architecture is seen in Figure 4-5. The user can specify whether the XBee radio transmitters are used for live data streaming to the ground station. This function was primarily used during flight testing to ensure that the data capture was occurring and that no radio communication issues were occurring. Alternatively, the XBee module did not have to be used, allowing for the data to just be recorded to the SDHC card aboard the BeagleBone Black.

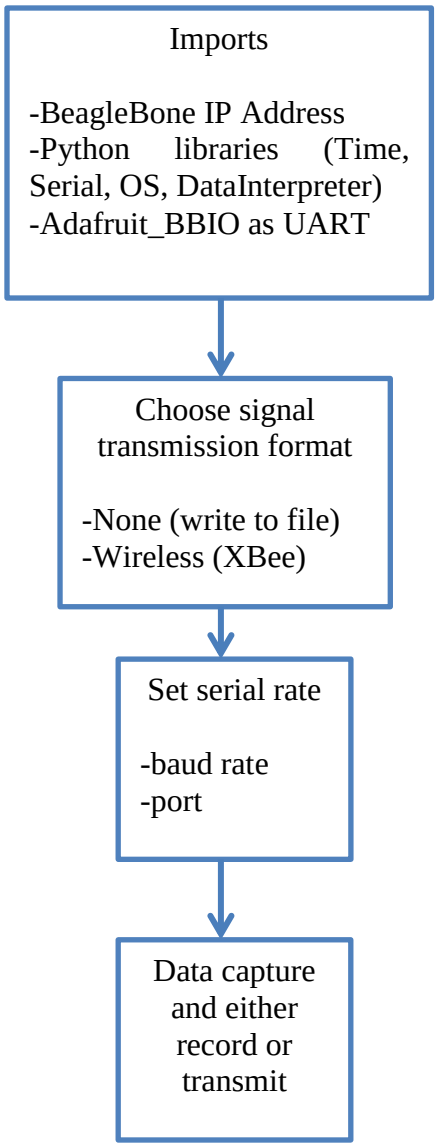

Figure 4-5 Argus DAQ software architecture

It was noted that when the code tried to have both functions operational at the same time, the BeagleBone Black would crash. Due to that the user had to specify which form of

transmission was desired. The data captured was saved to a binary file for later retrieval and data analysis.

4.2.2 Overlay between Argus Spectra and GoPro Imagery

Using the physical measurements seen in Figure 4-4 it is possible to determine which pixels on the GoPro imagery represents the region in which spectral information was captured. The software architecture is shown in Figure 4-6.

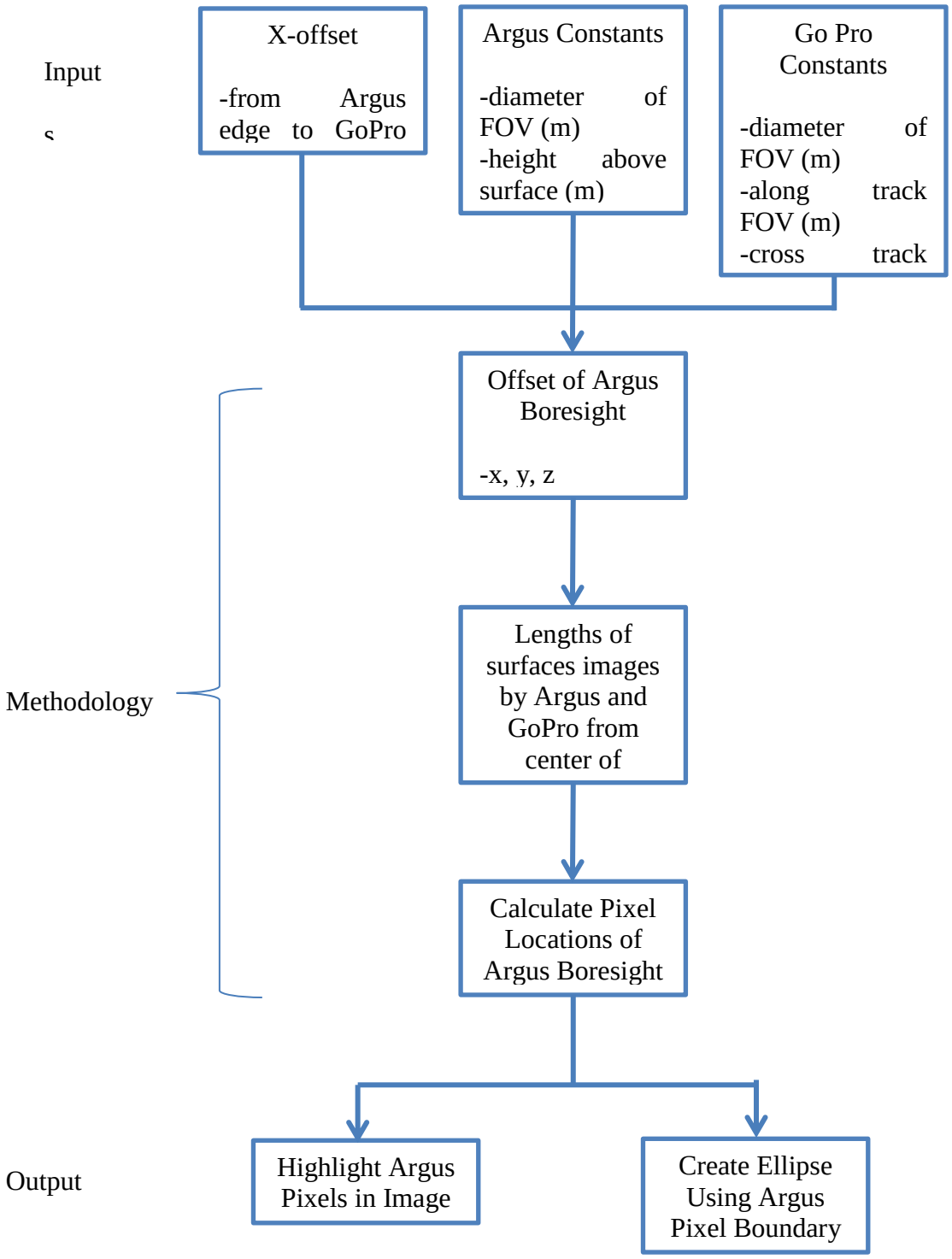

Figure 4-6 Argus Overlay

From the Argus and GoPro measurements, first the offset of the Argus boresight is computed. This allows the physical relation of where the Argus is taking measurements in the x, y and z dimensions. Next the lengths of the surfaces measured in meters are computed for both the Argus and GoPro images. Using the Argus boresight offsets, the pixels which Argus essentially views are marked on the GoPro image. An ellipse is drawn around these pixels using the pixel boundary locations.

This information is used to confirm the surfaces for which there is spectral imagery.

4.3 Field Campaigns

Two field campaigns occurred from mid-November 2014 to April 2015 in order to validate the UAV data acquisition system and stability of the craft's operation. The field campaigns were performed on days with clear visibility, low winds, and no precipitation. The rules set out in the Canadian Aviation Regulations were adhered to and flight information (contact information, UAV model, description and geographical boundaries of operation) were sent into Transport Canada before each flight. The flights were performed in remote locations across coastline sources and across various surfaces, with the UAV manually operated and without loss of sight with the pilot.

Figure 4-7 UAV and controller pre-field testing

For first field campaign, the main spectral targets were shallow water systems with clear coastline boundaries and bare (uncovered and untreated) patches of soil just outside of Toronto, Ontario. There was minimal wind and no snow or sleet precipitation occurred. The sky was partially overcast. An Argus 1000 was used and set with a 1.024 second integration time and high spectral sensitivity setting and while the nadir facing GoPro was programmed to continuously take imagery every 0.5 seconds. The UAV was flown at an altitude of approximately 10 m over the spectral targets.

For the second field campaign, the main spectral targets were deep water systems with clear coastline boundaries and a variety of different surface targets, including bare patches of soil, automobiles, and aged asphalt. It occurred during excellent weather conditions; no wind, and bright sun. The UAV was flown at an altitude of 20 m. An Argus 1000 instrument was used, set with a 0.256 second integration time and low spectral sensitivity, while the GoPro still recorded imagery at every 0.5 seconds. It flew approximately over the spectral targets at an altitude between 20 and 50 meters.

342 spectral samples were obtained over the two campaigns and seven surface types were observed.

Research objective 4 concluded with a series of field flights with the UAV. The system proved capable of performing spectral data acquisition fieldwork at low altitudes. While this is not meant to be a substitute for space-based measurements, the UAV system can provide a testing platform any Argus series spectrometers.

5 Laboratory Methodology

This chapter describes the methodologies performed for the various laboratory experiments.

5.1 Soil Baking

This section speaks to the methodology behind measuring the sample soil's moisture content in the laboratory. This methodology will be used to confirm the soil moisture content of the sample when obtaining its corresponding spectra. The overall methodology's error was found and is discussed in Soil Baking Error Analysis.

5.1.1 Methodology

The purpose of performing the soil bake is to ensure that the required soil moisture content (SMC) is obtainable and within a certain tolerance related to the measuring and baking error.

First the soil under test (SUT) has all its moisture removed. This is done through a baking process using a Tenney Junior Compact Temperature Cycling Environmental Chamber. This oven features a fiberglass and polyurethane insulation that surrounds the temperature chamber, ensuring minimal thermal loss [66]. It is also programmable and has a temperature range from 0°C to 300°C [66]. Following the *American Society for Testing and Materials* (ASTM) 2216-98, process to bake off soil moisture, 1 kg of the SUT is placed in a baking dish and baked at 105°C for 12 hours [67] . This soil can now be used for moisture content testing purposes.

Figure 5-1 Denver Instruments Digital Scale

Now the moisture content of the soil can be produced. At this point, it is possible to produce any value of soil moisture content desired. In order to complete this laboratory segment, the bake oven and digital scale are used. The digital scale used in the laboratory experiments is a Denver Instruments SI-203. It has a mass range of 0 to 200 g and an error value of 0.001 g [68]. The petrie dishes used for soil baking are weighed ahead of the procedure (m_1) and must be dry and clean prior to use.

Approximately one-third of the petrie dish is filled and the mass is recorded. Each petrie dish now has distilled water added to it, using soil to water ratios from 10% to 80% (m_2). The distilled water to be added is measured with a graduated cylinder. The soil to water

ratio is the theoretical soil moisture contents desired. The samples are well mixed and then baked for 12 hours at 105°C in order to remove all of the distilled water which was added to them.

Figure 5-2 Soil samples ready for weighing

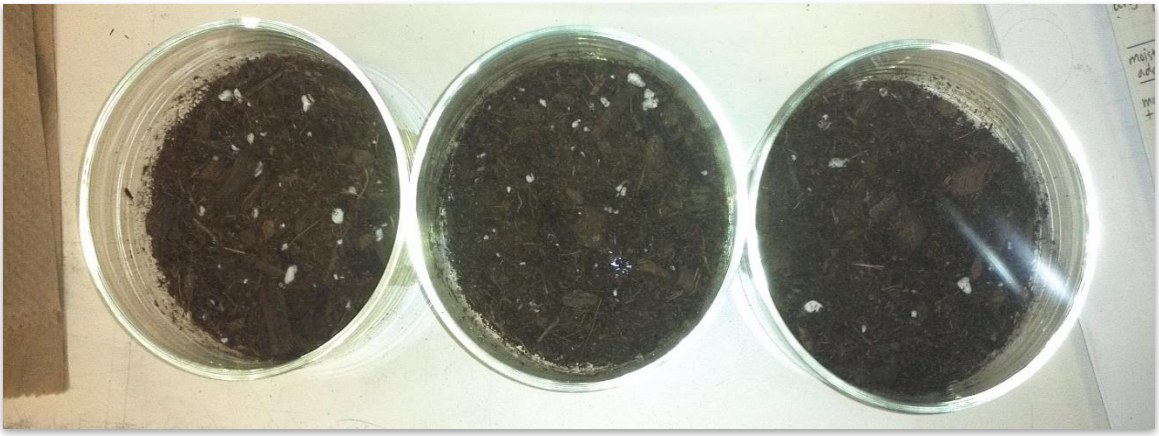

Figure 5-3 Three soil samples after the addition of distilled water

After the baking process is complete, each container and dry soil is weighed (m_3). The soil moisture content of each sample is now calculated through Equation (5-1). The mass of moisture is represented by the numerator, while the denominator is the mass of dry soil.

$$SMC = \frac{(m_2 - m_3)}{(m_3 - m_1)} x100 \qquad \textbf{(5-1)}$$

The overall process is repeated three times to confirm the amount of water needed for the SMC ratio desired. The baking process is found to provide a simple and effective measurement of SMC.

5.1.2 Soil Baking Error Analysis

Various quantities m_1, m_2, m_3 are measured with small uncertainties δm_1, δm_2, δm_3. Measured values are used to calculate quantity SMC, then the uncertainties in m_1, m_2, m_3 cause in an uncertainty in SMC.

The measured values are m_1, m_2, m_3 are independent and random errors and therefor propagate according to the sum of quadrature [69].

$$\Delta SMC = \sqrt{\left(\frac{\partial SMC}{\partial m_1}\delta m_1\right)^2 + \left(\frac{\partial SMC}{\partial m_2}\delta m_2\right)^2 + \left(\frac{\partial SMC}{\partial m_3}\delta m_3\right)^2} \quad \textbf{(5-2)}$$

The partial differentials, denoted by the symbol ∂, are used in order for each component of the equation to have proper weight. Not all of the equation variables are of equal weight, as the m_3 measurement is used twice, whereas both m_1 and m_2 are only used once in the SMC calculation.

The partial differentials are solved used in the final uncertainty in SMC. The expanded SMC uncertainty is seen in (5-2). For an equation with only two independent random variables, the sum of Quadrature can be used. Measurements m_1 and m_3 are made up of only their associated values, while measurement m_2 is the summation of two values, the value of the dry soil and the distilled water, expressed as Equation (5-3) where m_c has associated error c_E, and s_m has associated error of m_E.

$$m_2 = m_c + m_E \ \therefore error = \ c_E + m_E \quad \textbf{(5-3)}$$

$$\delta m_2 = \sqrt{\left(\frac{\partial m_2}{\partial c_E}\delta c_E\right)^2 + \left(\frac{\partial m_2}{\partial m_E}\delta m_E\right)^2} \quad \textbf{(5-4)}$$

Each partial derivative is further broken down

$$\delta m_2 = \sqrt{\left(\frac{\partial(c_E + m_E)}{\partial c_E}\delta c_E\right)^2 + \left(\frac{\partial(c_E + m_E)}{\partial m_E}\delta m_E\right)^2} \quad \textbf{(5-5)}$$

The Sum/Difference Rule is applied and is seen in Equation

$$\frac{\partial(c_E + m_E)}{\partial c_E} = \frac{\partial c_E}{\partial c_E} + \frac{\partial m_E}{\partial c_E} = 1 + 0 = 1$$

$$\frac{\partial(c_E + m_E)}{\partial m_E} = \frac{\partial c_E}{\partial m_E} + \frac{\partial m_E}{\partial m_E} = 0 + 1 = 1 \quad \textbf{(5-6)}$$

The partial derivatives are both equitable to 1. The error in measurement m_2 is solved in Equation (5-8).

$$\frac{\partial m_2}{\partial c_E} = \frac{\partial m_2}{\partial m_E} = 1 \quad \textbf{(5-7)}$$

$$\delta m_2 = \sqrt{(\delta c_E)^2 + (\delta m_E)^2} = \delta c_E + \delta m_E \quad \textbf{(5-8)}$$

After the Δ*SMC* is found for each set, the RMS value is then found for all the test sets. This is solved using equation (5-9). The variable n is the number of sets and δSMC_{set_i} is the SMC error value found for each given laboratory test set.

$$\delta SMC_{RMS} = \sqrt{\frac{\sum_{i=1}^{n} \delta SMC_{set\_i}}{n}} \qquad \textbf{(5-9)}$$

5.2 Argus 2000 Calibration

This section descries the practices followed in order to perform the instrument calibration. The instrument calibration consisted of wavelength to pixel number determination, or wavelength calibration.

Previously calibration has been performed using laser beam. However, a laser that outputs within the desired spectral region of the Argus 2000 instrument was not able to be acquired and thus other methods were explored. These methods include pencil lamps and use of external filters and the actual detector cut-off edge.

5.2.1 Wavelength Calibration

The laboratory set-up is modeled after Walker [70] and Jagpal [42]. The experimental known parameters, assumptions, and laboratory set-up are described in the following sub-sections.

5.2.1.1 Known Parameters and Assumptions

The quartz-halogen lamp with tungsten filament made by Oriel (model QTH FEL 6315) produces a heat of 3200°K and a power equivalency of 1000W [71] is taken to be a point source. It is assumed that the collimated light source does not lose intensity (W/m^2) along the collimation path from the mirror to the spectralon as seen by Argus 2000. It is also assumed that the radiance does not change over the setup through collimation.

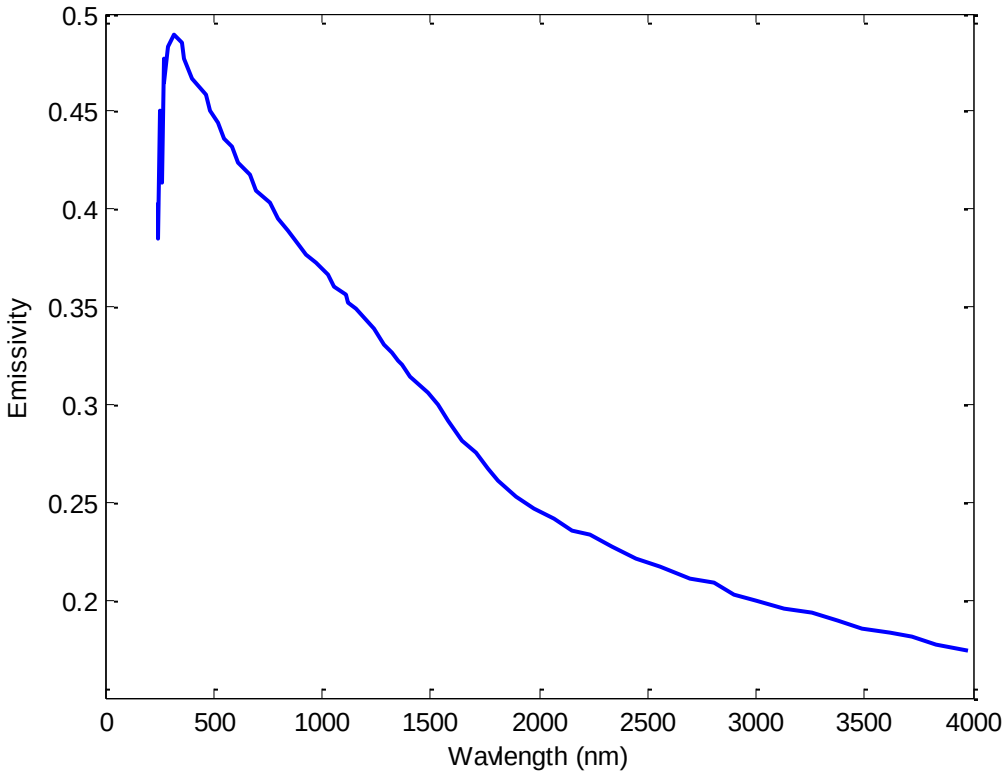

Figure 5-4 Spectral Emissivity for Tungsten with Constant Temperature of 3000°K (adapted from [72])

5.2.1.2 Lab Set-up

The spectrometer is mounted on an adjustable Vernier kinematics mount with five degrees of freedom. The spectralon used is Labsphere SRT-00-050 (Calibration Report Number AA-00821-000) with National Laboratory Traceable Standard SRS-99-050; the reflectivity data is viewable in Figure 5-6 Spectralon Reflectivity. The reflectivity stays above 0.92 for the desired wavelength range.

The light is collimated using an aluminum coated mirror. The collimation beam is directed so that it hits the spectralon without any angular dispersion. The circular aperture is needed to cut out stray light (Figure 5-5).

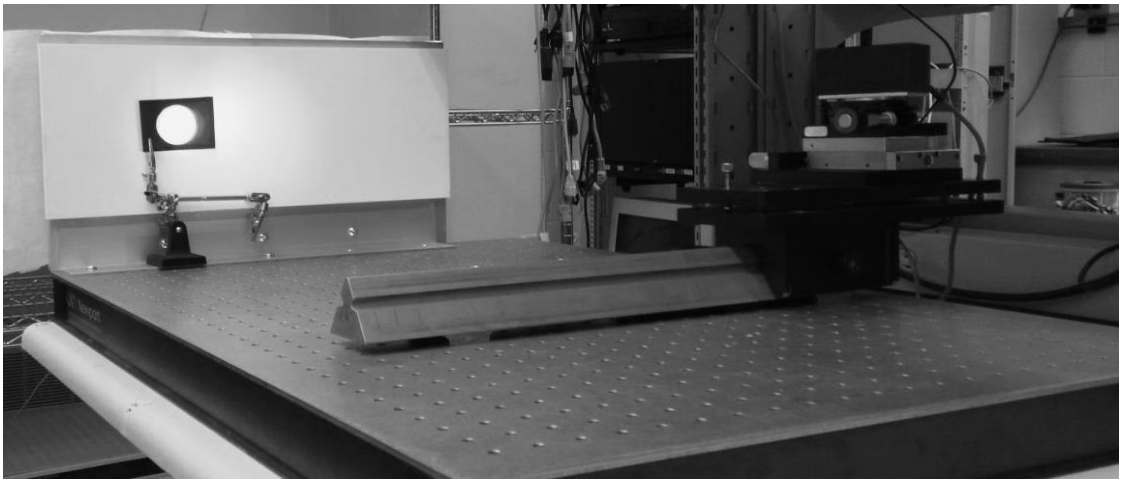

Figure 5-5 Circular aperture and collimated beam

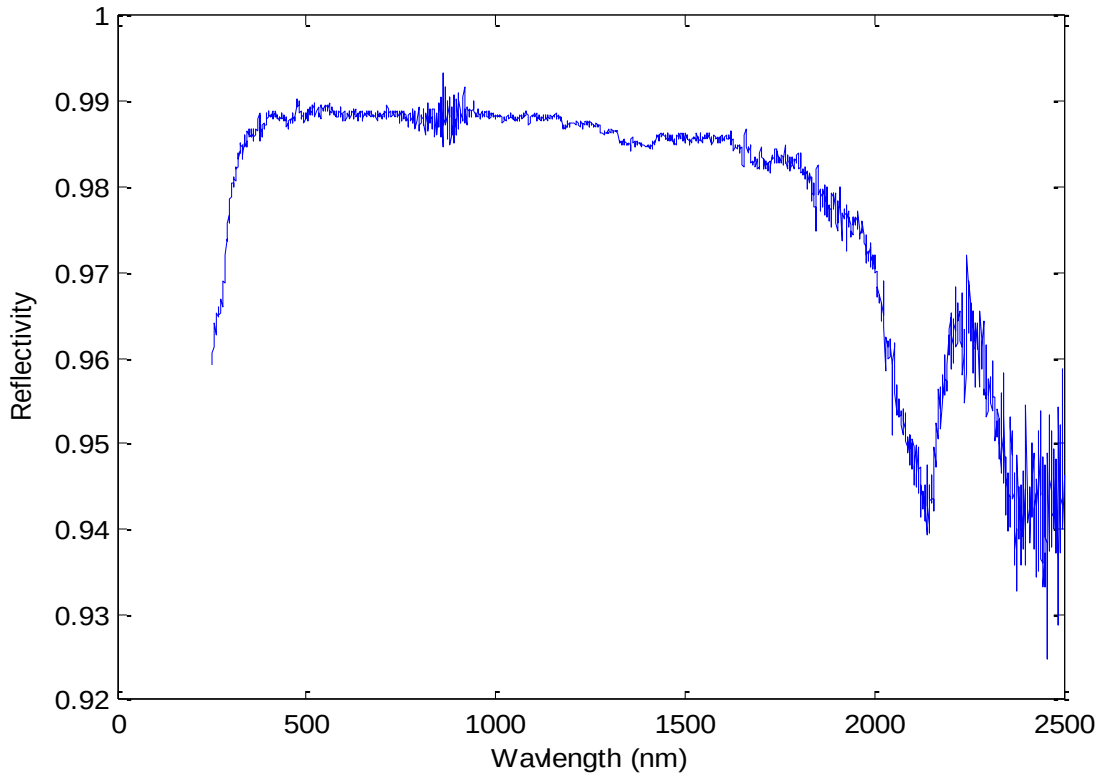

Figure 5-6 Spectralon Reflectivity

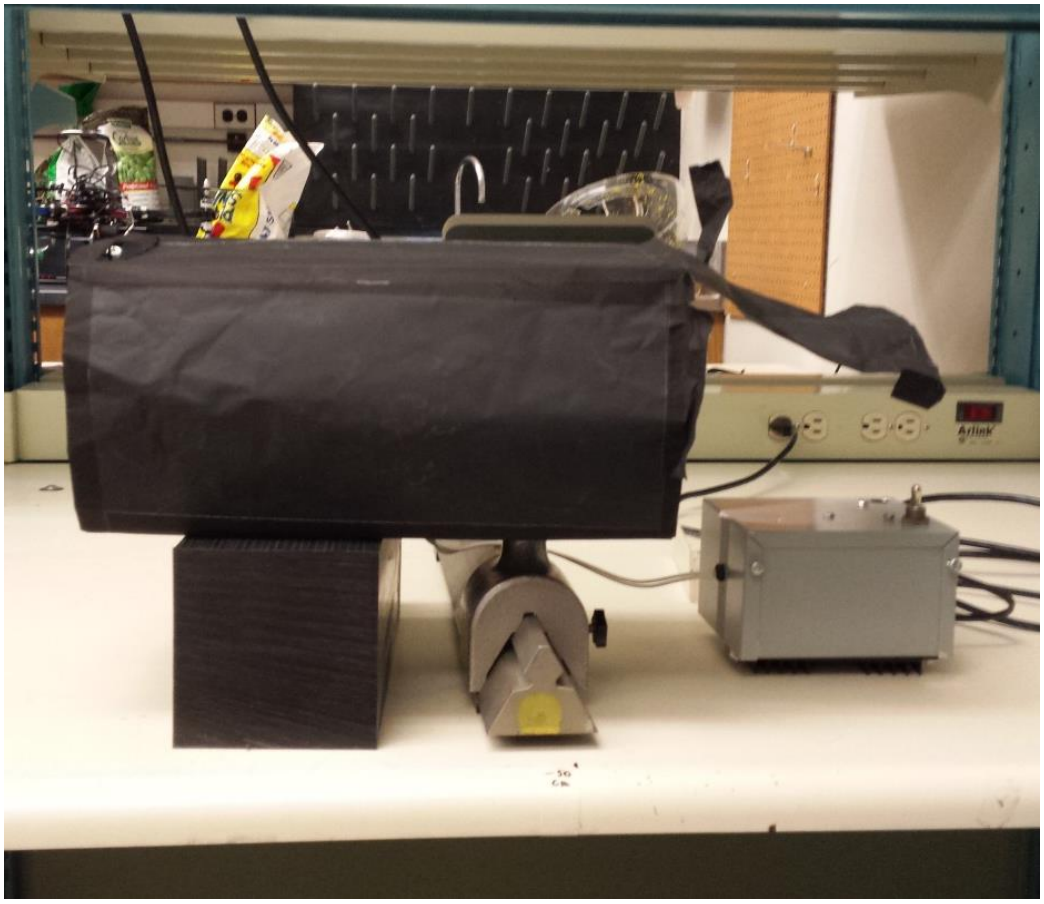

Figure 5-7 Enclosure in laboratory setup

5.2.1.3 Pencil Lamps

The laboratory setup consists of varying types of pencil style calibration lamps, which fills the instrument's instantaneous field of view (IFOV). This simulates radiation emitted by a ground tile and received by the spectrometer. The spectrometer is mounted on an adjustable Vernier kinematics mount with five degrees of freedom. The pencil lamps were used first as they contain sharp theoretical spectral intensity peaks at very specific wavelengths.

The tungsten-halogen light is set to give a power output of 500W and the grating is moved to ensure a clear view of detector cut-off edge. The background noise for each measurement is taken. Figure 5-8 Laboratory Set-up Pencil Lamps shows the laboratory experiment. The pencil lamp spectra will be taken with both the light source on and off. This is required because the pencil lamp intensity is unknown and so it can be determined if it could be measured by the Argus 2000 instrument. The background noise will also be measured by turning off the light source and pencil lamp power.

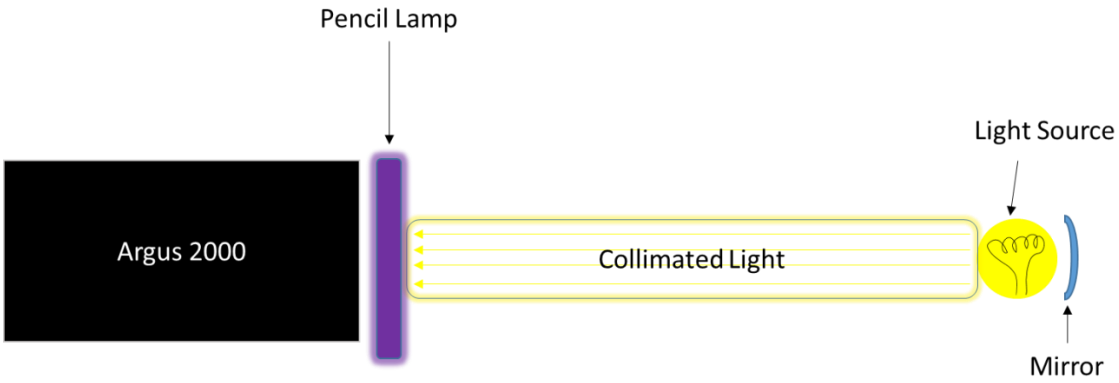

Figure 5-8 Laboratory Set-up Pencil Lamps

The pencil style calibration lamps available for use are 6033 Xenon (Figure 5-9), 6031 Krypton (Figure 5-10), and 6030 Argon (Figure 5-11).

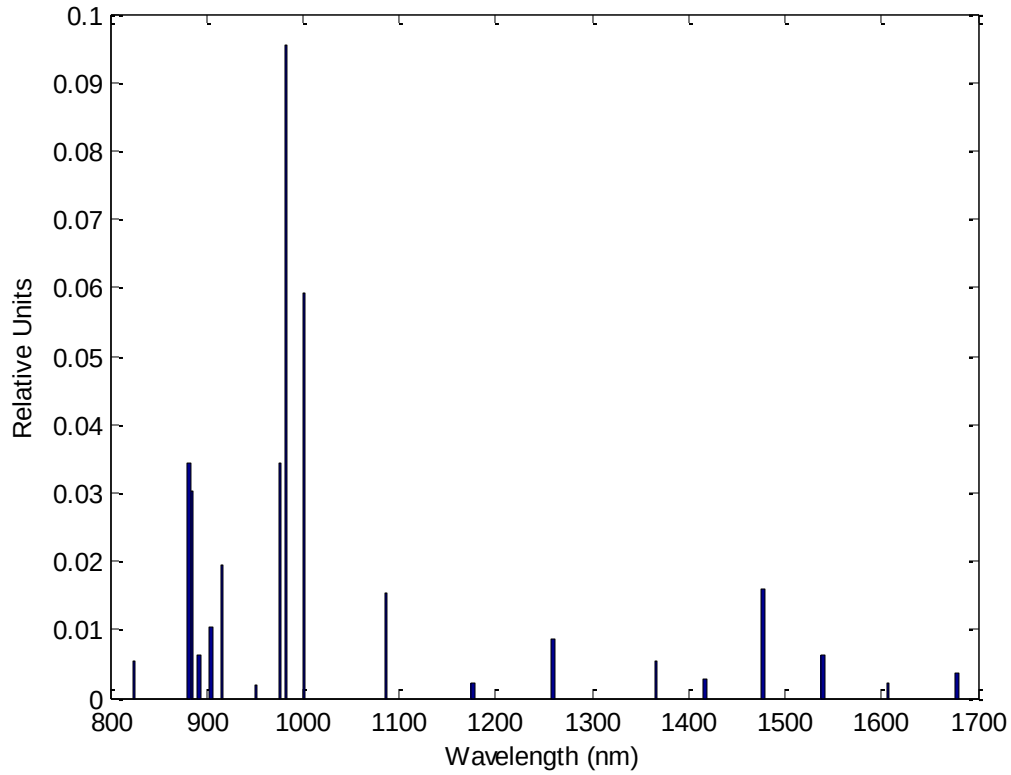

Figure 5-9 Xenon Pencil Lamp (adapted from [73])

The Xenon lamp produces emission lines in the visible to IR spectrum. The output caused by the excitation of the Xenon gas in this lamp contains no UV light. It also features an emission line close to 1700 nm [73].

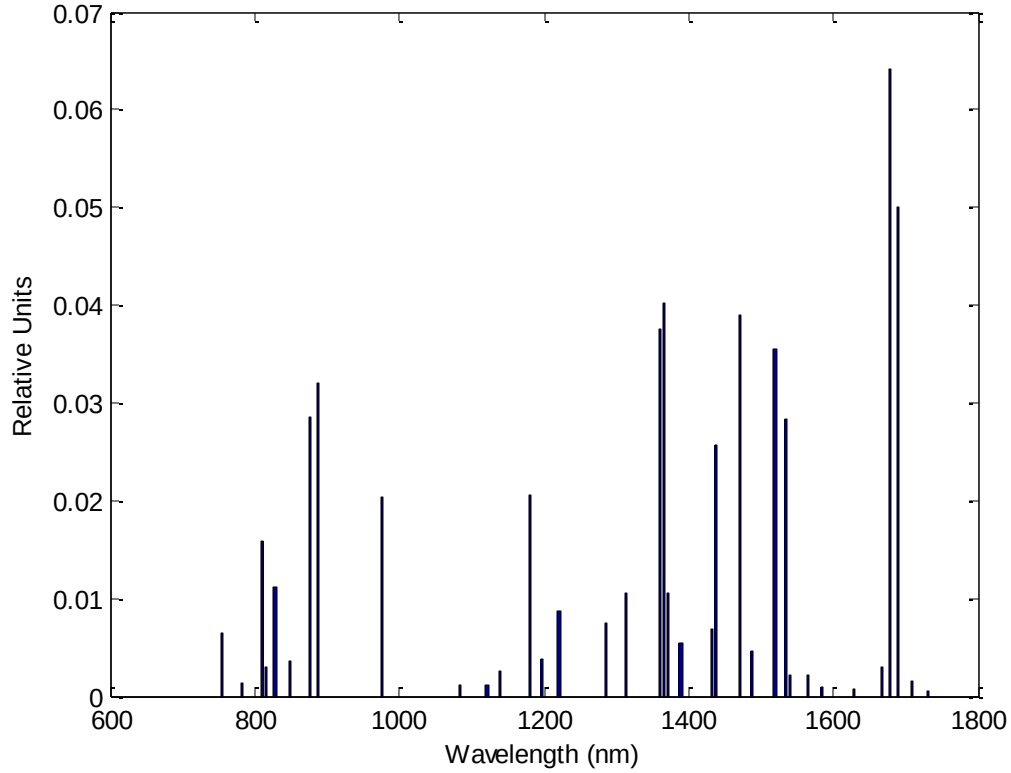

Figure 5-10 Krypton Pencil Lamp (adapted from [73])

The Krypton lamp produces spectral lines within the visible to IR region [73].

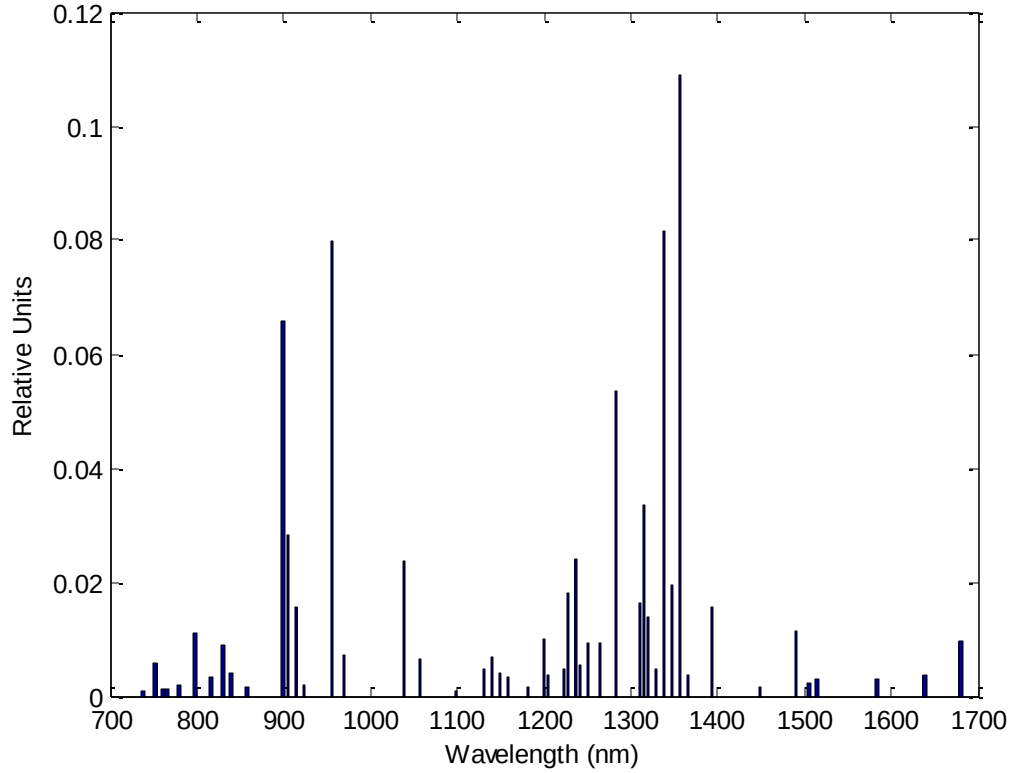

Figure 5-11 Argon Pencil Lamp (adapted from [73])

The Argon lamp produces primarily visible to IR emissions from excitation of pure Argon gas [73]. It also features an emission line close to 1700 nm.

The Krypton lamp is chosen to use for wavelength calibration.

5.2.1.4 Detector and Filter Edge

The wavelength – pixel correlation will also be performed using the detector edge and the 1600 nm filter placed in front of the Argus 2000. The detector edge will be viewable through the grating placement - the grating will have a sharp edge off in transmission

around 2100 nm. The laboratory experiment consists only of the collimated light beam facing the input optics of the Argus 2000 instrument and is seen in Figure 5-12.

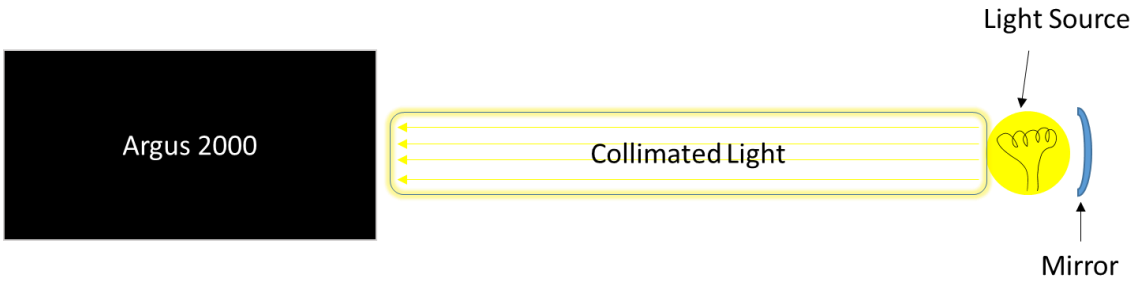

Figure 5-12 Detector Edge

The laboratory experiment for the filter edge is similar to that of the detector edge, except the 1600 nm filter is placed in front of the Argus 2000 input optics in order to create a sharp cut at 1600nm (Figure 5-13).

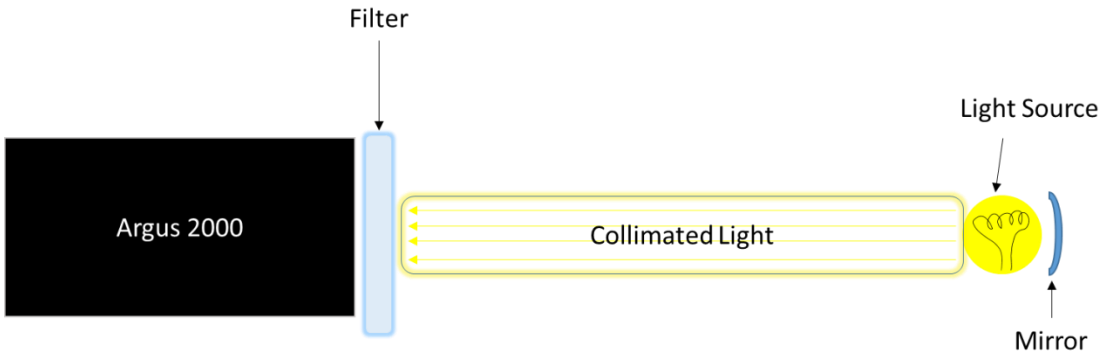

Figure 5-13 Filter Edge

The placement of the 1600 nm filter can be seen in Figure 5-14.

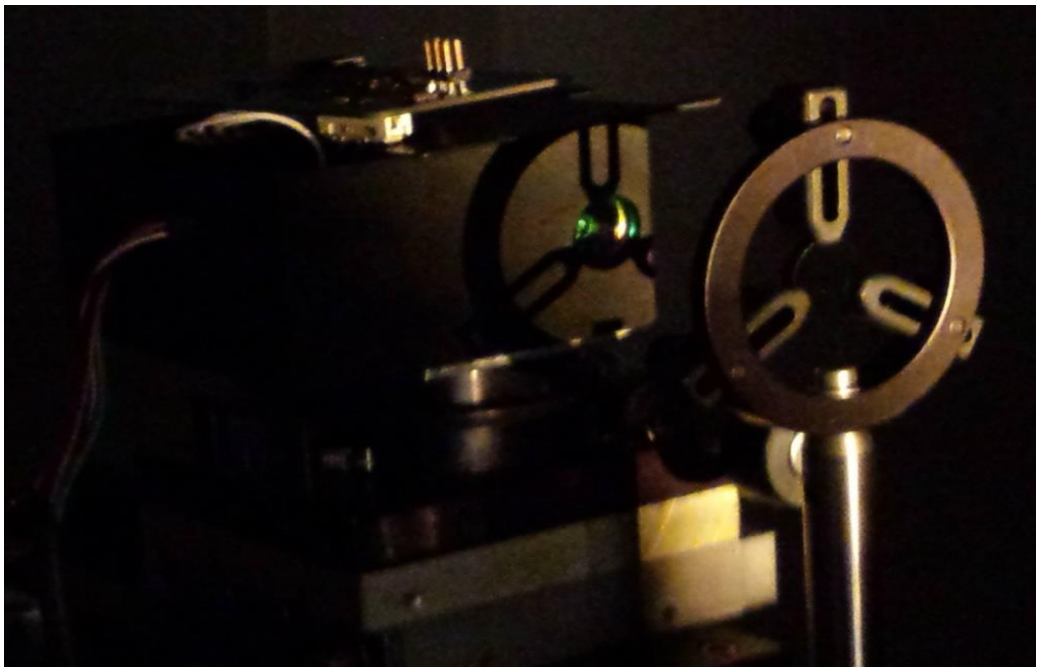

Figure 5-14 Filter Placement

The incidence points will be calculated for both the detector edge and filter measurements. Incidence points are where the function changes concavity. Since concave up corresponds to a positive second derivative and concave down corresponds to a negative second derivative, then when the function changes from concave up to concave down (or vise versa) the second derivative must equal zero at that point. These points are assumed to occur at the location in the theoretical and experimental data.

5.3 Soil Spectra Collection

The laboratory set-up is meant to resemble a spectral viewing from space. It uses the 1000W quartz-halogen with tungsten filament light source mentioned in 5.2.1.1 as well as keeping the same laboratory assumptions as previously mentioned. The Argus 2000 instrument and the soil under test are also utilized.

5.3.1 Lab Set-up

The laboratory experiment is defined by the size of the light source projection on the wall. The light source uses collimate the light from the 1000W quartz-halogen lamp with tungsten filament. The arrangement is modeled after the radiometric calibration laboratory setup, except with a petrie dish filled with soil instead of spectralon. The soil is placed at the same height as the Argus 2000 instrument so that The soils' spectra are measured by the Argus 2000 instrument. This is shown in Figure 5-15 Taking soil spectral measurements. Three datasets will be measured – 0%, 50% and 100% SMC.

5.3.2 Taking Spectral Measurements

The Argus 2000 instrument and the light source are turned on for fifteen minutes before measurements are taken. This is to ensure thermal noise reduction – it had been previously found that after approximately fifteen minutes the thermal noise from the light source and instrument detector to be reduced to minimum. Two identical samples of soil are to be prepared at a time. One soil sample will be tightly wrapped in the petrie dish using plastic wrap while the other will be used for taking spectral measurements. The measurements must be taken within a timely manner as not to allow the moisture within

the soil to begin evaporation. Once the spectral measurements are taken, the soil samples under wrap will be baked in order to confirm their SMC values.

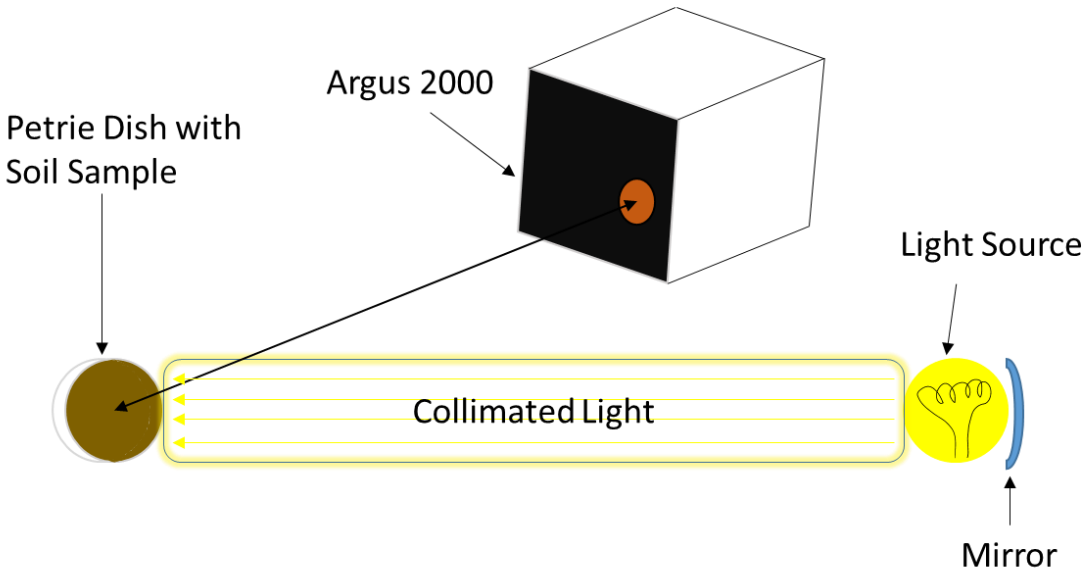

Figure 5-15 Taking soil spectral measurements

The soil spectra were taken on March 17th 2016. Table 5-1 shows the datasets measured using the Argus 2000 instrument. The actual laboratory set-up can be seen in Figure 5-16.

Table 5-1 Soil Data for Laboratory Soil Spectral Measurements

Measurement Container	Percent SMC	Type of Soil
F	0	All-purpose (Miracle-Gro)
G	50	All-purpose (Miracle-Gro)
L	100	All-purpose (Miracle-Gro)

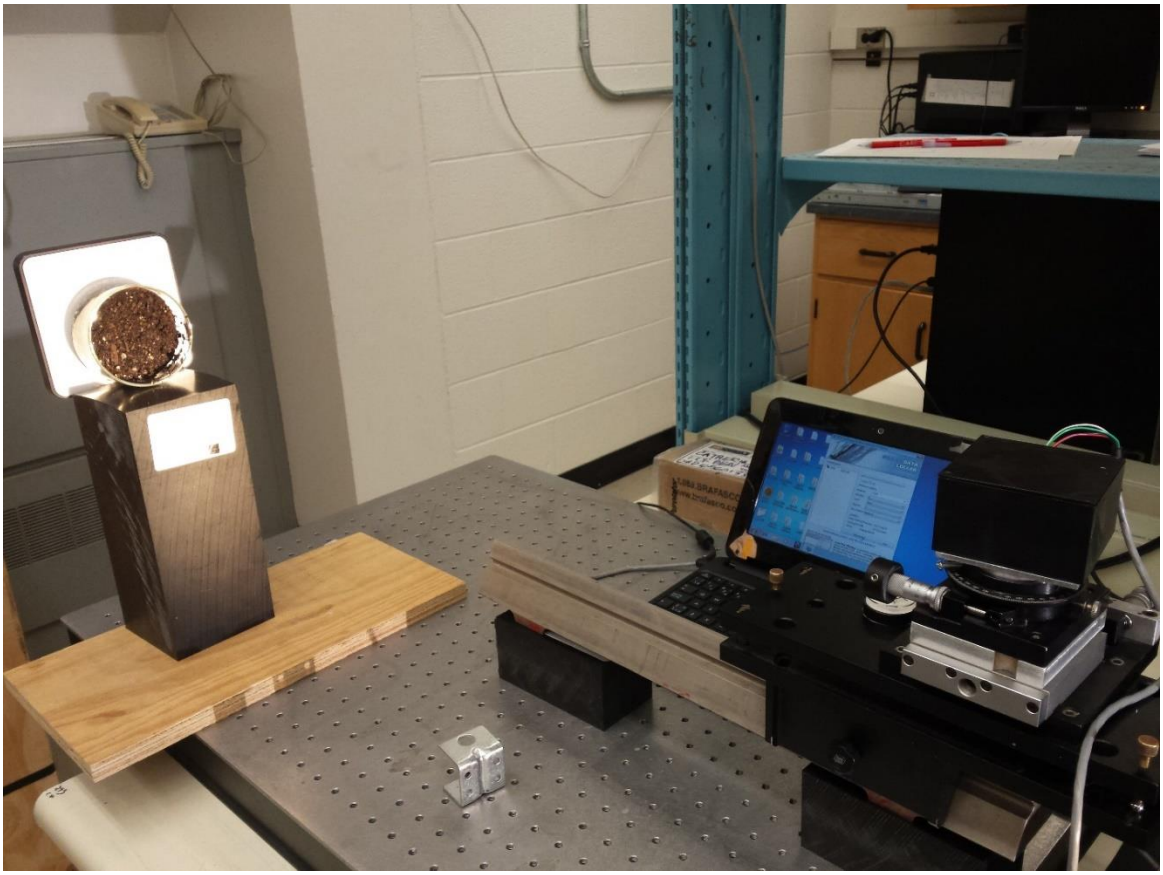

Figure 5-16 Laboratory Set-up

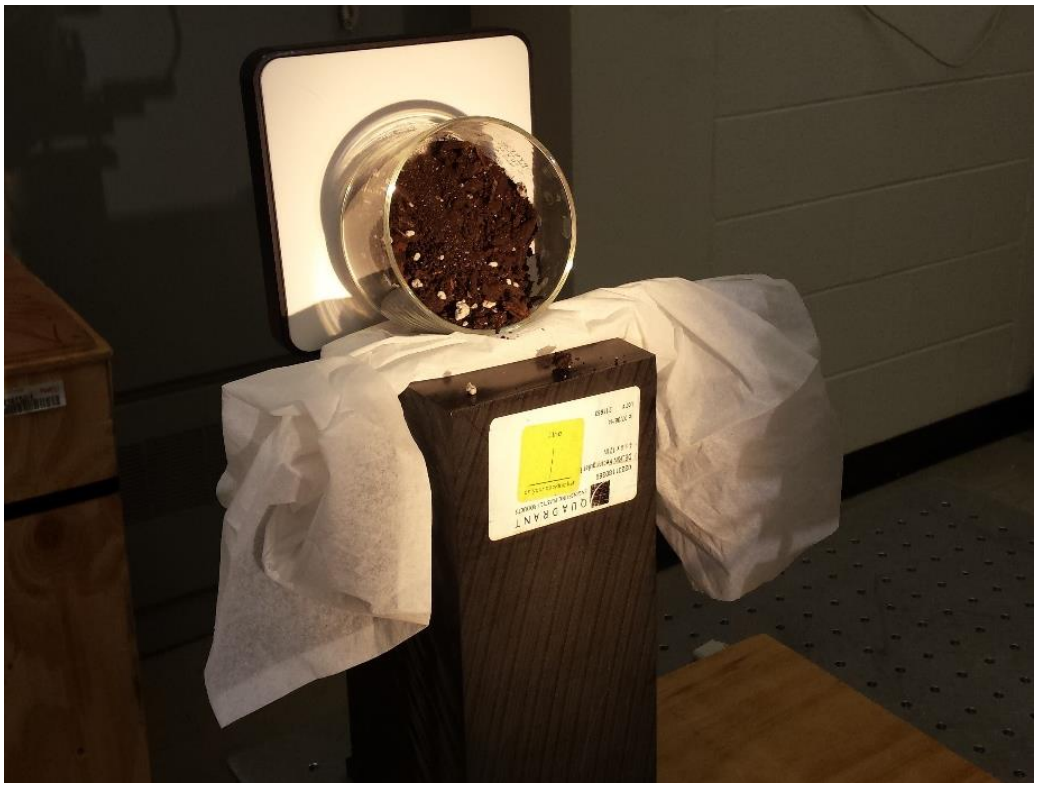

Figure 5-17 Soil Under Illumination

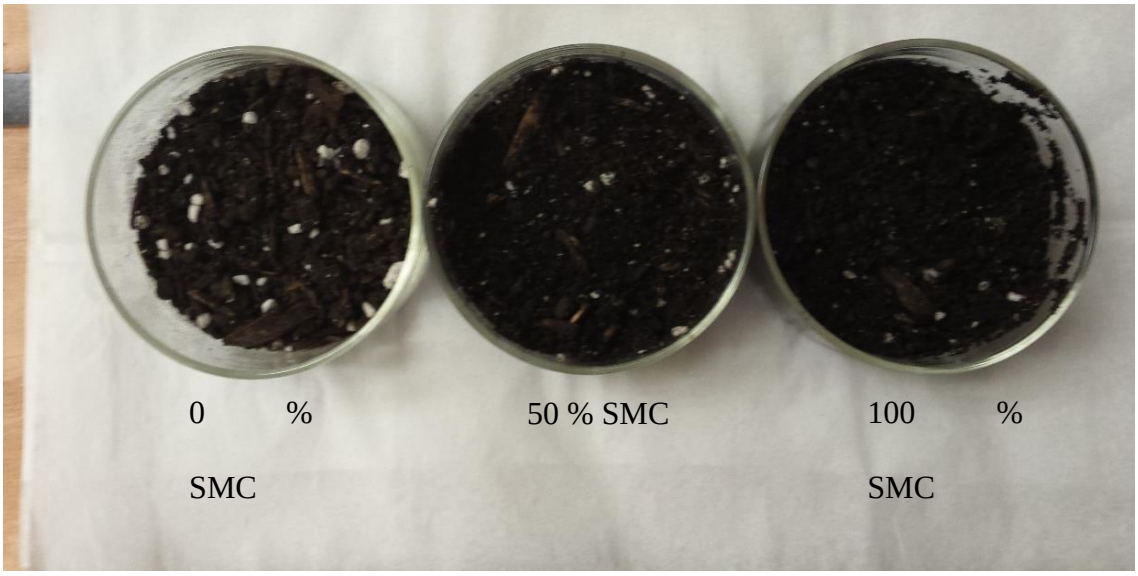

Figure 5-18 Soil samples at 0%, 50% and 100% SMC

5.4 Full-Width Half Maximum Calculation

The resolution of the Argus 2000 instrument is defined by its geometric slit found in the instrument optical entrance. As a result of the finite size of the slit, the FWHM value determines the spectral resolution as the spectral intensity distribution is distorted to some extent by the physical characteristics of the instrument. Previously the full-width half-maximum of the Argus 1000 series instruments had been calculated using a laser beam. Since no laser beam within the spectral range of the instrument is available, a new method is devised.

The full-width half-maximum (FWHM) of the Argus 2000 instrument is calculated through a laboratory experiment using the 1000W. This is done by slewing the instrument

through the collimated light beam as shown in Figure 5-19. The slew is performed by use of the Vernier mount and measurements are taken in steps of 1/10 °.

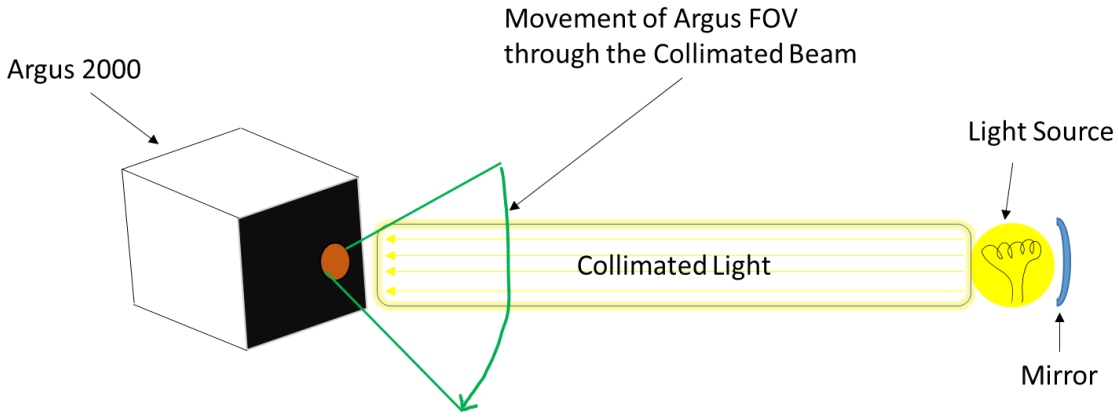

Figure 5-19 FWHM Measurement

The placement of the mirror and light source is performed on a basic table using a standard meter ruler to map out the distances required in order to achieve collimation.

5.5 ASTM E 595 Total Mass Loss and Collected Volatile Materials from Outgassing in a Vacuum Environment

The industry standard test for measuring outgassing in materials is ASTM (American Society for Testing and Materials) E 595. Developed by NASA [74] to screen low outgassing materials for use in space, the test determines the volatile content of material samples placed in a heated vacuum chamber. It measures the Total Mass Loss (TML),

Collected Volatile Condensable Material (CVCM) and Water Vapor Regained (WVR) [75].

This test reveals what vaporized substances are released from solid materials. The substances may cause contamination of spacecraft surfaces and can condense on cold parts of the spacecraft. Materials for human spaceflight demand specialized testing to ensure any outgassing products are not toxic or noxious smelling.

The main equipment used to perform this test is the thermal vacuum chamber (TVAC). The chamber is used normally to test macro-items, but can also be used to testing of micro-quantities. The chamber is equipped with various types of thermocouples in order to ensure the desired temperature is reached inside of the chamber. [76]

The testing was performed from Feb. 27th 2015 to March 2nd 2015 using the measurements methods and apparatus' described in ASTM E 595-98. Multiple numbers of samples were being tested during this time in the TVAC. Each sample must be between 100 and 300 milligrams of mass and is placed into a pre-weighed aluminum foil boat, which has been cleaned and dried. The samples are then bathed in a 24-hour pre-conditioning soak at 25 °C, 50% relative humidity and standard atmospheric pressure to ensure that the samples receive a common preliminary treatment. Following the bath, the individual samples are re-weighed then placed into individual compartments in a solid copper bar which can be heated. Each compartment is closed by a solid copper cover, requiring that all volatile materials escape only through a 6.3 mm diameter exit port.

The Delrin 150SA samples (Figure 5-20) are approximately 5.25+/-.01 mm in dimension, each weighing in the region of 202 milligrams.

Figure 5-20 Delrin 150SA samples prepared for ASTM E 595 test

The copper heater bar is heated to 125° C for 24 hours. The sample is also heated to 125 °C by conduction and radiation. This causes the volatile materials to be driven off, with their only escape being through the exit port. At a distance of 12.7 mm, a chromium-plated collector is in direct line of sight of the exit port and is maintained at 25 °C. The majority of escaping volatiles collect on the chromium-plated disk while barriers near the collector plate to prevent cross-contamination between neighboring samples.

The TML is determined from the weights measured pre and post the 125 ° C soak in vacuum and is presented as a percentage loss, while similarly the weight differences between the cleaned collector and that of the collector with condensed outgassed

materials on it is used to observe the mass of the condensable and is calculated as a percentage of the starting mass of the sample (CVCM). The final value measured is the WVR which is a percentage of the starting mass of the amount of water reabsorbed in 24 hours while the sample is exposed to 25 °C, and 50 % relative humidity bath. During the test, the data parameters listed in Table 5-2 are measured.

Table 5-2 Delrin 150SA data parameters

Parameter	Unit	Parameter	Unit
Test Manager	#	Approx. weight per sample	g
Start Date	#	Position number	#
End Date		Initial holder mass	g
Client ID	#	Final holder mass	g
Thoth ID	#	Initial collector mass	g
Description	#	Cleaned Collector Mass	g
Manufacturer	#	Final collector mass	g
Requestor	#	Position number	#
Sample Temperature	C	Initial holder + sample	g
Collector Temperature	C	Initial + sample after 24hrs	g
Pressure	Torr	Final holder + sample	g
Time at temperature	hours	Reweighed sample + holder	g
Number of samples per boat	#	Initial collector mass	g

6 Results and Discussion

The following sections present the results obtained for the calibration processes and space flight using the methodologies identified in Chapters 4 and 5.

6.1 UAV Platform and Field Results

The field campaign was successful in retrieving the raw counts per pixel of the desired surfaces. In Figure 6-1 the raw counts per pixel are displayed for the coastline data which showcases the snow covered ground and the dark water. The counts per pixel are expected to be higher in the snow covered region as the snow will reflect the sunlight quite well and thus be a brighter course for the spectrometer causing more counts to be registered.

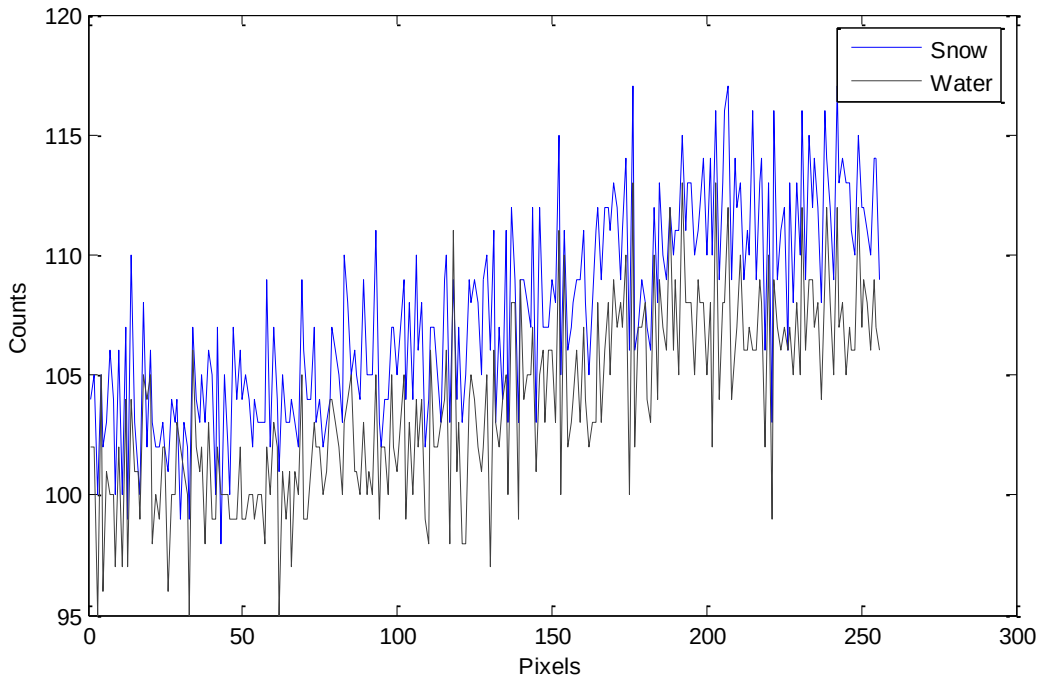

Figure 6-1 Shallow water coastline

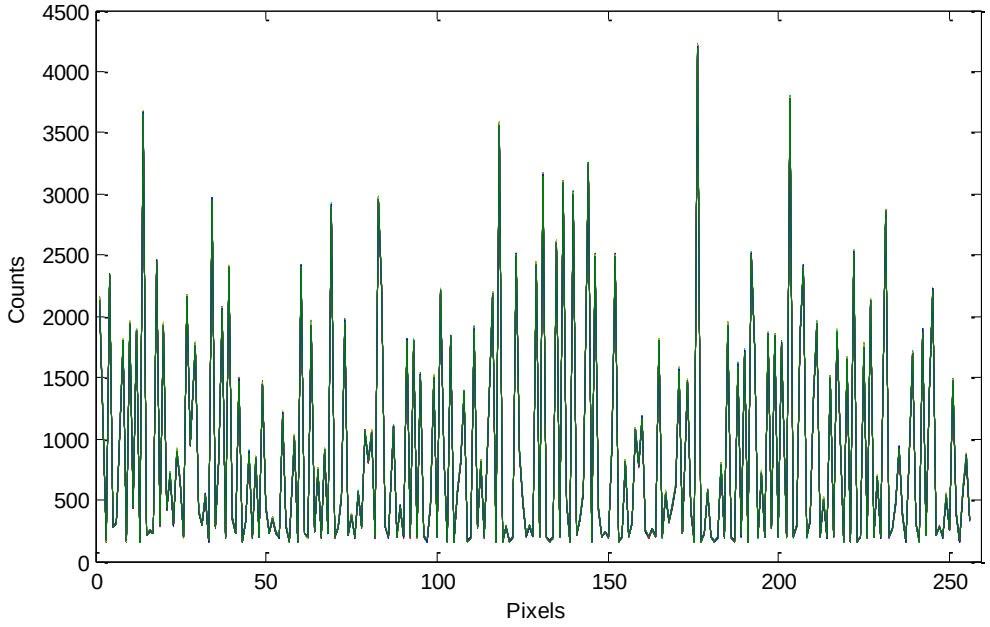

Figure 6-2 Bare soil

Figure 6-2 showcases a typical dark soil sample's raw counts versus pixels. With this data, the process of understanding the soil health, including the soil organic matter content and pH levels of the soil can begin. The soil spectra captured was that of frozen ground.

Figure 6-1 and Figure 6-2 were produced from the data obtained during the first field campaign, while Figure 6-3 and Figure 6-4 showcase the second field campaign.

In the second field campaign the difference of amounts raw data collected in terms of counts per pixel is noticeable. This stems directly from the instrument's integration time being lowered. As found previously, different types of surface are distinguishable. This

comes from the differing albedos of the surfaces. In Figure 6-4, the difference in albedo in-between wet sand, dry sand and the lake are viewed. Surfaces with a lower albedo reflect solar energy less and therefore produce fewer counts for the spectrometer to measure, while the opposite is true for surfaces with larger albedo values.

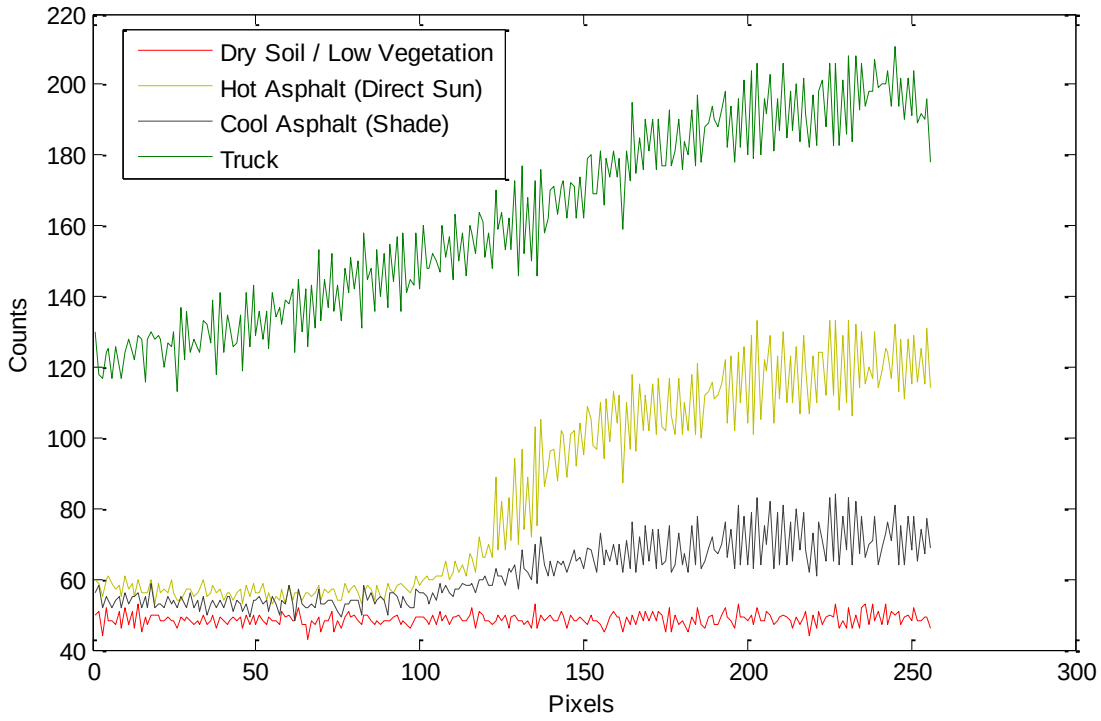

Figure 6-3 Multiple surfaces

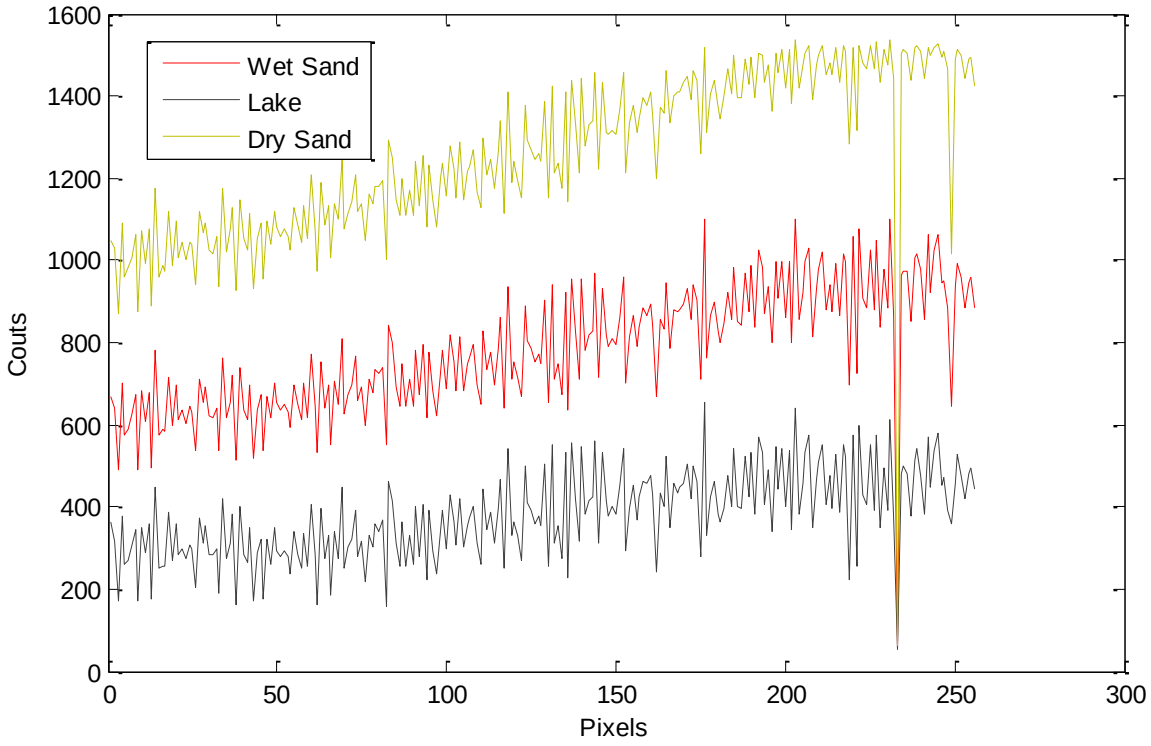

Figure 6-4 Deep water coastline

The photographs taken by the nadir facing camera on the UAV are time stamped and correlated against the Argus data captured. The pixels captured by the Argus spectrometer are marked in order to relate surfaces to data sets. Figure 6-5 and Figure 6-6 are examples of this. In Figure 6-5, the nadir facing camera has shown a flight over a section of dry sand while in Figure 6-6 a lake is showcased. In both figures the outline the Argus pixel overlay. The overlay is just viewable by eye as it is only being three-pixel wide circle on the surface of the far larger nadir GoPro image.

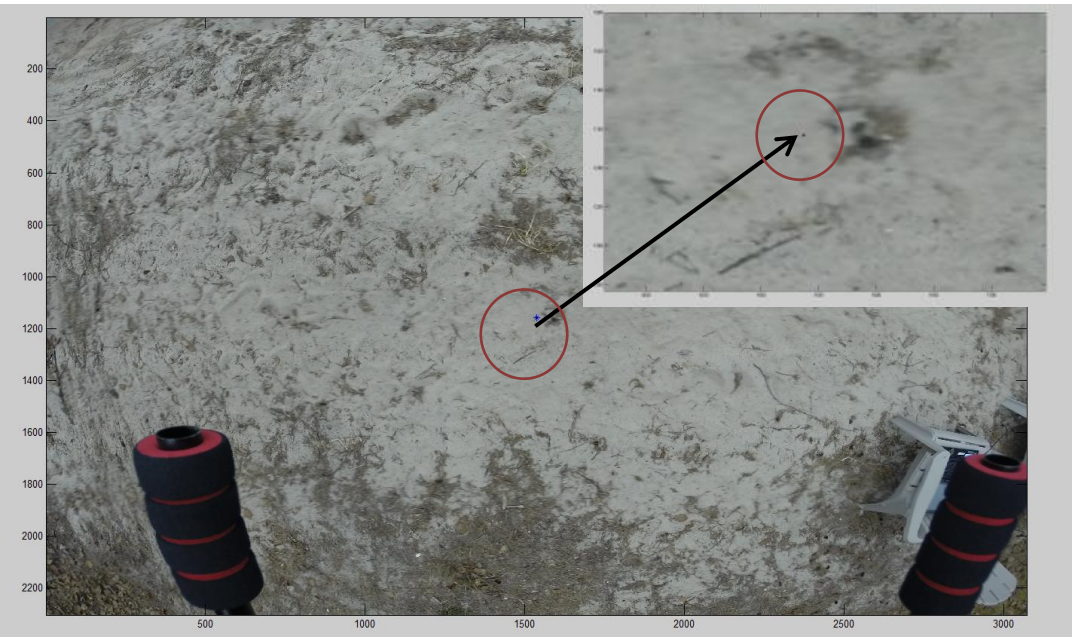

Figure 6-5 Argus Spectrometer: Dry Sand. [6]

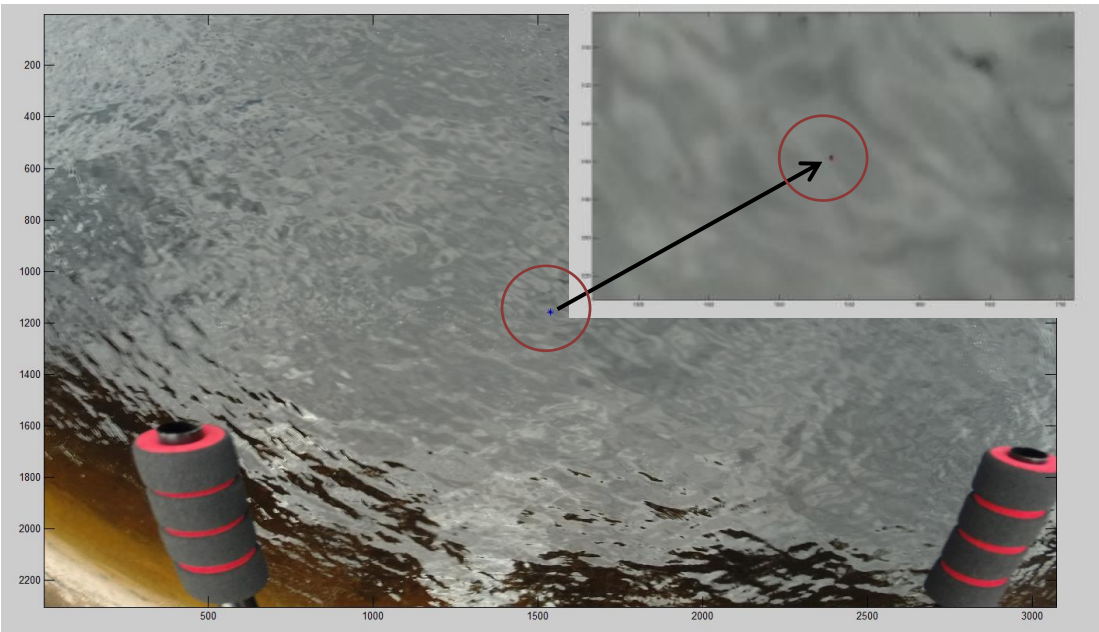

Figure 6-6 Argus Spectrometer: Lake. [6]

6.2 Argus 2000 Calibration

6.2.1 Pencil Lamps

The tungsten-halogen lamp is turned on in order to capture the low intensity Krypton pencil lamp outputs. The values were not discernable from the background noise during the initial view and afterwards in post-processing. The pencil lamp output on the GSE program can be seen in Figure 6-7. The collimated light was on during that measurement. Due to the poor response of the pencil lamp seen, the collimated light was turned off and the Krypton pencil lamp spectra was re-acquired.

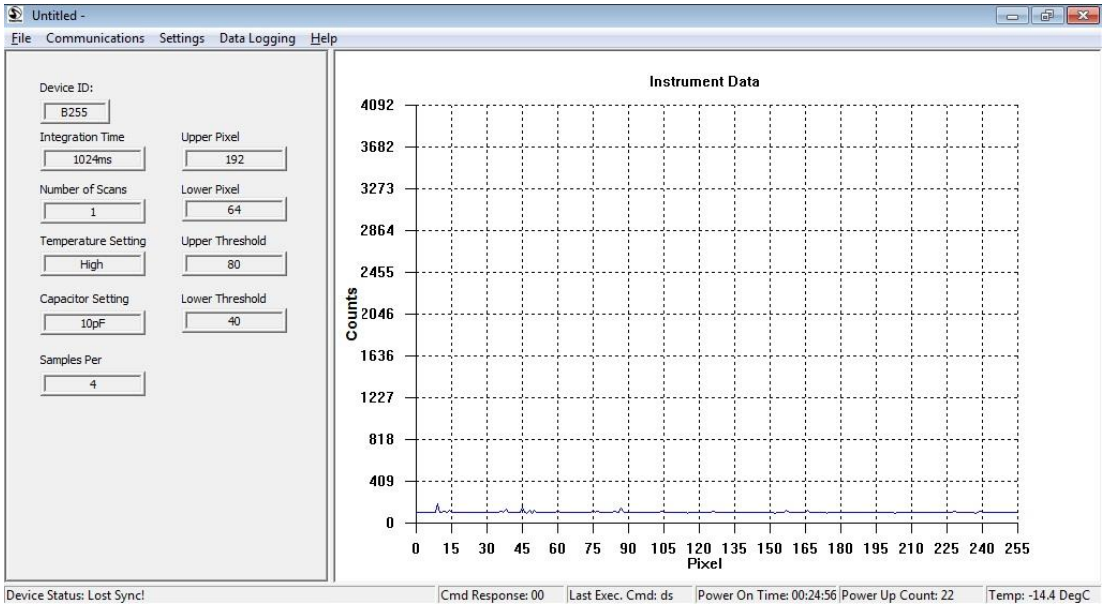

Figure 6-7 Krypton

Figure 6-8 shows the counts measured by the Argus 2000 instrument when the only pencil lamp is producing a signal. The background noise measurement is the middle plot.

It is noted that similar peaking occurs in the same pixel number region as the Krypton pencil lamp. The background signal measured is subtracted from the Krypton signal measured and the resulting dataset is plotted in the lowest graph seen in Figure 6-8. It is seen that the resulting data contains no intensity peaks from the pencil lamp and only a flat line, indicating that the pencil lamp output was not discernable from the background noise measured by the instrument.

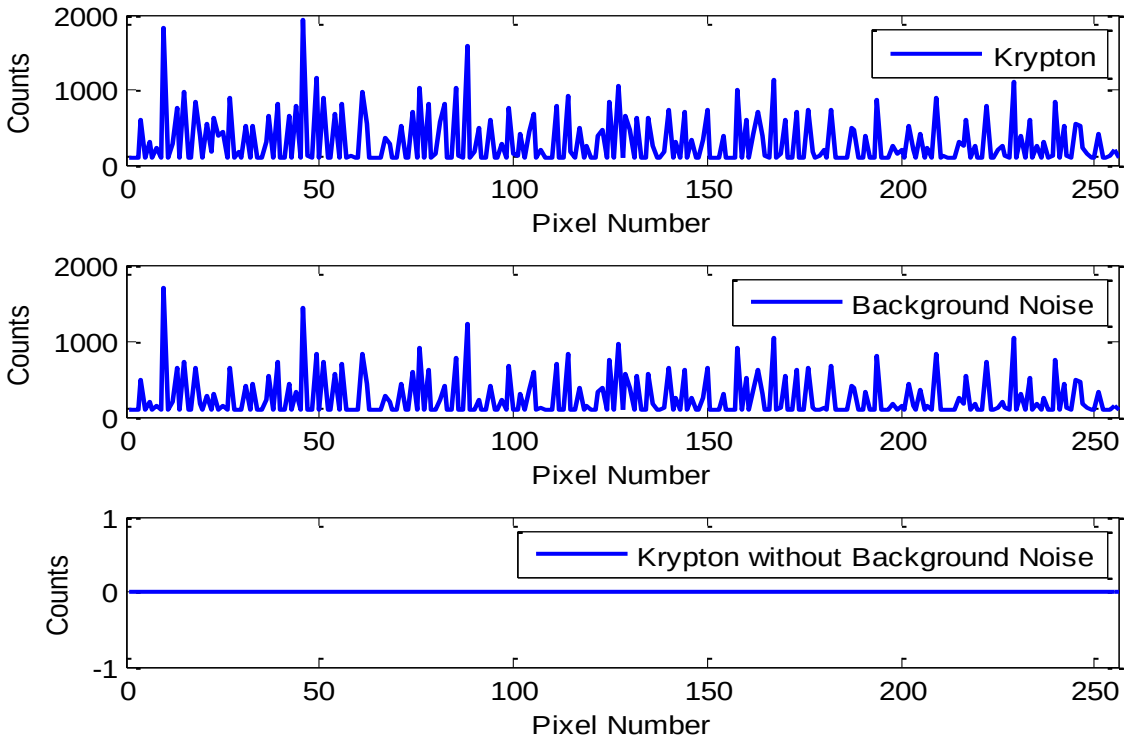

Figure 6-8 Krypton, Background Noise and Signal After Analysis

The theoretical output of the Kypton pencil lamp and the actual output detected by the Argus 2000 instrument is seen in Figure 6-9. The theoretical peaks expected at just under

1700 nm, around pixel 45, are not measured. It is possible that this is a pencil lamp intensity issue as the pencil lamps only uses a low current produce its spectra (10 mA). In order to validate this hypothesis a stronger intensity pencil lamp can be re-imaged.

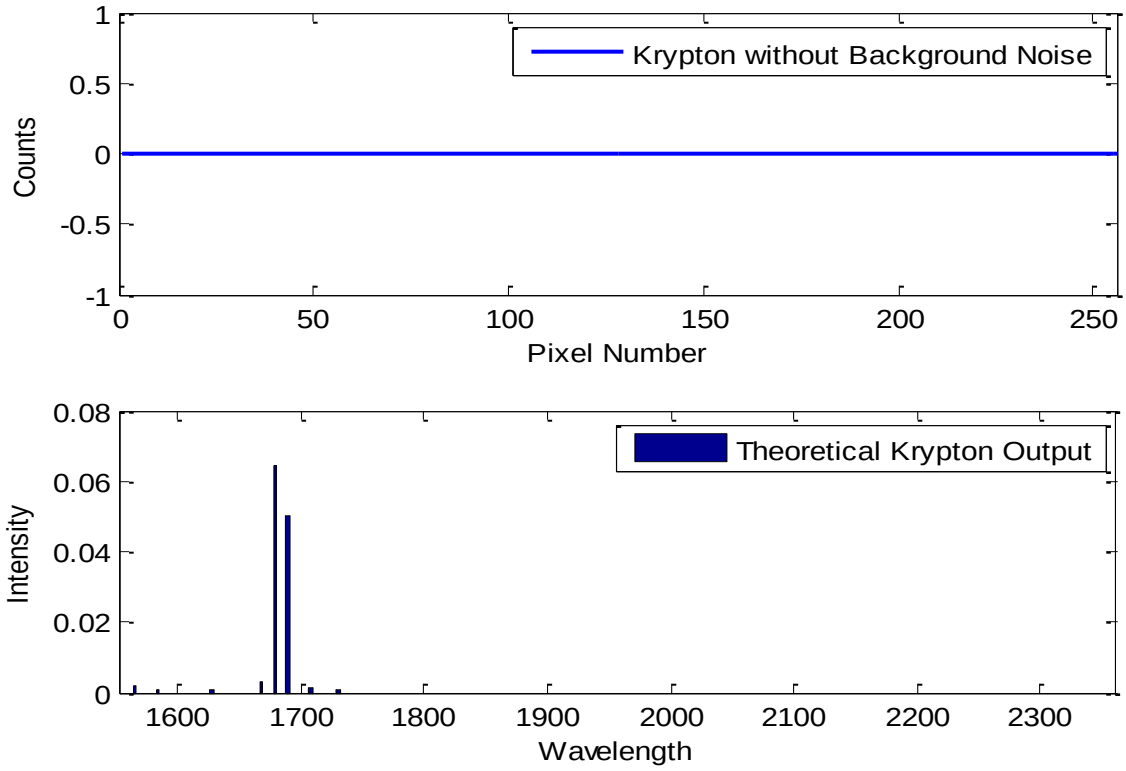

Figure 6-9 Actual Measurement and Theoretical Measurement

6.2.2 Detector and Filter Edge

The tungsten-halogen light is set to give a power output of 500W and the grating is moved to ensure a clear view of detector cut-off edge.

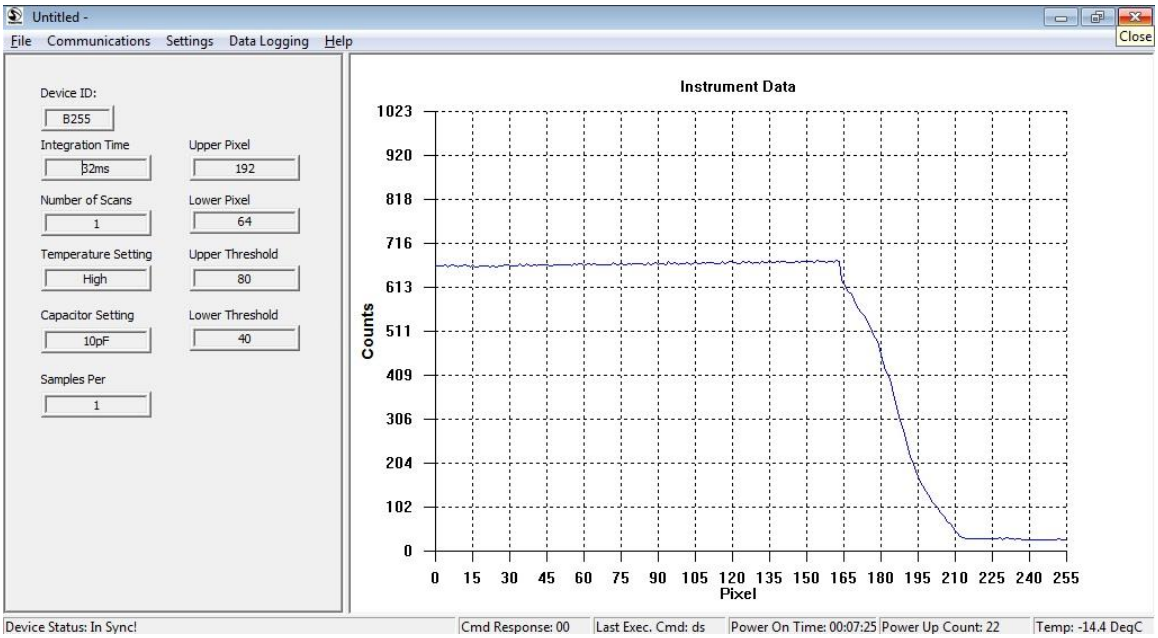

Figure 6-10 Detector Edge on GSE

With the tungsten-halogen light continued to be powered at 500W, the 1600 nm filter is placed in a filter grip and positioned as close to the Argus 2000 input as possible. The clear 1600 nm cut-off from the filter is shown in Figure 6-11 and Figure 6-12.

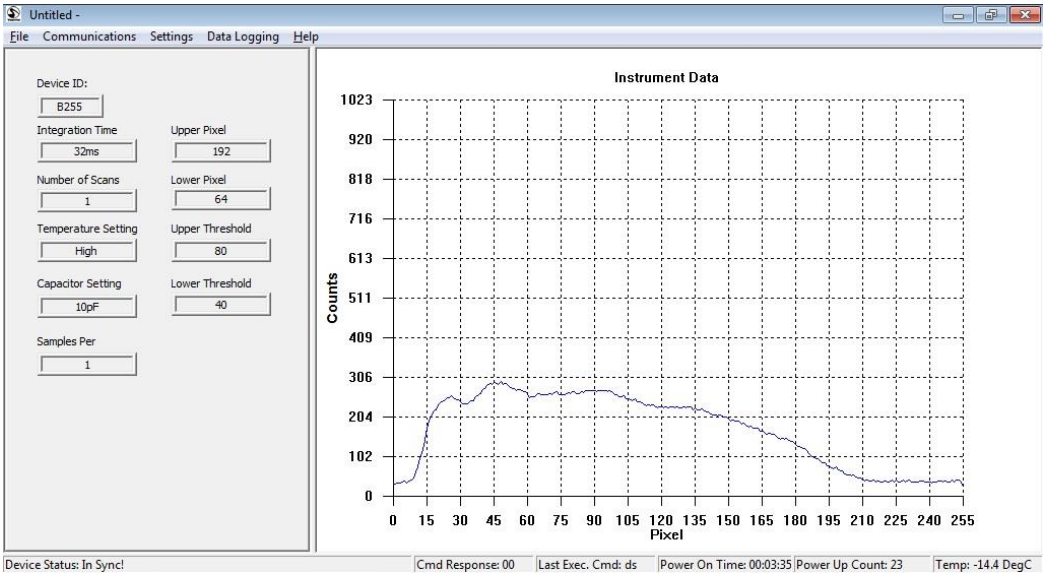

Figure 6-11 1600 nm Filter

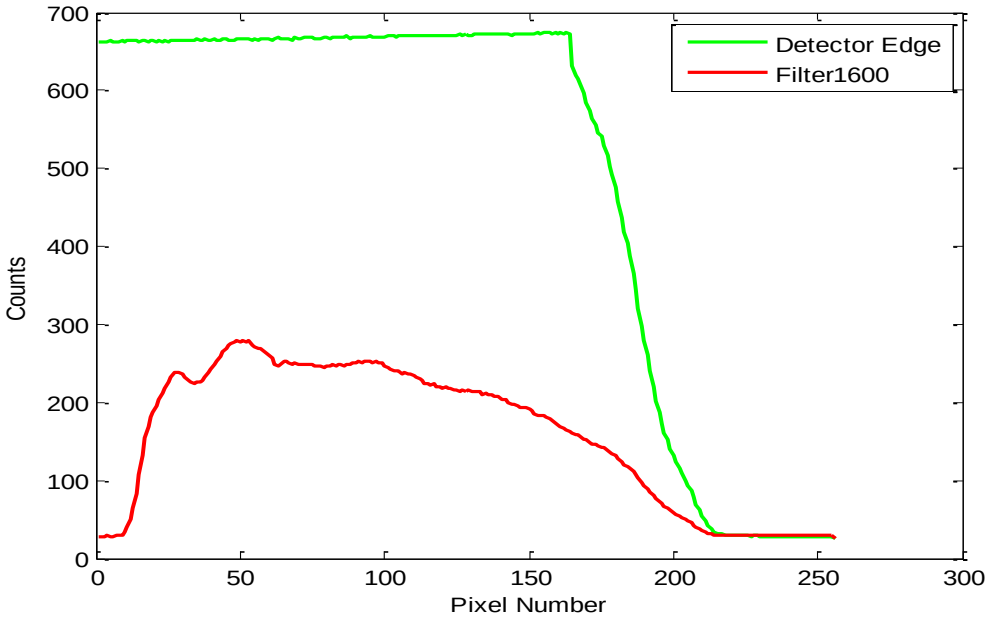

Figure 6-12 Detector and Filter Edges shown

The second derivative method was used to solve for the points of incidence (POI). Each of the theoretical and measured plots were fitted using the Matlab function *polyfit* which provides a linear regression. The second derivative is then computed in order to get the points of incidence. All of the roots or points of incidence are calculated using the built in Matlab function *roots*.

Figure 6-13 and Figure 6-14 are used for the calculation of one wavelength calibration point. This region is concerned with the theoretical and actual detector QE slopes. The theoretical QE slope is obtained from the digitization of the graph given from Sensor's Unlimited. It is fitted using a five coefficient polynomial. Of the POIs found, one, as expected, lies directly in the mid of QE slope downward, where the QE slope changes signs.

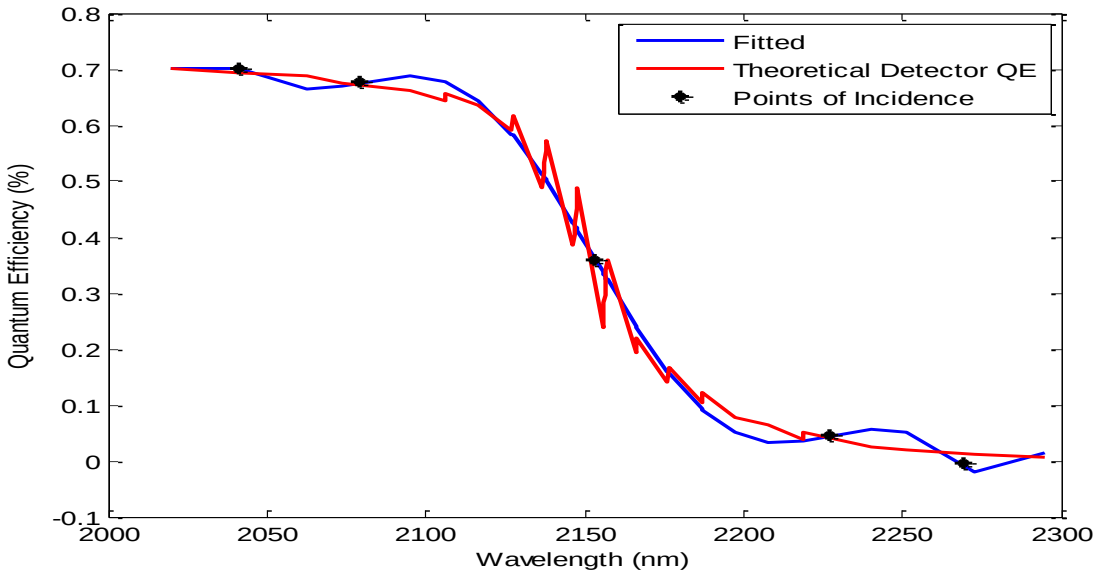

Figure 6-13 POI on Theoretical Detector

Similarly, Figure 6-14 is fitted with five coefficient polynomial and its POIs are plotted. It also shows a POI located in the mid of the downward slope of the detector cut-off. It is assumed that the POIs found for the theoretical and actual detector cut-offs located in the middle of their downward slopes are at the same location. The POIs indicated in Figure 6-13 and Figure 6-14 are referenced to 2153 nm and pixel 189 respectively.

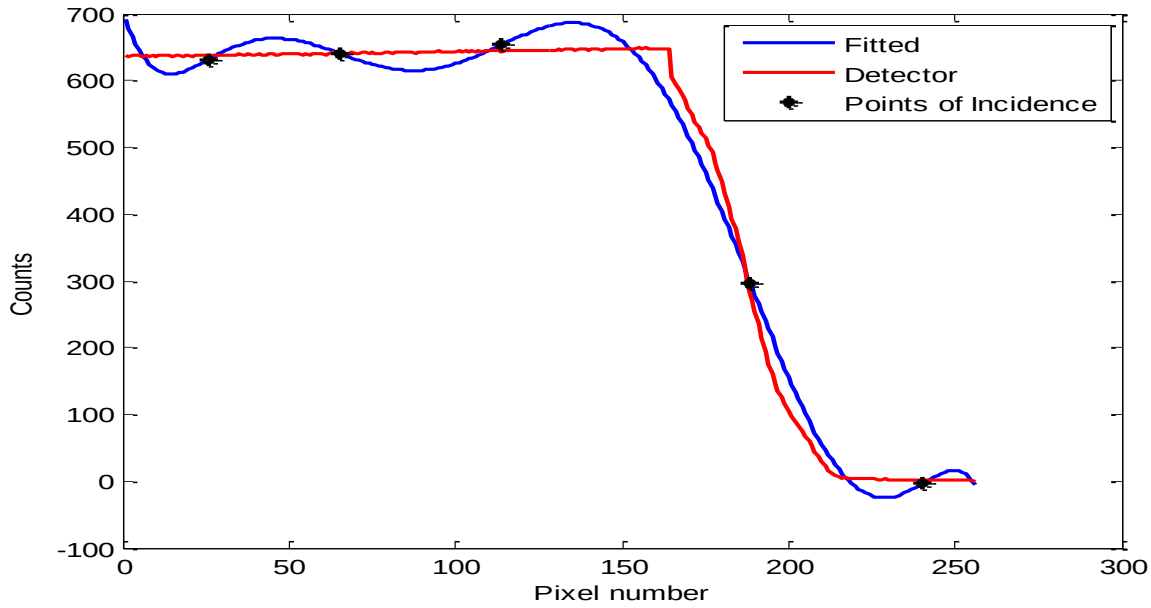

Figure 6-14 POI on Measured Detector

Figure 6-15 and Figure 6-16 are used in the actual and theoretical filter measurements. Figure 6-15 shows the actual filter measurement. It is fitted with a seven coefficient polynomial. As seen previously, a POI lies in the upward slope of the filter. While this POI does not lie directly in the middle of the slope, it does correspond with where the slope changes sign. This POI lies at pixel 15.

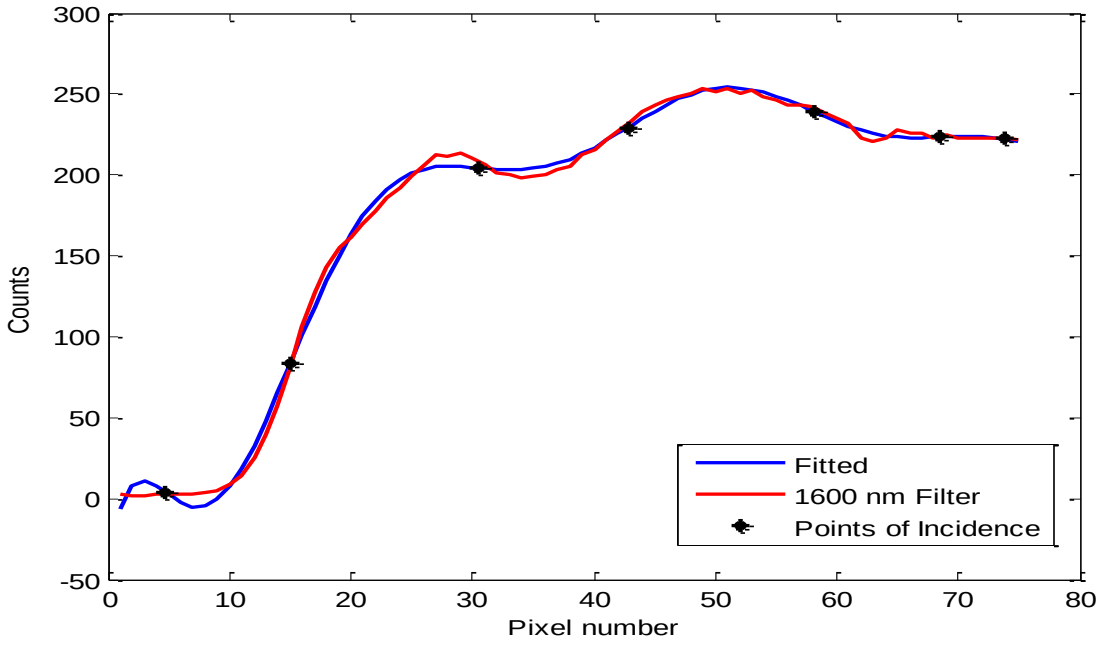

Figure 6-15 POI on Measured 1600 nm Filter

Similarly, in Figure 6-16, a five coefficient polynomial is fitted to the theoretical values and the POI lies in the upward slope of the filter. This point is matched to 1600 nm.

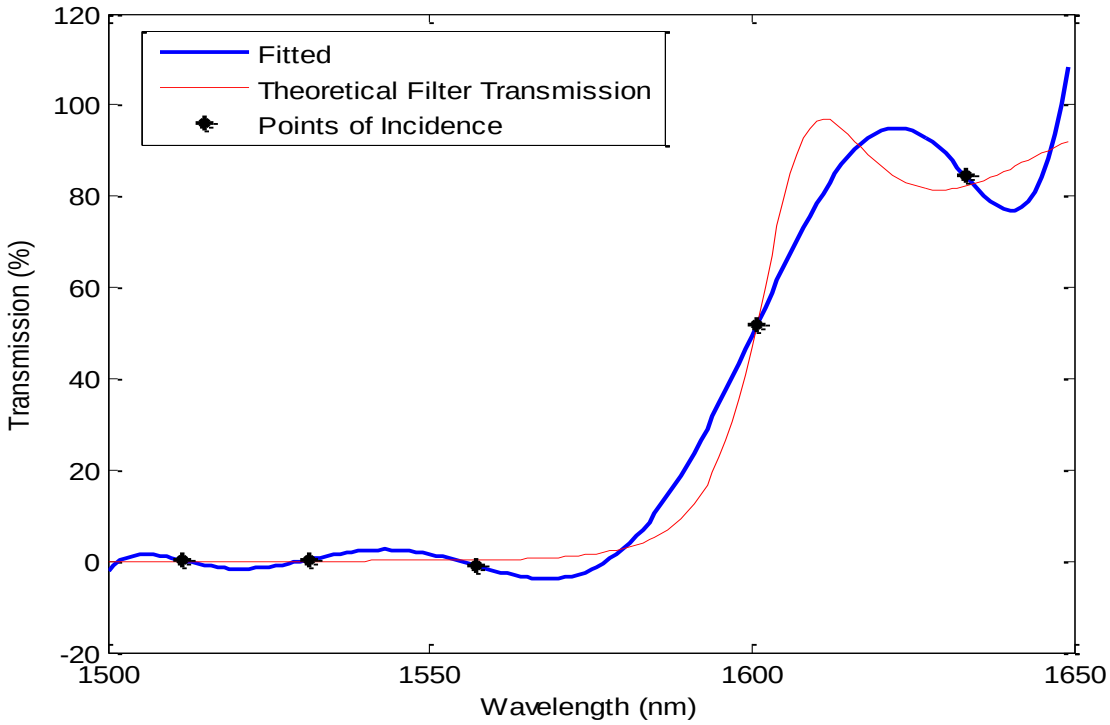

Figure 6-16 POI on Theoretical 1600 nm Filter

The wavelength calibration points were solved for and can be seen in Table 6-1. The accuracy of these findings are within one pixel.

Table 6-1 Wavelength Calibration Results

Calibration Point	**1**	**2**
Pixel Number	15	189
Wavelength (nm)	1600	2153

The wavelength calibration results are used to determine the instrument resolution. The Argus 2000 instrument resolution is found to be 3 nm per pixel.

6.3 Full-Width Half Maximum

The angular sensitivity is plotted for the Argus 2000 instrument in Figure 6-17. The measurement values resemble a Gaussian distribution which is expected. Unexpectedly, the peak of the measurement is not much higher than the baseline of the signal and the slope between the baseline and peak is not steep and sharp but rather slow. The FWHM is measured using Matlab and its value is found to be 0.7066°. This value is far too large considering the throughput of the optics on the instrument have a value of 0.125°.

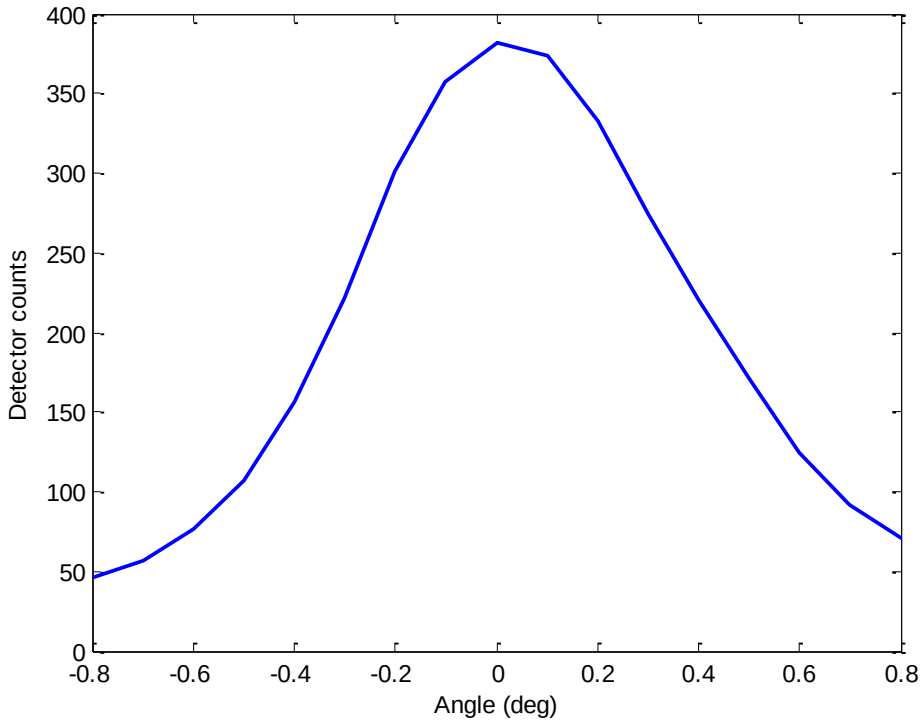

Figure 6-17 Argus 2000 Angular Sensitivity

The ratio of these values is found reveals that the measured FWHM is 5.6528 times larger than it theoretically should be.

The hypothesis is formed that this is due to the poor collimation of the light source. The collimation of the actual value of the light source is measured using a standard tape measure and paper which is used to trace out the size of the collimated beam. The theoretical value of the collimated beam is 3 inches in diameter while the measured value is approximately 16 inches in diameter. This yields a ratio 5.33 times larger radius than the beam is theoretically meant to have and is visualized in Figure 6-18.

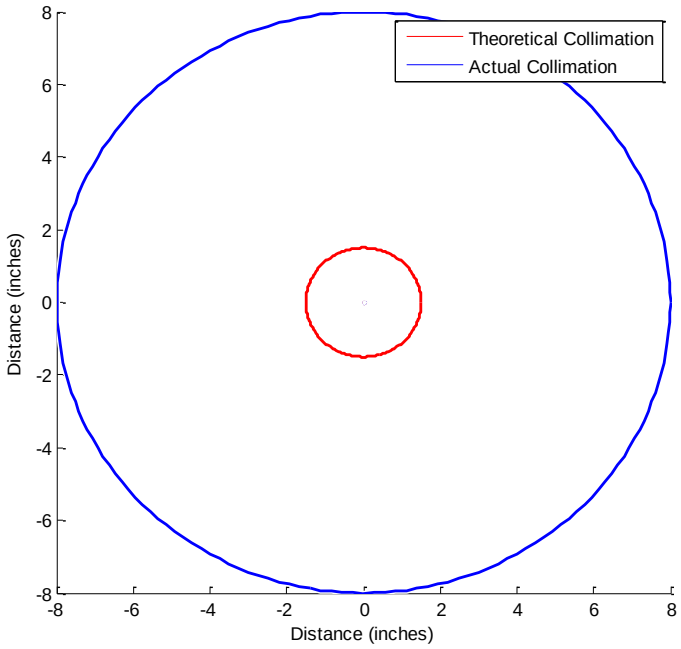

Figure 6-18 Disparity between Theoretical and Actual Collimated Beam Widths

6.4 Soil Spectra Collection

This section reviews the soil spectral measurements taken and the soil baking methodology-error.

6.4.1 Spectra Measurements

Two regions identified for further analysis from GENSPECT modelling were 1964 nm and 2020 nm. These regions are closely examined to see if they could be used in order to view soils with different soil moisture contents.

The soil spectra collected is shown in Figure 6-19 with 0% SMC in green, 50% SMC in red and 100% SMC in blue. The soil-baking methodology produced an error of 2.4%, which then allows for an acceptable confidence level of the SMC value used for spectral analysis. The spectra is represented by the counts measured on the detector shown on the y-axis and the wavelength on x-axis.

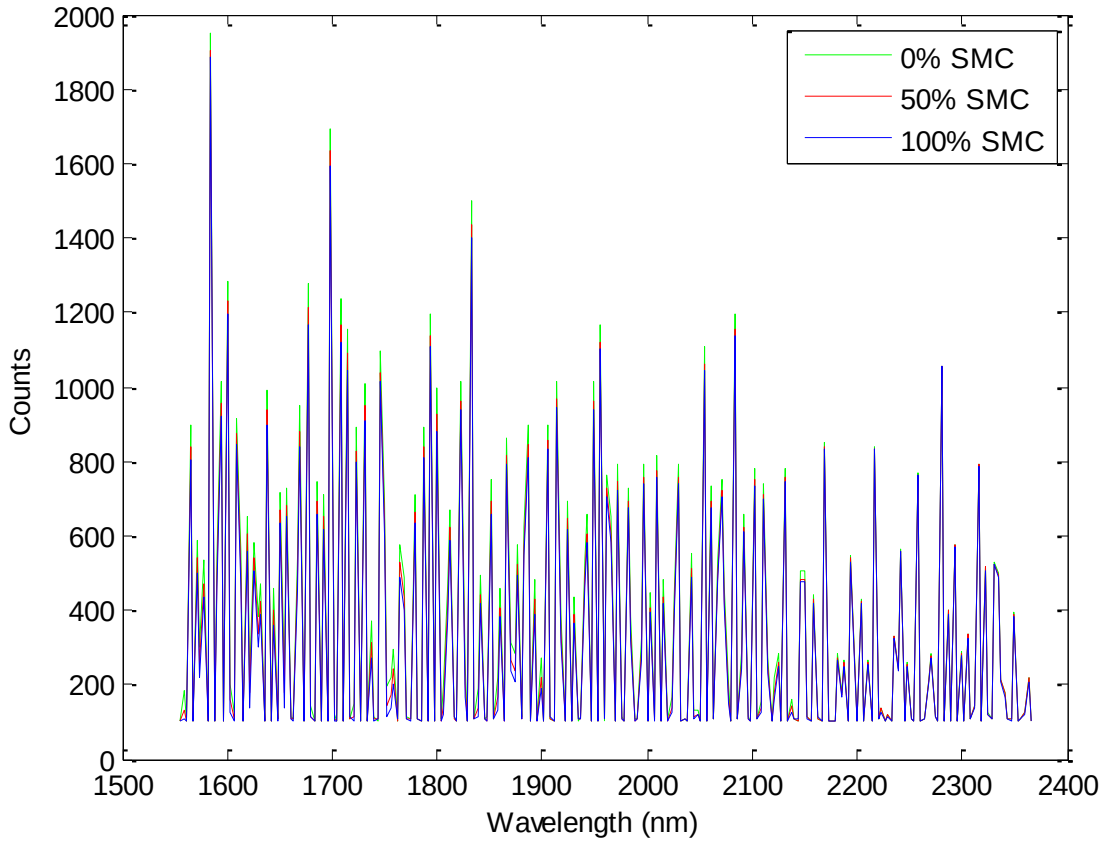

Figure 6-19 Soil Spectra

In Figure 6-20 the region surrounding 1964 nm is viewed. From wavelengths 1962 nm to 1965 nm, the three soil moisture contents are clearly distinguishable with 0% SMC registering with the most amount of counts and 100% SMC with the least amount of counts.

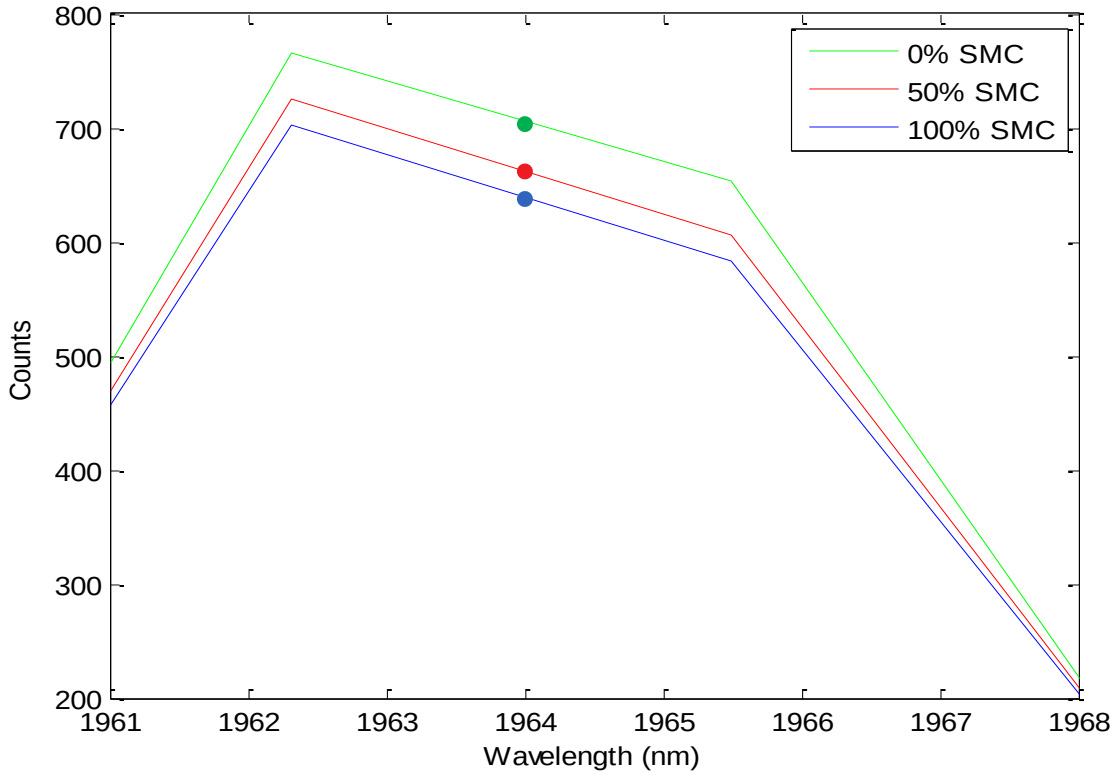

Figure 6-20 Soil Spectra at 1964 nm

These results are expected as 100% SMC soil is visually the darkest sample, thus having the lowest albedo of all the soil samples tested, while 0% SMC has the highest albedo value and is visually the lightest of samples. The albedo values have a direct correspondence on the amount of counts the detector will be able to register, with higher albedo values producing more counts.

Previous to 1962 nm and post 1966 nm the difference in counts registered is quite small, leaving the area in-between a likely resource for the measurement of soil moisture content.

The transmittance of the soil is calculated next using the spectralon as the baseline as seen in Figure 6-21. The 0% SMC shows the highest transmittance value of all the soil samples while 100% SMC is the lowest. The values are at their lowest state at approximately 1965.5 nm.

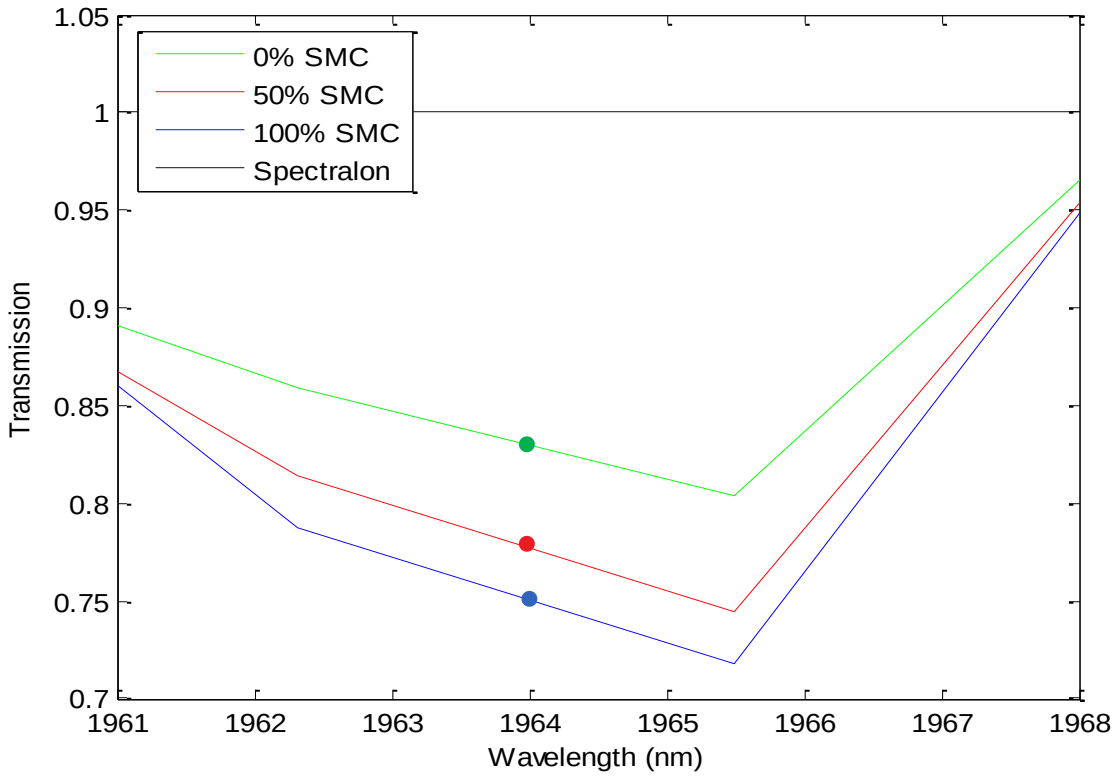

Figure 6-21 Soil Transmission at 1964 nm

The soil spectra are then reviewed at 2020 nm and surrounding areas, is shown in Figure 6-22. Some variance between the three SMC soil samples can be seen at 2016 nm and 2023 nm but not nearly as large as what was previously seen in Figure 6-20. The variance in counts registered peak at 2016 nm and 2023 nm.

Comparably to the 1962 nm results, there are locations at which the variance peak is largest; 2016 nm and 2023 nm. In these locations, 0% SMC registers the largest number of counts, while 100% SMC registers with the lowest number of counts. The variance between 0% and 100% SMC is approximately 60-75 counts.

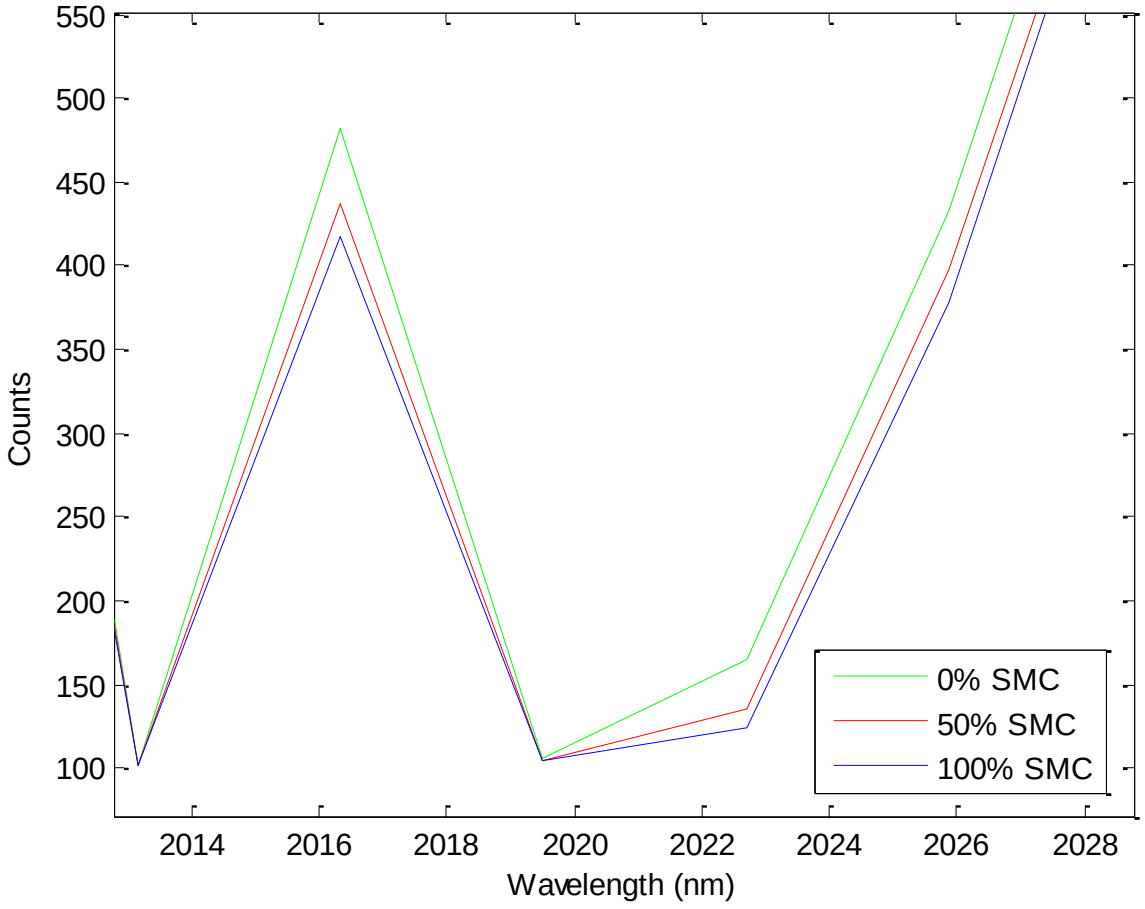

Figure 6-22 Soil Spectra at 2020 nm

The transmittance for the 2020 nm wavelength region is also calculated. Similarly, variances between 0% and 100% exist at 2016 nm and 2023 nm. This is shown in Figure 6-23.

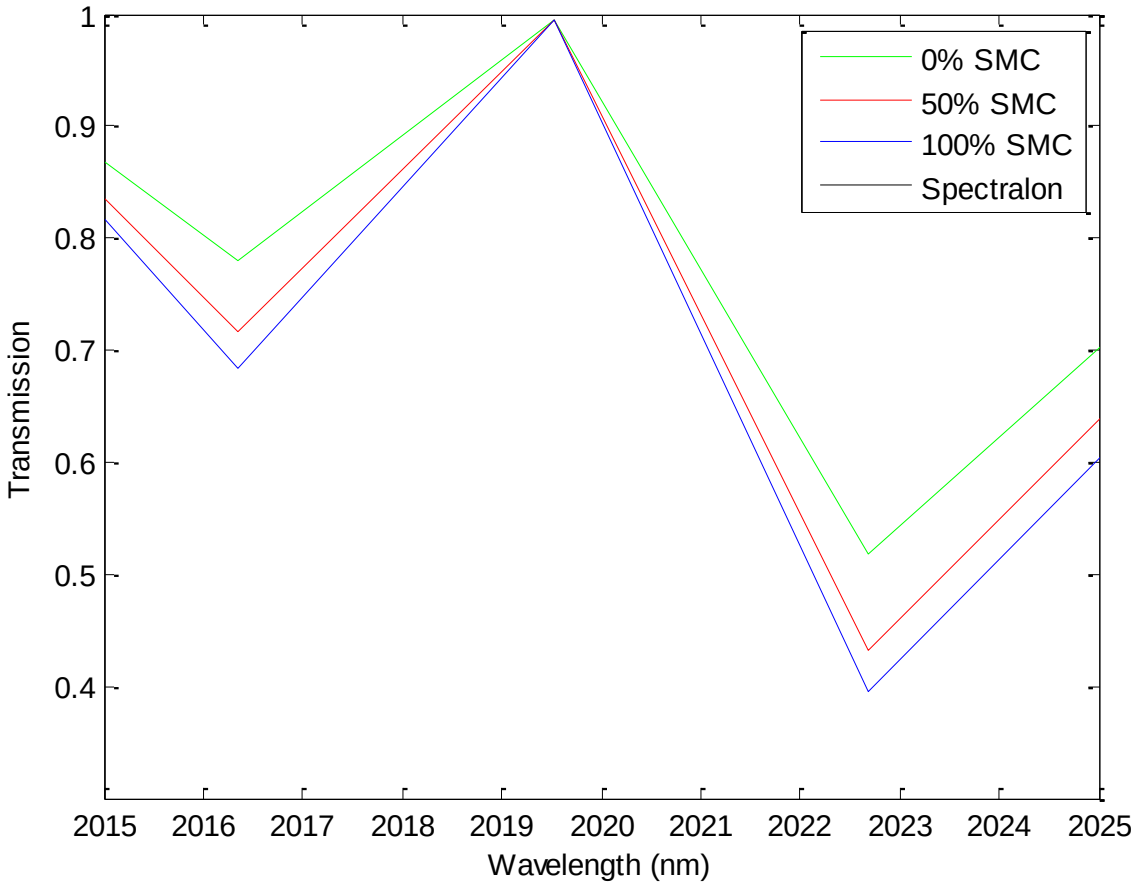

Figure 6-23 Soil Transmission at 2020 nm

The percent-change values are calculated from graphs Figure 6-21 and Figure 6-23 and speak to the relative signal strengths between different SMC levels. The wavelength region at 1964 nm (Figure 6-21) showcases a percent-change from 0% to 50% SMC of 10.39% and from 50% to 100% SMC of 2.66%. The peak percent-change value occurs at 1965.5 nm with a value of 14.5% in-between 0% and 50% SMC.

In Figure 6-23, the percent-change from 0% to 50% SMC is 1.67% and from 50% to 100% SMC of 0.56%. The peak percent-change value occurs at 2022.6 nm with a value of 33.3% in-between 0% and 50% SMC.

The findings are summarized in Table 6-2.

Table 6-2 Percent Change Summary

Wavelength Region	**0% - 50% SMC Percent Change (%)**	**50% - 100% SMC Percent Change (%)**
1964 nm	10.4	2.7
2020 nm	1.7	0.6

These results offer the preliminary analysis that 1964 nm wavelength region has potential to measure SMC remotely.

In preliminary soil moisture spectral collection trials, it was noted that the soil samples' SMC values changed within a short period of time. If the sample was not spectrally measured and then set to bake within a five-minute timeframe, then the sample's SMC value had changed by over 1% loss. This is due to the conditions of the laboratory (laboratory air not held at a moisture stable value and the distance required to travel for the sample to be prepared, then spectrally measured and then baked.

6.5 Instrument

6.5.1 Instrument Precision

The instrument precision is categorized through its 2σ values, the calculated SNR, the linearity of the data, its range and resolution.

The noise data obtained by the instrument is considered to be white noise and thus can be used to calculate the 2σ value. White noise is a random signal consistent with the noise floor of the electronics. A 2σ analysis is used as it represents a 95% confidence bound.

The mean, standard deviation, and 2σ values are calculated for each dataset. The findings are seen in Table 6-3. Each dataset was taken for approximately one minute in order to ensure the SMC content of the soil would not be changed due to the surrounding laboratory climate.

Table 6-3 Instrument Precision

SMC %	Number of Packets	Mean Counts	Standard Deviation 1σ	2σ Uncertainty
0	261	653.89	17.23	34.46
50	280	605.27	21.25	42.50
100	330	583.80	18.98	37.80

It is noted that the mean counts appear to decrease in value while the SMC value is increased. The 1σ and 2σ values do not follow that trend but instead stay relatively consistent from differing SMC values.

The SNR of the instrument is solved through use of Equation (6-1), standard for image processing. The signal mean counts are represented by μ and σ is the standard deviation of the background noise.

$$SNR = \frac{\mu}{\sigma} \qquad \textbf{(6-1)}$$

The calculated SNR values are seen in Table 6-4. The SNR values range from 539:1 at 0% SMC to 479:1 at 100% SMC. This reflects that the signal received at the detector is higher at 0% SMC than at 50% or 100% SMC. The SNR value decreases at the SMC value increases. At 479:1 SNR, an SMC variance of 21% can be measured. In order to distinguish between a smaller variance in SMC measurement, the SNR value would need to be increased.

Table 6-4 SNR Value

SMC Value	SNR
0%	539:1
50%	497:1
100%	479:1

The preliminary range values were chosen to be 0% SMC to 100% SMC. This allows for a generalized performance overview to be obtained. This directly ties in to the thesis objective to see if varying levels of SMC can be measured and provide a basis regarding further instrument and laboratory studies.

The linearity of the mean values is next diagnosed. A fitted line is matched to the three datasets and is observed to fall within the 2σ variance of the mean count. This is visualized in Figure 6-24. The mean detector counts values are placed in a scatterplot. The error bars show the 2σ variance. The linearity function, shown by the red line, flows within the error bars of the three datasets. The R^2 value is found to be 0.9523, signifying the datasets closely match the fitted regression line.

The resolution of the datasets is measured by placing the mean counts obtained for each dataset against the laboratory-determined saturation level of the instrument. The datasets taken use data integration time setting in order to deliberately avoid instrument saturation. The instrument reaches saturation approximately at 2000 counts so the calculated mean counts range of 654 to 583 is well below that value.

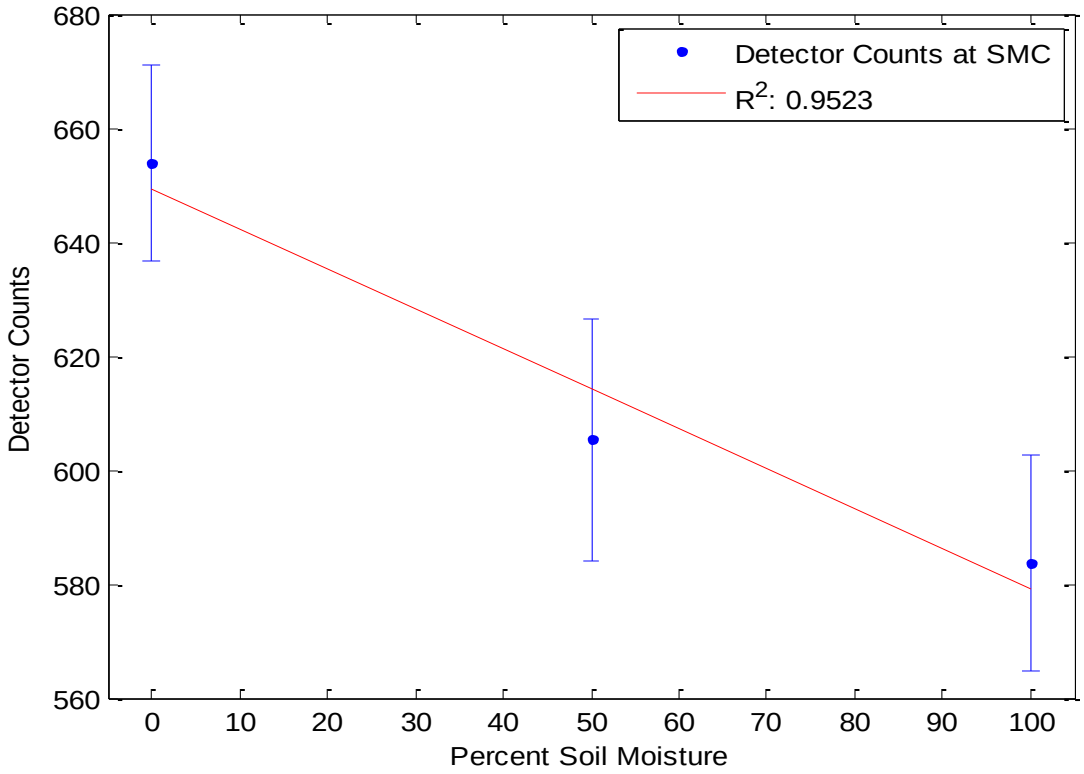

Figure 6-24 Mean Counts, Standard Deviation and R-squared

A minimum of three distinct levels of soil moisture are measurable, as shown in the laboratory studies. To further perform a sensitivity analysis, spectral measurements can be taken on the absorption SMC band and off it. The ratio of these samples provides a measurement sensitive to SMC while reducing factors such as variations in illumination that might distort results.

6.5.2 Instrument Use

The new technology proposed in this thesis for soil moisture content measurement showcases technology innovation. The Argus 2000 instrument is meant to be showcased on small spatial scale such as microsatellites. It is there where the features of the instrument, mainly size, low mass, low cost, and implementation-to-microsatellite constellation readiness shine. Further-more the instrument can provide near real-time analysis of ground conditions. Combined with an imager, the new integrated system can provide even more suitable data ready for analysis of ground conditions.

The proposed soil moisture content (SMC) measurements are not without limitations. These limitations begin with the penetration depth of infrared radiation – approximately 1 μm in the near-infrared spectrum [77]. The penetration depth is based on three factors; wavelength, angle of incidence, and refractive index [77]. The surface geometry also plays a role. For model purposes, often the surface is portrayed as smooth with a static albedo value yet in reality this is not often the case. Surface geometry (plane, concave, convex), thickness, surface quality (polished, rough, oxidised, sand-blasted) all play a role on how infrared radiation is reflected back to the sensor.

While the instrument's original use is for soil moisture content, the spectral region analysis performed in 3.1.3 shows other uses. Specifically, the instrument, if placed in space, could measure the atmospheric columns of CO_2 and CH_4. If the instrument is used on land for soil science purposes, it's spectral region coverage would allow it measure soil salinity, soil-phosphorus concentrations, and soil-clay content.

7 Conclusion and Future Work

The studies and work performed for this thesis have shown that a potential exists to monitor soil moisture content by use of remote sensing methods in space. The atmospheric constituents' spectral information has been studied and two regions of interest in the SWIR, 1964 nm and 2020 nm, have been identified as spectral windows and potential locations that can be used to monitor SMC. The instrument designed can detect a SMC variance of 21% due to a 479:1 SNR calculation.

A UAV was designed, built and tested using an Argus 1000 instrument in order to ensure the scientific platform was capable of performing spectral data acquisition fieldwork. This UAV was tested over the coastline region of Lake Traverse in Algonquin Park, with three flights performed obtaining coastline and various surface spectral data. During the second coastline run, the UAV failed and the choice of a Y-6 frame design was put to the test. The frame design allowed for motor failure in flight without loss of instrument or ability to control the UAV.

Using these wavelength regions, the Argus 2000 grating spectrometer was designed. This instrument uses new optical tools and incorporates a larger chassis in order to provide the ability to measure in the short wave infrared region. The instrument was wavelength calibrated in order to ensure the SWIR region of the desired object was to be measured.

Soil samples were then prepared and had their spectra measured using the Argus 2000 instrument. The spectra showed that indeed both regions were locations in which varying

SMC measurements could be made. Of the two regions, 1964 nm is preferred due to the variance of counts measured within the SMC levels seen.

The Argus 2000 instrument is a tool that can potentially be used to measure SMC from space. It has been seen that the instrument functions within the desired spectral region and that it can distinctly measure different SMC levels.

7.1 UAV Platform and Field Results

A low cost, COTS UAV system was built as a scientific tool to perform remote spectral data collection. The UAV consisted of a Y6 frame design (six motors on three arms). For areas where hand-collecting spectral imagery is not an option, the UAV provides an opportunity to log data in a quick and efficient manner. The UAV will continue to provide a good platform for remote spectral studies in the future and allow scientists a new method for acquiring remote spectra otherwise not obtainable.

The data collected can be used towards specifying further targets of interest for both continuing UAV and space-based viewing campaigns for data collection. All of the raw data is to be released online as part of a spectral data campaign.

The Argus settings for further UAV campaigns have been noted, as well as which settings allow for non-saturated raw data to be acquired.

7.2 Argus 2000

7.2.1 Instrument Design

The Argus 2000 instrument was modelled after the Argus 1000 instrument and modified for a new wavelength region. The modifications included a new model of InGaAs linear array, a 600grooves/mm grating, a change in chassis size and different optical filters.

The change of InGaAs linear array was easily incorporated into the new design. It fit into the mount well and was able to be kept in a precise location within the chassis. The mount design did not interfere with the optical cover and allowed for the height of the spectrometer to remain the same as in the Argus 1000 instrument.

The new grating also was easily incorporated and fit into the mount well. There were no issues with its' placement and mounting.

To block the lower wavelength light from being detected on the InGaAs linear array, a filter is used. The Techspec 1600 nm Longpass OD>2.0 filter was purchased from Edmund optics. Unfortunately, the filter did not stop the transmission of visible light and due to market availability, a suitable substitute for the Techspec 1600 nm longpass filter was unable to be sourced. Instead a secondary filter was acquired; FELH1300 from Thorlabs. The filter transmission data clearly showcased a blockage of all radiation up to 1300 nm where transmission then begins to occur. A set of mathematical equations were found and studied to comprehend how light would transmit between the filters. These results suggest that the use of two filters in the instrument design is flawed and unnecessary, therefor only one filter will be used. The filter chosen is the Thorlabs FELH1300 longpass filter allows for its ability to block radiation in the NIR and VIS spectral regions.

7.2.2 Instrument Calibration

The instrument calibration for Argus 2000 consists of wavelength calibration. The wavelength calibration consisted of trialing pencil lamps, utilizing filter cut-off edges and the detector cut-off edge

From on the datasets measured, the pencil lamps did not produce enough intensity for the Argus 2000 instrument to detect. The wavelengths used for calibration came from to use the filter edge and detector edge.

The second derivative method was successfully used to provide calibration points for each end of the detector using the data captured by use of the 1600 nm filter and the physical detector cut-off. These points were solved to within one pixel. Each pixel has a 3nm resolution so the error associated with the measurements is +/- 3 nm or +/- 1 pixel. The corresponding spectral points were found to be pixel 15 (1600 nm) and pixel 189 (2153 nm).

7.3 Soil Spectra Collection

7.3.1 Soil Baking and Error Analysis

Soil baking was performed in the laboratory in order to understand the limitations and accuracy of creating soil moisture. The methodology is taken *American Society for Testing and Materials* (ASTM) 2216-98. First all moisture is baked off from the soil

sample and then water is added in order to obtain the desired soil moisture content. The soil baking methodology proved to work well with the error measurement resulting in 2.4%. That is to say if a 90% SMC is desired, due the laboratory tool limitations the soil moisture content could be between 87.6% – 92.4 % SMC.

7.3.2 Spectral Measurements

The spectral measurements proved well, resulting in the confirmation of two wavelength regions that can have potential use for measuring soil moisture content. The 1964 nm section proved to show a greater variance in the number of counts registered in comparison to the 2020 nm region, however, both have a potential for use. The 1964 nm section is more favorable as it features a consecutive three (3) nm span where the variance between SMC levels in constant, and eight nm span where the variance between levels in visible. Ideally the region to be used should span three pixels of measurement on the detector. With the current instrument design, the region only spans two pixels fully.

The current instrument design produced a 3.14 nm instrument resolution; with a change in input filter and slight detector re-positioning, it may be possible to obtain a 2 nm instrument resolution. This resolution would allow for three consecutive pixels to be measured.

In preliminary soil moisture spectral collection trials, it was noted that the soil samples' SMC values changed within a short period of time. In order to evade this source of error, future spectral measurements, ideally, should be made in a laboratory setting which

contains all of the scientific tools needed for soil preparation, spectral measurement, and soil baking. The laboratory setting should be air-moisture content and temperature stable.

7.4 Full-Width Half Maximum

The Full-Width Half Maximum (FWHM) results gave light to how much the measurement is dependant on the source of illumination and its collimation. Unfortunately, the FWHM were poor, showcasing poor light source collimation.

The collimation must be performed using better equipment to set the distance requirements in-between the mirror and light source. The experiment should be performed in a dark room after proper collimation has been achieved.

7.5 ASTM E-595 Total Mass Loss and Collected Volatile Materials from Outgassing in a Vacuum Environment

The industry standard test for measuring outgassing in materials is ASTM (American Society for Testing and Materials) E 595 which determines the volatile content of material samples placed in a heated vacuum chamber. Three cubes of Delrin 150SA were prepared and placed in the process of sitting in a 24-hour pre-conditioning soak at 25 °C, 50% relative humidity and standard atmospheric pressure to ensure that the samples receive a common preliminary treatment. The sample is heated afterwards to 125 °C for 24-hours by conduction and radiation causing the volatile materials to be driven off. The samples sit through a second post-conditioning soak. Materials pass or fail the test based

on these TML and CVCM measurements. If the CVCM exceeds 0.1%, the material fails. The material will also fail if the TML exceeds 1%—though the TML may be offset by water vapor regained (WVR) by the sample in a subsequent measurement.

The Delrin 150SA samples passed the TML testing.

7.6 Instrument Precision

The instrument precision is categorized the calculated SNR, the linearity of the data, its range and resolution.

The SNR values range from 539:1 at 0% SMC to 479:1 at 100% SMC. This reflects that the signal received at the detector is higher at 0% SMC than at 50% or 100% SMC. The SNR value decreases at the SMC value increases. At 479:1 SNR, an SMC variance of 21% can be measured.

The linearity of the mean values is next diagnosed. A fitted line is matched to the three datasets and is observed to fall within the 2σ variance (error bars) of the mean count. The R^2 value is found to be 0.9523, signifying the datasets closely match the fitted regression line.

The dataset range was set at 0% to 100% SMC.

The resolution of the datasets is measured by placing the mean counts obtained for each dataset against the laboratory-determined saturation level of the instrument. The mean counts were found to be slightly less than half of the counts at saturation level, thus providing an acceptable instrument resolution.

7.7 Future Work

During the next field campaigns, a calibration target of spectralon or something of equal effect should be imaged using the UAV and data acquisition system. This data can be used to obtain the albedo values of the varying surfaces in the short-wave infrared spectrum. These settings should be compared against future field work surveys with similar weather conditions to see if a correlation exists. An Argus 2000 instrument should be used in order to confirm its' flight-readiness.

Future calibration methods would ideally involve obtaining a laser that outputs within the desired spectral region and performing the wavelength calibration once again and ensuring this method produced accurate results.

A few areas were marked for improvement for soil baking methodology; the use of less soil in containers, re-performing tests with soil that has been sifted to ensure all particles are the same size, and the use of more precise measurement tools.

If less soil would be used in each container, smaller containers could be used and then more samples baked at the same time, resulting in the collection of a larger database in a timelier manner. If then the soil is sifted pre-mixing with distilled water and testing, then the effect of grain size on the resulting SMC calculated could be defined. With more precise measurement equipment for the distilled water addition to the soil, the error associated with the soil preparation and baking process would be reduced. The current equipment used was limited in its performance and made it difficult to obtain less than 5 ml accuracy.

For future soil laboratory testing measurements, the following should be explored to understand how they affect spectral measurements of SMC:

1. Soil grain size
2. Soil composition (percentages of sand, clay and loom)
3. Soil pH

Futhermore, the methodologies presented in this thesis could be improved through further research. A larger dataset and process-review would allow for an improved analysis method to emerge.

Further testing is required in order to characterize if Delrin 150SA could be used in space or not. The recommended tests are [78]:

1. Thermal Cycling
2. Ionizing Radiation
3. Ultraviolet Radiation
4. Atomic Oxygen

Thermal cycling is performed in order to simulate the temperature shifts an object in orbit would experience. The temperature range and frequency of thermal cycling can be increased as a means of deriving a test item's lifetime performance. Ionizing radiation testing is normally performed for electronics and optics. Depending on what type of instrumentation would incorporate Delrin 150SA, this test might be performed. Ultraviolet radiation testing is performed in order to understand how the physical

properties of Delrin 150SA could change, as ultraviolet radiation is known to degrade plastics. Lastly, atomic oxygen has been known to erode plastics.

The instrument precision needs to be further analyzed. Some methods are presented for future work.

The range of the SMC values could be explored more in depth. Currently the SMC values measured jumped by 50% per measurement. In subsequent measurements, a variance of 10% SMC could be studied. This would be useful to understand the change in mean detector counts and if the instrument would be able to distinguish between lower stages in order to distinguish the lowest stage that the instrument could perform at for a certain type of soil.

The variation in the resolution studies will present sufficient data to provide further SNR analysis. It can then be seen if the SNR continues to follow the downward trend as the SMC values increase. Increasing the SNR value would allow for higher precision measurement to be made.

8 References

[1] United Nations Office for Outer Space Affairs, 2015. [Online]. Available: http://www.un-spider.org/links-and-resources/data-sources/dsotm-soilmoisture. [Accessed 17 November 2015].

[2] G. Certini and R. Scalenghe, Soils: Basic Concepts and Future Challenges., 1st ed., Cambridge: Cambridge University Press, 2006, pp. 55-58.

[3] C. Du and J. Zhou, "Evaluation of soil fertility using infrared spectroscopy: a review.," *Environmental Chemistry Letters,* vol. 7, no. 2, pp. 97-113, 2009.

[4] UTIAS SFL, "Canadian Space Agency Awards Micro-mission Cluster Pilots Project to SFL," 2014. [Online]. Available: http://utias-sfl.net/?p=992. [Accessed 4 March 2016].

[5] C. Tsouvaltsidis, G. Benari, N. Z. Al Salem, B. Quine and R. Lee, "ArgusE: Design and development of a micro-spectrometer used for remote Earth and," in *Proceedings of the Advanced Maui Optical and Space Surveillance Technologies Conference*, Maui, HI, 2015.

[6] C. Tsouvaltsidis, N. Zaid Al Salem, G. Benari, D. Vrekalic and B. Quine, "Remote Spectral Imaging Using A Low Cost UAV System," *The International Archives of Photogrammetry, Remote Sensing and Spatial Information Sciences,* vol. 1, pp. 25-

31, 2015.

[7] J. Kim and T. Hogue, "Improving Spatial Soil Moisture Representation Through Integration of AMSR-E and MODIS Products," *IEEE Transactions on GeoScience and Remote Sensing*, vol. 50, no. 2, pp. 446-460, 2012.

[8] B. Stenberg, R. Viscarra Rossel, A. Mounem Mouazen and J. Wetterland, "Visible and near infrared spectroscopy in soil science," *Advances in Agronomy*, pp. 163-215, 2010.

[9] R. Miller and R. Donahue, Soils: An Introduction to Soils and Plant Growth, 6th ed., New Jersey: Cambridge University Press, 1990, p. 126.

[10] Food and Agriculture Organization of the United Nations, "Chapter 2 - Soil and Water," FAO Land and Water Development Division, 1985. [Online]. Available: http://www.fao.org/docrep/r4082e/r4082e03.htm#2.5.3 capillary rise. [Accessed 10 January 2017].

[11] N. Goldshleger, E. Ben-Dor, Y. Benyamini, M. Agassi and D. G. Blumberg, "Characterization of the soil's spectral crust by the spectral reflectance in the SWIR region.," *Terre Nove*, pp. 12-17, 2001.

[12] M. A. Hardisky, V. Klemas and F. C. Daiber, "Remote sensing salt marsh biomass and stress detection.," *Advances in Space Research*, vol. 2, no. 8, pp. 219-229,

1983.

[13] N. A. O'Brien, C. A. Hulse, D. M. Friedrich, F. J. Van Milligen, M. K. von Gunten, F. Pfeifer and H. W. Siesler, "Miniature near-infrared (NIR) spectrometer engine for handheld applications," *SPIE Defense, Security and Sensing,* vol. 8374, 2012.

[14] I. Bogrekci and W. S. Lee, "Effects of soil moisture content on absorbance spectra of sandy soils in sensing phosphorus concentrations using UV-VIS-NIR spectroscopy.," *Trans. ASABE,* vol. 49, no. 4, pp. 1175-1180, 2006.

[15] J. W. Hummel, K. A. Sudduth and S. E. Hollinger, "Soil moisture and organic matter prediction of surface and subsurface soils using NIR soil sensor.," *Computer and electronics in agriculture,* vol. 32, no. 2, pp. 149-165, 2001.

[16] R. Keren and M. J. Singer, "Effects of low electrolyte concentration on hydraulic concentration on hydraulic conductivity of sodium/calcium-montmorillonite-sand system.," *Soil Science Society of America Journal,* pp. 368-373, 1988.

[17] B. T. Gouweleeuw, A. I. J. M. van Dijk, J. P. Guerschman, P. Dyce and M. Owe, "Space-based passive microwave soil moisture retrievals and the correction for a dynamic open water fraction.," *Hydrology and Earth System Sciences,* no. 16, pp. 1635-1675, 2012.

[18] Y. H. Kerr, P. Waldteufel, J.-P. Wigneron and J. Martinuzzi, "Soil moisture retrieval from space: the Soil Moisture and Ocean Salinity (SMOS) mission.,"

IEEE Transactions on GeoScience and Remote Sensing, vol. 39, no. 8, pp. 1729-1735, 2001.

[19] D. Entekhabi, E. G. Njoku, P. E. O'Neill and K. H. Kellogg, "The Soil Moisture Active Passive (SMAP) Mission," *Proceedings of the IEEE,* vol. 98, no. 5, pp. 704-716, 2010.

[20] N. S. Chauhan, S. M. Miller and P. Ardanuy, "Spaceborne soil moiture estimation at high resolution: a microwave-optical/IR synergistic approach.," *International Journal of Remote Sensing,* vol. 24, no. 22, pp. 4599-4622, 2003.

[21] B. J. Choudhury and R. Golus, "Estimating soil wetness using satellite data.," *International Journal of Remote Sensing,* vol. 9, no. 7, pp. 1251-1257, 1988.

[22] E. Burke and L. P. Simmonds, "Sub-pixel hetergeneity and the retrieval of soil moisture from passive microwave radiometry.," *International Journal of Remote Sensing,* vol. 24, no. 10, pp. 2085-2104, 2003.

[23] Y. Liou, Y.-C. Tzeng and J.-P. Wigneron, "Estimating soil moisture profiles by microwave radiometry over a wheat field.," Santa Fe, 2000.

[24] C. L. Parkinson, "Aqua: an Earth-Observing Satellite mission to examine water and other climate variables," *IEEE Transactions on GeoScience and Remote Sensing,* vol. 41, no. 2, pp. 173-183, 2003.

[25] M. Owe, R. De Jeu and A. Van De Griend, "Estimating long term surface soil moisture from satellite microwave observations in Illinois, USA.," in *Remote Sensing and Hydrology*, Santa Fe, 2000.

[26] National Center for Atmospheric Research, "Measuring Soil Moisture and Snow Depth with GPS," 2015. [Online]. Available: https://www.ral.ucar.edu/projects/measuring-soil-moisture-and-snow-depth-with-gps. [Accessed 22 September 2015].

[27] K. M. Larson, E. E. Small, E. Gutmann, A. Bilich, P. Alexrad and J. Braun, "Using GPS multipath to measure soil moisture fluctuations: initial results.," *GPS Solutions*, vol. 12, no. 3, pp. 173-177, 2008.

[28] H. Saari, I. Pellikka, L. Pesonen, S. Tuominen, J. Heikkila and C. Holmlund, "Unmanned Aerial Vechile (UAV) operated spectral camera system for forest and agriculture applications," *SPIE Remote Sensing, International Society for Optics and Photonics*, vol. 13, p. 81740H, 2011.

[29] L. F. Johnson, S. Herwitz, S. Dunagan, B. Lobitz, D. Sullivan and R. Slye, "Collection of ultra high spatial and spectral resolution image data over California vineyards with a small UAV," *Proceedings of the 30th International Symposium on Remote Sensing of the Environment*, vol. 20, pp. 845-849, 2003.

[30] Cubert-GmbH, "UAV based hyperspectral imaging," 2016. [Online]. Available:

http://cubert-gmbh.de/uav-based-spectral-imaging/. [Accessed 5 May 2016].

[31] T. Hakala, E. Honkavaara, H. Saari, J. Makynen, J. Kaivosoja, L. Pesonen and I. Polonen, "Spectral imaging from UAVs under varying illumination conditions.," *International Archives of the Photogrammetry, Remote Sensing and Spatial Information Sciences,* Vols. XL-1/W2, pp. 189-194, 2013.

[32] S. K. von Bueren, A. Burkart, A. Hueni, U. Rascher, M. P. Tuohy and I. J. Yule, "Deploying four optical UAV-based sensors over grassland: challenges and limitations.," *Biogeosciences,* vol. 12, no. 1, pp. 163-175, 2015.

[33] H. E. Revercomb, W. L. Smith, F. A. Best, J. Giroux, D. D. LaPorte, R. O. Knuteson and H. B. Howell, "Airborne and ground-based Fourier transform spectrometers for meteorology: HIS, AERI, and the new AERI-UAV.," in *International Society for Optics and Photonics*, 1996.

[34] A. Mac Arthur, I. Robinson, M. Rossini, N. Davis and K. MacDonald, "A Dual-Field-of-view Spectrometer System For Reflectance and Fluorescence Measurements (Piccolo Doppio) and Correction of Etaloning," in *5th Annual Workshop on Remote Sensing of Vegetation Fluorescence*, Paris, 2014.

[35] H. Chao, M. Baumann, A. Jensen, Y. Q. Chen, Y. Cao, W. Ren and M. McKee, "Band-reconfigurable Multi-UAV-Based Cooperative Remote Sensing for Real-Time Water Management and Distributed Irrigation Control," in *IFAC World*

Congress, Seoul, 2008.

[36] J. A. J. Berni, P. J. Zarco-Tejada, L. Suarez, V. Gonzalez-Dugo and E. Fereres, "Remote sensing of vegetation from UAV platforms using lightweight multispectral and thermal imaging sensors.," *ISPRS Annuals of the Photogrammetry and Remote Sensing Spatial Information Sciences,* vol. 38, no. 6-12, 2009.

[37] L. Wallace, A. Lucieer, C. Watson and D. Turner, "Development of a UAV-LiDAR System with Application to Forest Inventory," *Remote Sensing,* vol. 4, no. 6, pp. 1519-1543, 2012.

[38] E. Valencia, R. Acevo, X. Bosch-Lluis, A. Aguasca, N. Rodriguez-Alvarez, I. Ramos-Perez and A. Camps, "Initial Results of an airborne leight-weight L-band radiometer.," *Geoscience and Remote Sensing Symposium, 2008. IGARSS 2008. IEEE International ,* vol. 2, pp. 1176-1179, 2008.

[39] D. Turner, A. Lucieer and C. Watson, "Development of an Unmanned Aerial Vehicle (UAV) for hyper resolution vineyard mapping based on visible, multispectral, and thermal imagery.," *The International Archives of the Photogrammetry, Remote Sensing and Spatial Information Sciences,* Vols. ISRSE-34, 2011.

[40] F. Archer, A. M. Shutko, T. L. Coleman, A. Haldin, E. Novichikhin and I. Sidorov,

"Introduction, overview, and status of the Microwave Autonomous Copter System (MACS).," *GeoScience and Remote Sensing Symposium, IEEE International,* vol. 5, pp. 3574-3576, 2004.

[41] B. M. Quine and J. Drummond, "GENSPECT: a line-by-line code with selectable interpolation error tolerance.," *Journal of Quantitative Spectroscopy & Radiative Transfer*, vol. 74, no. 2, pp. 147-165, 2002.

[42] R. Jagpal, Calibration and Validation of Argus 1000 Spectrometer - A Canadian Pollution Monitor, vol. Dissertation, Toronto: York University, 2011.

[43] W. G. Rees, Physical Principals of Remote Sensing, 1st ed., Press Syndicate of the University of Cambridge, 1990.

[44] I. Sokolik, "Absorption by atmospheric gases in the IR, visible, and UV spectral regions.," School of Atmospheric Studies, Georgia Institute of Technology, Atlanta, 2009.

[45] P. Tans, "National Oceanis and Atmospheric Administration," [Online]. Available: http://www.esrl.noaa.gov/gmd/ccgg/trends/. [Accessed 19 April 2013].

[46] R. D. Evans, J. Belnap, F. Garcia-Pichel and S. L. Phillips, "Remote sensing of biological soil crusts," in *Biological Soil Crusts: Structure, Function and Management*, Prince George, 2001, pp. 431-457.

[47] S. Eagleson, "Canadian Advanced Nanospace Experiment 2: Scientific and Technological Innovation on a Three-Kilogram Satellite," in *International Astronomical Congress (IAC)*, 2007.

[48] Thoth Technology, Inc., 2013. [Online]. Available: http://www.thothx.com/manuals/Argus%20Owner's%20Manual,%20Thoth%20Technology,%20Mar%202013,%20rel%20%201_11.pdf.

[49] Sensor's Unlimited, Inc., "InGaAs Products: Focal Plane Arrays," 2014. [Online]. Available: http://www.sensorsinc.com/arrays.html. [Accessed 3 June 2014].

[50] J. Belsky, *Personal Communication*, 2013.

[51] Edmund Optics, "Hastings Triplet Achromatic Lenses," 2014. [Online]. Available: http://www.edmundoptics.com/optics/optical-lenses/achromatic-lenses/hastings-triplet-achromatic-lenses/1725. [Accessed 15 March 2014].

[52] Schott North America, Inc., 2005. [Online]. Available: http://fp.optics.arizona.edu/optomech/references/glass/Schott/tie-35_transmittance_us.pdf. [Accessed 20 June 2014].

[53] Schott North America, Inc., [Online]. Available: http://www.schott.com/advanced_optics/us/abbe_datasheets/schott_datasheet_all_us.pdf. [Accessed 19 June 2014].

[54] Edmund Optics, "Product Support," [Online]. Available: http://www.edmundoptics.com/techsupport/resource_center/product_docs/prnt_67417.pdf. [Accessed 16 June 2014].

[55] H. Bach and N. Neuroth, The Properties of Optical Glass, 1st ed., Berlin: Springer Berlin Heidelberg, 1998.

[56] Edmund Optics, [Online]. Available: http://www.edmundoptics.com/optics/optical-filters/longpass-edge-filters/longpass-filters/2683/. [Accessed 20 March 2015].

[57] Thorlabs, [Online]. Available: https://www.thorlabs.com/thorproduct.cfm?partnumber=FELH1300. [Accessed 15 March 2015].

[58] W. Beaty, 2004. [Online]. Available: http://amasci.com/miscon/coherenc.html. [Accessed 12 November 2015].

[59] K. J. Gåsvik, Optical Metrology, 3rd ed., Trondheim: Wiley, 2002.

[60] Newport Corporation, 2015. [Online]. Available: http://search.newport.com/?x2=sku&q2=63350. [Accessed 30 October 2015].

[61] T. Erdogan, "Coherence and Combining Filters," 31 May 2011. [Online]. Available: http://www.semrock.com/Data/Sites/1/semrockpdfs/coherenceandcombiningfilters.

pdf. [Accessed 12 December 2015].

[62] DuPont, "Delrin Acetal Resin," 2012. [Online]. Available: http://www2.dupont.com/Plastics/en_US/assets/downloads/design/230323c.pdf. [Accessed 3 June 2014].

[63] Aerospace Specification Metals, Inc., [Online]. Available: http://asm.matweb.com/search/SpecificMaterial.asp?bassnum=MA6061T6. [Accessed 18 June 2014].

[64] AeroXCraft, [Online]. Available: http://www.aeroxcraft.com/landing-gear-c-13/dji-f550-landing-gear-set-p-20.html. [Accessed 12 March 2015].

[65] Polymer Plastics, "G10 FR-4 GLASS EPOXY COMPOSITE LAMINATE," [Online]. Available: http://www.polymerplastics.com/composite_g10.shtml . [Accessed 12 March 2015].

[66] Denver Instruments, 2013. [Online]. Available: http://www.denverinstrument.com/denverusa/media/pdf/literature/NEW_Summit.pdf. [Accessed 10 June 2014].

[67] American Society for Testing and Materials, "Standard Test Method for Laboratory Determination of Water (Moisture) Content of Soil and Rock by Mass," 1998. [Online]. Available: http://www.ce.sc.edu/deptinfo/members/faculty/ray/web1/Ugrad/ECIV%20330/AS

TM/D2216MoistureContent.PDF. [Accessed 15 January 2015].

[68] SPX, 2013. [Online]. Available: http://www.thermalproductsolutions.com/products/productDetails.aspx?pscId=41&plId=36. [Accessed 10 June 2014].

[69] J. Taylor, An Introduction to Error Analysis: The Study of Uncertainties in Physical Measurements, 2nd ed., University Science Books, 1997.

[70] J. H. Walker, R. D. Saunders, J. K. Jackson and D. A. McSparron, "NBS Measurements Services: Spectral Radiance Calibration," *NBS Special Publication,* vol. 102, no. 1987.

[71] Feit Electric, 2015. [Online]. Available: http://www.feit.com/halogen/jc-jcd/bpq20t3. [Accessed 16 November 2015].

[72] W. E. Forsythe and A. G. Worthing, "The Properties of Tungsten and the Characteristics of Tungsten Lamps," *Astrophysical Journal,* vol. 61, pp. 146-185, 1925.

[73] Newport Corporation, 2015. [Online]. Available: http://www.newport.com/Pencil-Style-Calibration-Lamps/377846/1033/info.aspx#tab_Overview. [Accessed 16 December 2015].

[74] NASA, 1997. [Online]. Available: http://outgassing.nasa.gov/og_desc.html.

[Accessed 5 September 2015].

[75] American Society for Testing and Materials, "ASTM Standard E 595-98 Total Mass Loss and Collected Volatile Materials from Outgassing in a Vacuum Environment," 1998.

[76] Thoth Technology, Inc., 2014. [Online]. Available: http://thothx.com/thermal-vacuum-test-services/. [Accessed 10 December 2015].

[77] Shimadzu Corporation, "IR Analysis Q&A," Shimadzu Corporation, 2016. [Online]. Available: http://www.shimadzu.com/an/ftir/support/faq/2.html. [Accessed 1 December 2016].

[78] European Space Agency, 4 September 2013. [Online]. Available: http://www.esa.int/Our_Activities/Space_Engineering_Technology/What_kind_of_testing_do_the_Materials_and_Components_Laboratories_carry_out. [Accessed 9 September 2015].

[79] NASA, 2008. [Online]. Available: https://outgassing.nasa.gov/help/og_help.html. [Accessed 14 December 2015].

[80] MasterBond, [Online]. Available: http://www.masterbond.com/certifications/nasa-low-outgassing. [Accessed 15 September 2015].

[81] Food and Argricultural Organization of the United Nations, "Chapter 2- Soil and

Water," 1985. [Online]. Available: http://www.fao.org/docrep/r4082e/r4082e03.htm#2.2.1 the infiltration process. [Accessed 5 January 2017].

Appendix

The following data shown in Table A-0-1 TML Collected Results in was collected during the TML experiment.

Table A-0-1 TML Collected Results

Parameter	**Unit**	**Test Data**	**Test Data**
Test Manager	#	RJ	RJ
Start Date	#	27-Feb-15	27-Feb-15
End Date		02-Mar-15	02-Mar-15
Client ID	#	cat1	cat2
Thoth ID	#	P-002	Q-002
Description	#	Delrin Cube 1	Delrin Cube 2
Manufacturer	#	DuPont	DuPont
Requestor	#	Tsouvaltsidis	Tsouvaltsidis
Sample Temperature	C	125	125
Collector Temperature	C	25	25
Pressure	Torr	1.0E-05	1.0E-05
Time at temperature	hours	24	24
Number of samples per boat	#	1	1
Approx. weight per sample	g	0.202984	0.202424
Initial holder mass	g	0.061136	0.068514
Final holder mass	g	0.061118	0.068586
Initial collector mass	g	16.823192	16.655632
Cleaned Collector Mass	g	16.823246	16.655574
Final collector mass	g	16.823294	16.655680

Initial holder + sample	g	0.264072	0.270872
Initial + sample after 24hrs	g	0.264094	0.270888
Final holder + sample	g	0.263228	0.270024
Reweighed sample + holder	g	0.263426	0.270224
Initial collector mass	g	16.823246	16.655574
Final collector mass	g	16.823294	16.655680

Table A-0-2 E-595 test results (adapted from [79])

Material	Manufacturer	Test Provider	TML (%)	CVCM (%)	WVR (%)
DELRIN 150 ACETAL 1.25 INCH DIA BLACK ROD #1	DuPont	NASA	0.43	0.02	.20
DELRIN 150 ACETAL 1.25 INCH DIA BLACK ROD #2	DuPont	NASA	0.47	0.02	.13
Delrin 150 SA Sample 1	DuPont	Thoth	0.43	0.02	0.10
Delrin 150 SA Sample 2	DuPont	Thoth	0.43	0.05	0.10

Materials pass or fail the test based on these TML and CVCM measurements. If the CVCM exceeds 0.1%, the material fails. The material will also fail if the TML exceeds 1%—though the TML may be offset by water vapor regained (WVR) by the sample in a subsequent measurement [80]. The measurements taken the TVAC facility are in agreement with the NASA test measurements. The conditions which need to be met are seen in Table A-0-3.

Table A-0-3 ASTM E-595 Pass/Fail Conditions

Condition		**Outcome**
CVCM	**TML**	
< 0.1%	<1%	Material passes
<0.1%	>1%	If TML-WVR <1%, material can pass
> 0.1%	NA	If TML-WVR > 1%, material fails

If a material passes NASA low outgassing tests, it can potentially be used in a multitude of applications including outer space, high vacuum, specialty optical and electro-optical applications, among others.